Department of Physics and Astronomy
University of Heidelberg

Polarised WW Scattering at the LHC

Master Thesis in Physics

submitted by

Johann Brehmer

born in Bremen

2014

This Master thesis has been carried out by Johann Brehmer at the
Institute for Theoretical Physics under the supervision of
Professor Tilman Plehn and Professor Joerg Jaeckel.

Abstract in deutscher Übersetzung

Die Polarisierung von W- und Z-Bosonen hängt fundamental mit dem Prozess der elektroschwachen Symmetriebrechung zusammen: Im Grenzfall von hohen Energien entsprechen longitudinale Vektorbosonen gerade den Goldstone-Bosonen. Eine Messung der Polarisierung kann deshalb dazu beitragen, die Struktur der elektroschwachen Physik zu verstehen. Bisher sind die longitudinalen und transversalen Moden vor allem im Kontext von Eichboson-Streuung bei hohen Energien betrachtet worden, allerdings leiden solche Messungen an geringen Wirkungsquerschnitten und hohen systematischen Unsicherheiten.

In dieser Arbeit verfolgen wir zwei alternative Ansätze. Zum einen verwenden wir die Verteilung von Zerfallswinkeln, um die Polarisierung der Eichbosonen im Endzustand zu messen. Zum anderen entwickeln wir eine neue Strategie, um die Polarisierung der Eichbosonen im Anfangszustand zu messen. Als Observablen verwenden wir dabei die kinematischen Eigenschaften der Tagging-Jets an der Higgs-Resonanz. Beide Methoden ermöglichen eine Überprüfung des Higgs-Eich-Sektors, und vor allem letztere Strategie kann schon in den nächsten Jahren am LHC realisiert werden. Basierend auf einer Statistik von 300 fb^{-1} bei 13 TeV können damit die Kopplungen der longitudinalen und transversalen Eichbosonen an das Higgs-Boson separat mit einer Genauigkeit von ungefähr 20% gemessen werden.

Abstract

The polarisation of W and Z bosons is intimately linked to the nature of electroweak symmetry breaking: in the limit of high energies, their longitudinal modes correspond just to the Goldstone bosons. This distinct physical origin means that a polarisation measurement can help us understand the structure of electroweak physics. Such a separation of longitudinal and transverse modes is well established in studies of the high-energy behaviour of gauge boson scattering. However, this classical approach suffers from low rates and large systematic uncertainties.

In this thesis we follow two alternative strategies. Angular distributions in gauge boson decays are used to measure the polarisation of the final gauge boson pair. At the same time, we develop a novel approach that probes the polarisation of the initial gauge boson pair in the kinematics of the tagging jets. Instead of the high-energy regime, we focus on the Higgs resonance. We find that both measurements are sensitive to the Higgs-gauge sector, and that especially the latter approach is feasible during the upcoming LHC run. After 300 fb^{-1} of data at 13 TeV, we will be able to separately test the longitudinal and transverse gauge boson couplings to the Higgs boson at the 20% level.

Contents

1. Introduction

Electroweak symmetry breaking is one of the core ingredients of modern particle physics, offering an elegant way to reconcile local gauge invariance with the observed massive $W^{\pm}$ and Z bosons. Its most straightforward realisation is the Higgs mechanism in the Standard Model, where the electroweak $\mathrm{SU}(2) \times \mathrm{U}(1)$ symmetry is spontaneously broken by a fundamental scalar doublet with non-zero vacuum expectation value. With the discovery of a scalar Higgs boson [1, 2], the Standard Model is finally complete.

At the same time, the Standard Model leaves many experimental and theoretical questions unanswered. It does not provide an explanation for the values of its many parameters or its intricate gauge structure, nor does it solve the hierarchy problem: why is the electroweak scale so small compared to the Planck scale in the presence of large quantum corrections? Different theories have been proposed to tackle these problems, including models where the Higgs boson is a composite object due to some higher-scale symmetry [3–6]. Understanding whether the Standard Model with its fundamental Higgs boson describes our world all the way up to a grand unification scale, or whether the structure of electroweak symmetry breaking is more complex, is one of the most important tasks for the experiments at the Large Hadron Collider (LHC) in the next years.

In this thesis we analyse how measurements of the polarisation of the massive gauge bosons $W^{\pm}$ and Z can contribute to these questions. There is a fundamental physical difference between the longitudinal and transverse modes: the Goldstone boson equivalence theorem [7–9] links the longitudinal states to the Goldstone bosons of electroweak symmetry breaking, while the transverse modes correspond to the original electroweak gauge bosons. This separation is only exact in the limit of large momenta. But even at finite energies, the polarisation of massive gauge bosons is closely linked to the structure of electroweak symmetry breaking.

The classical approach to the Higgs-gauge sector is longitudinal gauge boson scattering at high energies. Any deviation from the Standard Model Higgs-gauge coupling leads to a non-cancellation between gauge amplitudes and Higgs amplitudes, visible as an increase of the scattering rate at large energies [8, 10–12]. Much attention has been spent on the development of analysis techniques to measure such a cross-section increase at the LHC [13–23]. However, the observed Higgs boson at least dampens this effect significantly, further reducing the already small rates of such signatures. It was pointed out in [24] that these measurements also suffer from large scale uncertainties that can reach $\mathcal{O}(100\%)$. Such an analysis at the LHC therefore has to be considered challenging

at the very least.

These systematic uncertainties can be avoided by measuring the relative fractions of longitudinal and transverse gauge bosons instead of absolute rates. One can choose to probe either the initial or the final pair of gauge bosons in $VV \to VV$ scattering, where $V = W^{\pm}, Z$. The authors of [24] pioneered one such strategy by fitting angular distributions to the gauge boson decay products in the semileptonic WW channel. These observables are a model-independent probe of the polarisation of the final gauge boson pair. As a first part of this thesis, we extend this approach to other gauge boson channels and briefly discuss whether it can be realised in the coming years of LHC operation.

The main aim of this thesis, however, is the development of an entirely different approach to polarised gauge boson scattering. Instead of the high-energy limit, we focus on the phase-space region around the Higgs resonance, which is clearly sensitive to the Higgs-gauge coupling structure and gives larger rates than the high-energy regime. Instead of the decay products of the final pair of gauge bosons, we analyse the kinematics of the tagging jets, which are sensitive to the polarisation of the initial pair of gauge bosons. Our approach is motivated by the effective W approximation [25–27], which predicts an analytical relation between the transverse momenta of the tagging jets and the polarisation of the initial gauge bosons. We begin with an evaluation of its validity and then leave this approximation behind and analyse the full process. Signatures in different observables are discussed, including the transverse jet momenta and angular correlations between the two jets. We calculate their significance and compare them to alternative approaches. Our findings are submitted for publication [28].

This thesis begins with the theoretical and phenomenological foundations in chapter 2. After a brief recapitulation of the mechanism of electroweak symmetry breaking in and beyond the Standard Model, we discuss the role of longitudinal and transverse gauge bosons and analyse the structure of gauge boson scattering. The chapter concludes with an overview of possible approaches to the Higgs-gauge sector and a brief review of existing studies. In chapter 3 we discuss the measurement of angular distributions in the decays of final-state gauge bosons. Our strategy to measure the polarisation of initial-state gauge bosons in the kinematics of the tagging jets at the Higgs resonance is the topic of chapter 4. We give our conclusions in chapter 5.

2. The physics of massive gauge bosons

In this chapter we introduce the theoretical and phenomenological framework for the analysis strategies of this thesis. The foundations are laid in section 2.1. We recapitulate the concept of electroweak symmetry breaking and the Standard Model as well as some scenarios beyond the Standard Model. We then briefly review the current experimental status and outline the open questions we try to answer. In section 2.2 we present the tool we focus on during this thesis: the polarisation of W and Z bosons. In particular, we explain why their longitudinal modes play a special role in particle physics and formulate the Goldstone boson equivalence theorem. Finally, in section 2.3 we turn to our laboratory, gauge boson scattering processes. From a theoretical point of view, these amplitudes have an interesting high-energy behaviour, where deviations from the Standard Model can lead to a violation of perturbative S-matrix unitarity. We also approach gauge boson scattering from a phenomenological perspective and discuss the different strategies it provides to measure the Higgs-gauge sector.

2.1. The bigger picture

2.1.1. Electroweak symmetry breaking

Quantum field theories that are invariant under local gauge symmetries are one of the most successful ideas in modern physics. This concept predicts spin-1 gauge bosons, which are necessarily massless. While the photon and the gluon fit in this picture easily, the massive W and Z bosons do not. However, their masses can be accommodated in a fully gauge-invariant theory by means of spontaneous symmetry breaking. We will now give a brief review of this concept, for a detailed review see for instance [29].

It is worth stressing that the Higgs mechanism in the Standard Model is not the only realisation of electroweak symmetry breaking. We will now discuss electroweak symmetry breaking in rather general terms, i. e. we will not assume anything about the nature of the field Σ that breaks the $\mathrm{SU}(2)_\mathrm{L} \times \mathrm{U}(1)_\mathrm{Y}$ gauge group. The Standard Model on the other hand explicitly explains this object in terms of a fundamental scalar doublet ϕ. This will be the topic of the next section.

Nearly all observed particles and interactions can be described by a quantum field theory invariant under a local $\mathrm{SU}(3)_\mathrm{C} \times \mathrm{SU}(2)_\mathrm{L} \times \mathrm{U}(1)_\mathrm{Y}$ gauge symmetry. The corresponding gauge bosons are G^i_μ, W^i_μ, and B_μ, the coupling constants g_S, g, and g'. The fermions f of this theory and the representations of the gauge group they transform

Fields				Representation $\mathrm{SU(3)_C}$	$\mathrm{SU(2)_L}$	$\mathrm{U(1)_Y}$
LH quarks	$\begin{pmatrix} u \\ d \end{pmatrix}_L$	$\begin{pmatrix} c \\ s \end{pmatrix}_L$	$\begin{pmatrix} t \\ b \end{pmatrix}_L$	**3**	**2**	$\frac{1}{6}$
RH u-type quarks	u_R	c_R	t_R	**3**	1	$\frac{2}{3}$
RH d-type quarks	d_R	s_R	b_R	**3**	1	$-\frac{1}{3}$
LH leptons	$\begin{pmatrix} \nu_e \\ e^- \end{pmatrix}_L$	$\begin{pmatrix} \nu_\mu \\ \mu^- \end{pmatrix}_L$	$\begin{pmatrix} \nu_\tau \\ \tau^- \end{pmatrix}_L$	1	**2**	$-\frac{1}{2}$
RH leptons	e_R^-	μ_R^-	τ_R^-	1	1	-1

Table 2.1.: Fermionic fields in the Standard Model and the representations of the gauge group they transform under.

under are given in table 2.1. The kinetic terms in the Lagrangian read

$$\mathcal{L}_{\text{kin}} = -\frac{1}{4} G^i_{\mu\nu} G^{i\,\mu\nu} - \frac{1}{4} W^i_{\mu\nu} W^{i\,\mu\nu} - \frac{1}{4} B_{\mu\nu} B^{\mu\nu} + \sum_{\text{fermions}} \bar{f} \mathrm{i} \not{D} f, \tag{2.1}$$

with field strength tensors

$$G^i_{\mu\nu} = \partial_\mu G^i_\nu - \partial_\nu G^i_\mu + g_s f^{ijk} G^j_\mu G^k_\nu \,, \tag{2.2}$$

$$W^i_{\mu\nu} = \partial_\mu W^i_\nu - \partial_\nu W^i_\mu + g \varepsilon^{ijk} W^j_\mu W^k_\nu \,, \tag{2.3}$$

$$B_{\mu\nu} = \partial_\mu B_\nu - \partial_\nu B_\mu \,. \tag{2.4}$$

Here f^{ijk} and ε^{ijk} are the structure constants of $\mathrm{SU(3)_C}$ and $\mathrm{SU(2)_L}$, respectively. The covariant derivatives D_μ are chosen according to the gauge representations given in table 2.1.

Under an $\mathrm{SU(2)_L}$ transformation, the left-handed (LH) fermion fields transform as

$$f_L(x) \to \exp\left(\mathrm{i}\alpha_i(x)\frac{\tau_i}{2}\right) f_L(x) \tag{2.5}$$

with Pauli matrices τ_i, while the right-handed (RH) fermion fields f_R remain invariant. Under $\mathrm{U(1)_Y}$ transformations, the fermions transform as

$$f \to \exp\left(\mathrm{i}\beta(x) y\right) f \,, \tag{2.6}$$

where y is the $\mathrm{U(1)_Y}$ charge of the fermionic field. Note that there is a difference between these charges for the left-handed and right-handed fields.

Plain mass terms for the gauge bosons or fermions à la $\frac{1}{2} m_W^2 W^\mu W_\mu$ or $\bar{f}_L m_f f_R$ explicitly break the gauge symmetry. However, one can introduce a new field Σ and require

that it transforms as

$$\Sigma \to \exp\left(\mathrm{i}\alpha_i(x)\frac{\tau_i}{2}\right)\Sigma\exp\left(-i\beta(x)\frac{\tau_3}{2}\right) \tag{2.7}$$

under a combined $\mathrm{SU(2)_L} \times \mathrm{U(1)_Y}$ transformation. Then the term

$$\mathcal{L}_V = -\frac{v^2}{4}\,\mathrm{Tr}\left[V^\mu V_\mu\right] \tag{2.8}$$

with a constant v and $V_\mu = \Sigma(D_\mu\Sigma)^\dagger$ is invariant under the gauge group. The same is true for

$$\mathcal{L}_{\text{Yukawa}} = -\sum_{\text{fermions}} \bar{f} m_f \Sigma f\,. \tag{2.9}$$

Finally, one can add a potential for the Σ field:

$$\mathcal{L}_\Sigma = -\frac{\mu^2 v^2}{4}\,\mathrm{Tr}\left[\Sigma^\dagger\Sigma\right] - \frac{\lambda v^4}{16}\left(\mathrm{Tr}\left[\Sigma^\dagger\Sigma\right]\right)^2\,, \tag{2.10}$$

where μ and λ are constants. Collecting all the pieces, the full theory is given by

$$\mathcal{L} = \mathcal{L}_{\text{kin}} + \mathcal{L}_V + \mathcal{L}_{\text{Yukawa}} + \mathcal{L}_\Sigma\,, \tag{2.11}$$

and is fully gauge invariant and renormalisable.

Now assume that the potential for Σ is chosen such that

$$\mu^2 < 0\,, \tag{2.12}$$

$$v = \sqrt{-\frac{\mu^2}{\lambda}}\,. \tag{2.13}$$

Then the ground state or vacuum expectation value for Σ satisfies

$$\langle\Sigma^\dagger(x)\Sigma(x)\rangle = \mathbb{1}\,. \tag{2.14}$$

This condition suggests the parameterisation of this state of lowest energy as

$$\langle\Sigma(x)\rangle = \exp\left(-\frac{\mathrm{i}}{v}w^i(x)\tau^i\right) \tag{2.15}$$

in terms of the Pauli matrices τ^i and the so-called Goldstone bosons $w^i(x)$. The interaction between the gauge bosons and the Σ field turns into

$$\mathcal{L}_V \supset -\frac{v^2}{4}\,\mathrm{Tr}\left[V^\mu V_\mu\right] \tag{2.16}$$

$$= \frac{g^2v^2}{4}W^+_\mu W^{-\,\mu} + \frac{g^2v^2}{8c_W^2}Z_\mu Z^\mu \tag{2.17}$$

with

$$W_\mu^\pm = \frac{1}{\sqrt{2}}\left((W_\mu^1 - \frac{1}{gv}\partial_\mu w^1) \pm \mathrm{i}(W_\mu^2 - \frac{1}{gv}\partial_\mu w^2)\right), \tag{2.18}$$

$$Z_\mu = c_W(W_\mu^3 - \frac{1}{gv}\partial_\mu w^3) - s_W B_\mu, \tag{2.19}$$

$$c_W = \frac{g}{\sqrt{g^2+g'^2}}, \tag{2.20}$$

and

$$s_W = \frac{g'}{\sqrt{g^2+g'^2}}. \tag{2.21}$$

This reveals the mass-eigenstate bosons $W^\pm$ and Z with masses

$$m_W = \frac{gv}{2}, \tag{2.22}$$

$$m_Z = \frac{gv}{2c_W}. \tag{2.23}$$

In a nutshell, the fact that the vacuum expectation value of Σ is not invariant under the symmetry group leads to two remarkable transformations, which turn the original gauge bosons W^i, B into the mass eigenstates $W^\pm$, Z given in (2.18) and (2.19):

1. Derivatives of the Goldstone fields and the original massless gauge fields are combined into new, massive vector fields with three degrees of freedom each. This 'Higgs-Kibble dinner' (since the gauge bosons 'eat' the Goldstone modes) is a crucial point for the physics of massive vector bosons. While these particles are usually called 'gauge bosons', they are in fact a superposition of true gauge bosons and Goldstone bosons. This is why their behaviour under gauge transformations differs from that of 'proper' gauge bosons, and ultimately, why these vector bosons can be massive.

2. These massive vector fields mix, giving rise to the charge and mass eigenstates $W^\pm$ and Z.

There are some loose ends which should be quickly summed up. The remaining parts of W_μ^3 and B_μ form the massless photon

$$A_\mu = s_W W_\mu^3 + c_W B_\mu, \tag{2.24}$$

the gauge boson of the unbroken $\mathrm{U(1)_Q}$ symmetry of electromagnetism. With respect to this remaining gauge group, the fermions carry the electromagnetic charge $q = y + \frac{\tau_3}{2}$, where the second term should be replaced by its eigenvalue in the case of $\mathrm{SU(2)_L}$ doublets and zero for the singlets. Finally, the Yukawa terms (2.9) yield fermion masses, and, if the mass terms m_f are replaced by non-diagonal generation matrices, the CKM matrix.

2.1.2. The Standard Model

So far, Σ was just a field transforming in a specific way under the $\mathrm{SU}(2)_\mathrm{L} \times \mathrm{U}(1)_\mathrm{Y}$ gauge transformations, and its fundamental nature was irrelevant for the generation of boson and fermion masses. The simplest and most famous particular model of electroweak symmetry breaking is the Higgs mechanism in the Standard Model (SM). It introduces a complex scalar $\mathrm{SU}(2)_\mathrm{L}$ doublet ϕ, which is uncharged under $\mathrm{SU}(3)_\mathrm{C}$ and carries an $\mathrm{U}(1)_\mathrm{Y}$ hypercharge of $\frac{1}{2}$. The potential of ϕ is a fourth-order polynomial with a minimum at $\langle|\phi|\rangle = v/\sqrt{2}$. Parameterised as fluctuations around this vacuum expectation value, the field contains four real degrees of freedom:

$$\phi = \frac{1}{\sqrt{2}} \exp\left(-\frac{\mathrm{i}}{v} w^i \tau^i\right) \begin{pmatrix} 0 \\ v + H \end{pmatrix} \tag{2.25}$$

$$= \frac{1}{\sqrt{2}} \begin{pmatrix} -w^2 - \mathrm{i}w^1 \\ v + H + \mathrm{i}w^3 \end{pmatrix} + \mathcal{O}(w^i w^j, w^i H)\,. \tag{2.26}$$

As in the general Σ model, three of them are the Goldstone fields w^i, which combine with the gauge bosons to form the massive vector bosons $W^\pm$ and Z according to (2.18) and (2.19). The fourth degree of freedom in ϕ manifests itself as another real scalar field, the Higgs boson H. Comparing the Standard Model to the Σ model of the previous section, the Σ field corresponds to a complex 2×2 matrix, where one column is exactly ϕ and the other column contains the same information:

$$\Sigma = \frac{\sqrt{2}}{v}\left(\tilde{\phi}\, \phi\right) \tag{2.27}$$

with $\tilde{\phi} = \mathrm{i}\tau_2 \phi^*$.

In this parameterisation, the Lagrangian takes on a much simpler form including kinetic and potential terms for the ϕ field:[1]

$$\begin{aligned}
\mathcal{L}_\mathrm{SM} = &-\frac{1}{4} G^i_{\mu\nu} G^{i\,\mu\nu} - \frac{1}{4} W^i_{\mu\nu} W^{i\,\mu\nu} - \frac{1}{4} B_{\mu\nu} B^{\mu\nu} \\
&+ \sum_\text{fermions} \bar{f} \mathrm{i} \not{D} f + (D^\mu \phi)^\dagger (D_\mu \phi) \\
&- \mu^2 \phi^\dagger \phi - \lambda (\phi^\dagger \phi)^2 \\
&- \sum_\text{generations} \frac{\sqrt{2}}{v} \left(m_u \begin{pmatrix} \bar{u} \\ \bar{d} \end{pmatrix}_L \tilde{\phi}\, u_R + m_d \begin{pmatrix} \bar{u} \\ \bar{d} \end{pmatrix}_L \phi\, d_R + m_l \begin{pmatrix} \bar{\nu}_e \\ \bar{e}^- \end{pmatrix}_L \phi\, e_R \right) \\
&+ \text{h. c. of some terms}\ .
\end{aligned} \tag{2.28}$$

[1] This is basically the expression found on numerous coffee mugs, T-shirts and post cards around CERN, modulo a few errors in the merchandise version.

The third line of this Lagrangian is the famous Mexican-hat potential for the scalar doublet ϕ.

The most distinctive feature of the Standard Model in comparison with other models of electroweak symmetry breaking is the Higgs boson H. The potential for ϕ leads to a mass

$$m_H^2 = -2\mu^2 = 2\lambda v^2 \,, \tag{2.29}$$

and the fact that in ϕ it only appears together with v means that its couplings to both fermions and gauge bosons are fully determined by their masses.

2.1.3. Beyond the Standard Model

At energies up to the TeV scale, the Standard Model has been extremely successful and agrees with nearly all observations. But it does have its shortcomings, among them the famous hierarchy problem: why is the electroweak scale so small compared to the Planck scale despite huge quantum corrections? Also, the host of parameters of the Standard Model and the complicated gauge structure are not very satisfying, surely there must be some simpler theory to explain our world?

While the Higgs sector of the Standard Model might be the simplest realisation of electroweak symmetry breaking, it is by no means the only such mechanism. Many alternatives aim to answer the questions raised by the Standard Model. For instance, Technicolor models [30–32] describe the symmetry-breaking object Σ not as a fundamental scalar, but as a quark condensate. These theories are constructed in analogy to strong chiral symmetry breaking: when an asympotically free gauge group becomes strongly interacting, expectation values of the type $\langle\bar{\psi}\psi\rangle$ become non-zero, thus breaking the electroweak symmetry and providing masses to the W and Z bosons. Such a generation of the weak scale by dimensional transmutation does not lead to a hierarchy problem. The original Technicolor models do not predict the existence of a light scalar resonance such as the Higgs boson.

Other theories of electroweak symmetry breaking predict a composite or strongly interacting Higgs boson [3, 4]. Typically it arises from the breaking of some higher-scale symmetry as a pseudo-Goldstone boson. This symmetry protects the weak scale from quantum corrections and thus (at least partially) solves the hierarchy problem. Such theories include Little Higgs [5] and Holographic Higgs models [6]. Finally, other models describe the electroweak gauge bosons as composite particles of an emergent gauge symmetry [33].

All in all, there are some reasons and plenty of room for new physics between the electroweak scale and the Planck scale $\Lambda_{Pl} \sim 10^{19}$ GeV, where a new theory is necessary to describe gravity as well. Any model of physics beyond the Standard Model has a typical energy scale Λ, for instance the mass of new particles. If Λ is larger than the

energy scale probed by current experiments (a few TeV at the LHC), this model cannot be discovered directly, e. g. by searching for new resonances.

However, the theory might still leave an imprint in the interactions of the known particles at accessible energies. This effect can be described in a model-independent way in the framework of effective field theory: at energies $E \ll \Lambda$, any model of physics beyond the Standard Model can be described by a number of higher-dimensional operators:

$$\mathcal{L}_{\text{eff}} = \mathcal{L}_{\text{SM}} + \sum_{d>4} \sum_{i} \frac{c_{d,i}}{\Lambda^{d-4}} \mathcal{O}_{d,i} \,, \tag{2.30}$$

where $\mathcal{O}_{d,i}$ is an operator of energy dimension d. Given a fundamental theory in the ultraviolet regime, Wilsonian renormalisation allows the calculation of the constants $c_{d,i}$. Typically one assumes that new physics also satisfies the basic construction principles of the Standard Model, Lorentz invariance and gauge invariance. This considerably reduces the number of possible operators and follows naturally from the enormous success of gauge theories in the description of our world. However it also poses a limitation: such an approach is blind to any higher-scale physics that does not follow these assumptions.

If the coefficients $c_{d,i}$ are roughly of the same order of magnitude, the factor of $\Lambda^{-(d-4)}$ means that the higher the dimension of an operator, the less significant it is at low energies. There are no dimension-five operators relevant for the scattering of weak bosons, so the dominant contributions beyond the Standard Model are expected to be described by dimension-six operators. Two example operators that we will use later in this thesis are

$$\mathcal{O}_W = (D_\mu \phi)^\dagger \, W^{\mu\nu} \, (D_\nu \phi) \tag{2.31}$$

and

$$\mathcal{O}_{\phi,2} = \frac{1}{2} \partial_\mu \left(\phi^\dagger \phi \right) \partial^\mu \left(\phi^\dagger \phi \right) \,, \tag{2.32}$$

following the conventions of [34]. For convenience, the field-strength tensors $W^{\mu\nu}$ now include the gauge constants and the $\mathrm{SU(2)_L}$ and $\mathrm{U(1)_Y}$ generators,

$$W_{\mu\nu} = \frac{\mathrm{i}}{2} g \tau^i \left[\partial_\mu W^i_\nu - \partial_\nu W^i_\mu + g \varepsilon^{ijk} W^j_\mu W^k_\nu \right] \,. \tag{2.33}$$

Note that this convention is different from the definition used in section 2.1.1. The operators $\mathcal{O}_{\phi,2}$ and $\mathcal{O}_W$ can be generated in theories with a strongly-interacting light Higgs sector, including Little Higgs and Holographic Higgs theories [4]. Of course, there are many more dimension-6 operators relevant to electroweak physics, which are discussed in more detail in [34–40].

2.1.4. Experimental status

In the previous section we have found that from a theoretical point of view, alternative models of symmetry breaking can solve questions that the Standard Model leaves unanswered. However, so far the experimental reality fails to comply with these arguments and indeed provides impressive evidence in favour of the Standard Model. In the summer of 2012, the ATLAS and CMS experiments discovered a new resonance around $m_H = 125$ GeV that remarkably resembles the Standard Model Higgs boson [1, 2]. Its scalar nature is established [41] and a CP-even eigenstate is preferred over a CP-odd eigenstate, although admixtures are not ruled out. The couplings of this particle agree with the Standard Model predictions, albeit within relatively large error bars [42]. With the Higgs discovery, the particle zoo of the Standard Model is complete. Even worse for models of new physics, the first run of the LHC has not given us any other new resonances or, more generally, deviations from the Standard Model. All in all, the LHC results so far are a triumph for the Standard Model.

So where does this leave alternative models of the electroweak sector? Theories without a light Higgs-like resonance such as the original Technicolor are ruled out by the Higgs discovery. On the other hand, strongly interacting light Higgs sectors, including Little Higgs and Holographic Higgs models, are still alive. The absence of any direct signal puts these theories under pressure and shifts their energy scales above the TeV scale, which implies that they can only provide a less natural solution to the hierarchy problem than originally hoped for. Still, it is way too early to give up on these well-motivated models.

It is now safe to assume that the Standard Model provides a good description of physics up to the TeV scale, and any relevant new physics resides at higher scales. This justifies the parameterisation of new physics in terms of effective field theory as described in the previous section. Constraints on new physics can hence be expressed as limits on higher-dimensional operators. For the Higgs-gauge operators of interest in this thesis, such limits typically arise from electroweak precision data or the measurement of triple gauge interactions at the LHC [43]. For instance, the operator $\mathcal{O}_W$ as defined in (2.31) contributes to the ZWW and WWW vertices. Their measurement at the LHC gives the limits

$$-5.4\ \text{TeV}^{-2} < \frac{c_W}{\Lambda^2} < 9.8\ \text{TeV}^{-2} \tag{2.34}$$

at 90% CL [43]. There are no strong constraints from electroweak precision measurements, because the loop contributions from this operator can be balanced by other operators, making this operator a so-called 'blind direction' [44]. The operator $\mathcal{O}_{\phi,2}$ as defined in (2.32) only affects Higgs interactions and is constrained to

$$-9.8\ \text{TeV}^{-2} < \frac{c_{\phi,2}}{\Lambda^2} < 7.5\ \text{TeV}^{-2} \tag{2.35}$$

at 90% CL [43].

The discovery of a Higgs-like boson and the first measurements of its properties have provided some exciting insight into the structure of the electroweak sector, but there are still many open questions. Understanding the nature of electroweak symmetry breaking is one of the most important tasks for the upcoming run 2 of the LHC. The Higgs discovery has given us the Higgs-gauge sector and thus opens new possibilities to tackle this question. It provides an ideal laboratory for various reasons: on the one hand, the Higgs mechanism is responsible for the W and Z masses, and the interplay of the Higgs and the Goldstone modes inside the W and Z bosons is intimately linked to the structure of electroweak symmetry breaking. On the other hand, the scalar nature of the Higgs boson is responsible for the troublesome hierarchy problem. The question is not *if* the Higgs-gauge sector needs further exploration – it is *how* to probe the Higgs-gauge sector and thus the details of the electroweak sector at the LHC experiments.

2.2. The polarisation of gauge bosons

The handle to the electroweak sector that we will focus on during this thesis is the polarisation of the massive vector bosons $W^{\pm}$ and Z. In this section we will define the longitudinal and transverse modes and explain their link to electroweak symmetry breaking and thus their relevance.

2.2.1. Counting degrees of freedom

Massless gauge bosons

First, let us consider massless gauge bosons. As an example we will use the free photon field. Its Lagrangian is given by

$$\mathcal{L}_{\text{Maxwell}} = -\frac{1}{4} F^{\mu\nu} F_{\mu\nu} \tag{2.36}$$

with field strength $F_{\mu\nu} = \partial_\mu A_\nu(x) - \partial_\nu A_\mu(x)$. The corresponding equations of motion are the Maxwell equations

$$\partial_\mu F^{\mu\nu} = 0\,. \tag{2.37}$$

The theory is invariant under a U(1) gauge symmetry acting on A_μ as

$$A_\mu(x) \to A_\mu(x) - \partial_\mu \Lambda(x)\,. \tag{2.38}$$

Now we would like to know how many degrees of freedom this photon field has. This question is best answered in momentum space. Here the field equations read

$$k^2 A_\mu(k) - k_\mu k^\nu A_\nu(k) = 0. \tag{2.39}$$

It is instructive to analyse the implications on the light cone and away from it separately:

- For off-shell momenta, i. e. $k^2 \neq 0$, one can use the gauge freedom to choose the *Lorenz gauge* by requiring $k_\mu A^\mu(k) = 0$. Then the Maxwell equation (2.39) implies

$$A_\mu(k) = 0. \tag{2.40}$$

  In other words, by fixing the gauge outside of the light cone, the free photon field is restricted to the light cone.

- On the light-cone, i. e. where $k^2 = 0$, the Maxwell equations (2.39) give the *four-transversality condition*

$$k_\mu A^\mu(k) = 0 \tag{2.41}$$

  without needing to fix the gauge. This result is 'for free' and we can still use the gauge invariance to impose a gauge of our choice. A common choice is the radiation gauge $A_0(k) = 0$. This is equivalent to the *three-transversality condition*

$$k_i A^i(k) = 0, \tag{2.42}$$

  where the index i only runs over the spatial indices.

So in this choice of gauge, the photon field only exists on the light cone, where the four components of A^μ are restricted by two transversality conditions.[2] Hence, there are two degrees of freedom per space-time (or momentum-space) point.

These degrees of freedom are usually expressed as plane waves with constant polarisation vectors,

$$A^\mu(x) = \varepsilon^\mu \exp(-\mathrm{i}k \cdot x)\,, \tag{2.43}$$

where the transversality conditions read $k \cdot \varepsilon = 0$ and $\mathbf{k} \cdot \boldsymbol{\varepsilon} = 0$. For a photon propagating in z direction, $k_\mu = (E, 0, 0, E)^\mu$, a commonly used basis for the polarisation vector ε are the helicity eigenstates

$$\varepsilon_+^\mu = \frac{1}{\sqrt{2}}(0, 1, \mathrm{i}, 0)^\mu\,, \tag{2.44}$$

$$\varepsilon_-^\mu = \frac{1}{\sqrt{2}}(0, 1, -\mathrm{i}, 0)^\mu\,. \tag{2.45}$$

Both are what we will call transversely polarised: their spatial part is orthogonal to $\mathbf{k}$, as required by (2.42). These two modes are democratic, there is no fundamental difference between them.

[2] In the words of Kelogg Stelle, 'the gauge condition shoots twice' [45].

Massive vector bosons

In contrast to this, consider a free massive vector boson:

$$\mathcal{L}_{\text{Proca}} = -\frac{1}{4}F^{\mu\nu}F_{\mu\nu} - \frac{m^2}{2}A_\mu A^\mu \,. \tag{2.46}$$

This Proca theory leads to the field equation

$$\partial_\mu F^{\mu\nu} - m^2 A^\nu = 0 \,. \tag{2.47}$$

Note that this equation is not gauge invariant: the mass term breaks the U(1) symmetry of Maxwell theory.

Again, let us count the degrees of freedom. In momentum space, the equation of motion reads $-k^2 A^\nu + k^\nu k_\mu A^\mu - m^2 A^\nu$. Multiplying this with k_ν yields

$$k_\mu A^\mu(k) = 0 \,, \tag{2.48}$$

which is the same four-transversality condition found for massless gauge bosons. However, without a gauge symmetry there are no further requirements that can be imposed on A^μ. So for a massive vector boson, there are three degrees of freedom per space-time (or momentum-space) point.

For a massive boson propagating in z direction, $k_\mu = (E, 0, 0, k_3)^\mu$ with $k^2 = m^2$, a popular basis for the polarisation vector consists of the two transverse modes

$$\varepsilon_+^\mu = \frac{1}{\sqrt{2}}(0, 1, \mathrm{i}, 0)^\mu \,, \tag{2.49}$$

$$\varepsilon_-^\mu = \frac{1}{\sqrt{2}}(0, 1, -\mathrm{i}, 0)^\mu \,, \tag{2.50}$$

and an additional longitudinal mode

$$\varepsilon_L^\mu = \frac{1}{m}(k_3, 0, 0, E)^\mu \,. \tag{2.51}$$

Again, the designations ‘transverse’ and ‘longitudinal’ refer to the scalar product of the spatial components $\mathbf{k}$ and $\boldsymbol{\varepsilon}$ only. The four-transversality condition (2.48), on the other hand, is always satisfied by on-shell vector bosons.

Clearly, there is a difference between the transverse polarisation vectors (2.49) and (2.50) on the one hand and the longitudinal polarisation (2.51) on the other hand: while the former have components of order 1, the latter has components of order E/m. Therefore, at energies $E \gg m$ one expects that longitudinal gauge bosons dominate over transverse modes. This is the first hint at a fundamental difference between longitudinal and transverse gauge bosons.

Electroweak symmetry breaking

With these results it is straightforward to count the degrees of freedom in the electroweak sector before and after electroweak symmetry breaking. One begins with four gauge bosons, namely the B and the three instances of W^i. They are massless, so each of them has two polarisation states, summing up to a total of eight degrees of freedom per space-time point. After electroweak symmetry breaking, these fields have transformed into the massless photon and the now massive bosons W^+, W^- and Z. While the photon has two polarisation states, each of the massive vector bosons contributes three degrees of freedom, so there are now eleven degrees of freedom between these bosons.

Of course, these three additional degrees of freedom do not just appear out of nowhere. They come from the three Goldstone bosons, which combine with the original gauge bosons to form the massive vector bosons as given in (2.18) to (2.19). By incorporating these scalar fields, the gauge bosons do not only acquire a mass, but also gain a third, longitudinal polarisation. Since the Goldstone bosons are scalars, each of them brings one degree of freedom to the table. Hence there is a total of eleven real degrees of freedom per space-time point, both before and after electroweak symmetry breaking. In a sense, the longitudinal modes of the massive gauge bosons stem from the Goldstone bosons of electroweak symmetry breaking. This connection will be the topic of section 2.2.3.

2.2.2. Defining longitudinal and transverse modes

For on-shell W and Z bosons, i. e. for external legs in amplitude calculations, the definition of transverse and longitudinal states in (2.49) to (2.51) is sufficient. In real-life processes, though, these bosons can always leave the mass shell. This is obvious for decays of the 125 GeV Higgs to a pair of massive gauge bosons, where typically one of the gauge bosons is close to the mass shell, while the other is far off-shell. But also in other kinematic regimes, the large widths of the W and Z bosons mean that they can easily leave the mass shell by a few GeV. Finally, t-channel W and Z bosons are always far off-shell.

To be able to treat all these cases, we have to define polarisation states for on-shell and off-shell vector bosons alike. We define the transverse part and longitudinal parts of the W- and Z-boson fields as

$$V_T^\mu = \mathbb{P}_T{}^\mu_\nu \, V^\nu \tag{2.52}$$

$$V_L^\mu = \mathbb{P}_L{}^\mu_\nu \, V^\nu \tag{2.53}$$

where $V = W, Z$ is the gauge boson field in unitary gauge. $\mathbb{P}_T$ is the projection operator to the transverse plane,

$$\mathbb{P}_T{}^0_\mu = 0 = \mathbb{P}_T{}^\mu_0 \,, \tag{2.54}$$

$$\mathbb{P}_T{}^i_j = \delta^i_j - \frac{\mathbf{p}^i \mathbf{p}_j}{\mathbf{p}^2} \,, \tag{2.55}$$

with $i, j = 1, 2, 3$. The longitudinal projection operator is then

$$\mathbb{P}_{L\,\nu}^{\mu} = (\mathbb{1} - \mathbb{P}_T)_{\nu}^{\mu} \,. \tag{2.56}$$

For a (potentially off-shell) W boson with momentum $k^\mu = (E, 0, 0, k_3)^\mu$, this transverse projection operator takes on the form

$$\mathbb{P}_{T\,\nu}^{\mu} = \begin{pmatrix} 0 & 0 & 0 & 0 \\ 0 & 1 & 0 & 0 \\ 0 & 0 & 1 & 0 \\ 0 & 0 & 0 & 0 \end{pmatrix} \tag{2.57}$$

and the longitudinal projection operator becomes

$$\mathbb{P}_{L\,\nu}^{\mu} = \begin{pmatrix} 1 & 0 & 0 & 0 \\ 0 & 0 & 0 & 0 \\ 0 & 0 & 0 & 0 \\ 0 & 0 & 0 & 1 \end{pmatrix} \,. \tag{2.58}$$

In the case of on-shell W fields, these operators clearly project correctly onto the subspaces spanned by the basis (2.49) to (2.51).

Reference frame dependence

The definition of polarisation states in (2.52) and (2.53) requires the choice of a reference frame. In fact, boosting from one reference frame into another will induce a mixing of polarisations: longitudinal gauge bosons can become transverse and vice versa. The probability of such a change of polarisation depends on the size of the boost and on the direction of the boost relative to the gauge boson momentum.

To see this, consider again a W boson propagating in z direction. The corresponding transverse and longitudinal projectors are given in (2.57) and (2.58). A boost parallel to the W momentum is described by

$$\Lambda_{z\,\nu}^{\mu} = \begin{pmatrix} \gamma & 0 & 0 & \beta\gamma \\ 0 & 1 & 0 & 0 \\ 0 & 0 & 1 & 0 \\ \beta\gamma & 0 & 0 & \gamma \end{pmatrix} \,. \tag{2.59}$$

Clearly, Λ_z commutes with $\mathbb{P}_L$ and $\mathbb{P}_T$: boosts along the gauge boson momentum do not lead to a mixing of longitudinal and transverse momenta.

Boosts orthogonal to the W direction give a different result. For example a boost in x direction,

$$\Lambda_{x\,\nu}^{\mu} = \begin{pmatrix} \gamma & \beta\gamma & 0 & 0 \\ \beta\gamma & \gamma & 0 & 0 \\ 0 & 0 & 1 & 0 \\ 0 & 0 & 0 & 1 \end{pmatrix} \,, \tag{2.60}$$

does not commute with $\mathbb{P}_L$ or $\mathbb{P}_T$:

$$[\Lambda_x, \mathbb{P}_T]^\mu_\nu = \beta\gamma \begin{pmatrix} 0 & 1 & 0 & 0 \\ -1 & 0 & 0 & 0 \\ 0 & 0 & 0 & 0 \\ 0 & 0 & 0 & 0 \end{pmatrix} . \tag{2.61}$$

Gauge bosons that are longitudinal in one frame may be (partially) transverse in the other frame and vice versa. Assuming a quantum mechanical polarisation measurement after the boost, we can define the probability for a polarisation change. The commutator (2.61) suggests that this probability scales with the size of the boost as $\beta\gamma$. We will explicitly calculate the probabilities of this mixing for a specific case in section 4.5.1.

MadGraph implementation

We implement propagators for polarised W and Z fields into the Monte-Carlo event generation suite `MadGraph 5` [46]. This implementation will be used many times throughout this thesis. Unfortunately, the modular structure of the latest version of `MadGraph` makes the creation of a clean interface difficult. The current implementation therefore consists of new propagator structures in the matrix element calculation [47], which is based on the original `HELAS` library [48]. For each process, calls to these functions have to be added by hand. Our implementation allows the free choice of a reference frame for the definition of the polarisation.

2.2.3. The Goldstone boson equivalence theorem

Let us now come back to the difference between longitudinal and transverse gauge bosons. As discussed in section 2.2.1, the longitudinal modes of the W and Z boson appear when the Goldstone bosons w^i are incorporated into the gauge bosons. And already from the polarisation basis given in (2.49) to (2.51) it is obvious that longitudinal and transverse vector bosons are not created equal: at large energies, the longitudinal modes become dominant.

In fact, there is a fundamental difference between transverse and longitudinal states: in the limit of high energies, the latter correspond exactly to the Goldstone bosons of electroweak symmetry breaking. Conversely, in this limit the transverse modes represent the original, 'pure' gauge bosons.

To be more precise, consider a process involving external longitudinal $W^\pm$ or Z bosons with an energy scale E. In the limit $E \gg m_W$, the matrix element for this process can be calculated by exchanging all external electroweak bosons with the corresponding Goldstone bosons $w^\pm$, w^0 and using the Feynman rules for their scattering derived from

the Standard Model Lagrangian before electroweak symmetry breaking:

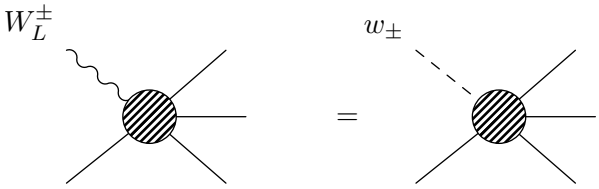

$$+\mathcal{O}\left(\frac{m_W}{E}\right). \tag{2.62}$$

This is the Goldstone boson equivalence theorem [7–9].

So what does all of this mean? At first, the longitudinal and transverse polarisation states appear to be just a basis for the solutions of the equations of motion of massive vector bosons. A more thorough investigation, however, reveals that there is a physical difference between these modes. In the high-energy limit, they can be clearly separated: the longitudinal states are equivalent to the Goldstone bosons of the Higgs sector, while the transverse modes correspond to the original electroweak gauge bosons.

In reality we have to analyse processes at finite energies, including off-shell as well as on-shell bosons. The separation between longitudinal and transverse modes is then less clean and depends on the reference frame. But this technical difficulty does not render the physical difference between transverse and longitudinal gauge bosons any less relevant. We view a separation of longitudinal and transverse gauge bosons as defined in (2.52) and (2.53) as a first step towards a separation of the original gauge bosons and the Goldstone bosons, the essential ingredients of electroweak symmetry breaking.

2.3. Gauge boson scattering

At the beginning of this chapter, the big theoretical question of interest was outlined, which is the nature of electroweak symmetry breaking. Then we discussed the tool we want to probe it with, namely the polarisation of massive gauge bosons. What is missing is a laboratory – a process where we can analyse the Higgs-gauge sector at the LHC.

In this section we introduce the scattering of massive vector bosons as such a laboratory. First we approach it from a theoretical perspective and explain the relevance of unitarity in this process. Then we focus on phenomenological aspects and give an overview of possible measurement strategies.

2.3.1. Gauge boson scattering and unitarity

Longitudinal WW scattering

Let us begin by analysing the scattering of longitudinal vector bosons with a special interest in the high-energy limit. We consider the exemplary process

$$W_L^+ W_L^- \to W_L^+ W_L^- . \tag{2.63}$$

Other initial and final states give similar results.

In the Standard Model, seven diagrams contribute to this process at tree level:

- the four-W interaction,
- s-channel diagrams with a photon, a Z, or a Higgs boson, and
- t-channel diagrams with a photon, a Z, or a Higgs boson.

The exact amplitude is rather involved. However, we are interested in the high-energy behaviour of this cross section, so we can use the Goldstone boson equivalence theorem to considerably simplify the calculation. The coupling of Goldstone bosons $w^\pm$ to other particles can be read off the Standard Model Lagrangian, see appendix A.1 for more details. The diagrams involving only Goldstone and Higgs bosons then yield the following expressions:

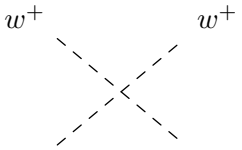

$$= \quad -4\mathrm{i}\lambda\,, \tag{2.64}$$

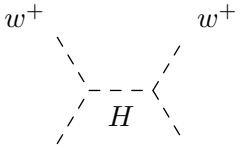

$$= \quad \frac{-4\mathrm{i}\lambda^2 v^2}{s - m_H^2}\,, \tag{2.65}$$

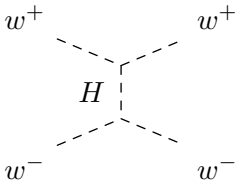

$$= \quad \frac{-4\mathrm{i}\lambda^2 v^2}{t - m_H^2}\,. \tag{2.66}$$

The γ and Z contributions turn out to be negligible. The total matrix element is then approximately

$$\mathcal{M}_{\mathrm{SM}}(W_L^+ W_L^- \to W_L^+ W_L^-) \approx \mathcal{M}_{\mathrm{SM}}(w^+ w^- \to w^+ w^-) \tag{2.67}$$

$$\approx -4\mathrm{i}\lambda - \frac{4\mathrm{i}\lambda^2 v^2}{s - m_H^2} - \frac{4\mathrm{i}\lambda^2 v^2}{t - m_H^2} \tag{2.68}$$

$$\approx -\mathrm{i}\frac{m_H^2}{v^2}\left[2 + \frac{m_H^2}{s - m_H^2} + \frac{m_H^2}{t - m_H^2}\right]. \tag{2.69}$$

In the high-energy limit of $s, |t| \gg m_H^2$, this expression becomes constant, so the cross section falls off proportional to

$$\sigma_{\text{SM}} \sim \frac{1}{s} \,. \tag{2.70}$$

In contrast, consider a scenario without a Higgs boson, which we emulate by taking the limit $m_H \to \infty$.[3] With $m_H^2 = 2\lambda v^2$ and $s, |t| \ll m_H^2$, the matrix element becomes

$$\mathcal{M}_{\text{Higgsless}}(W_L^+ W_L^- \to W_L^+ W_L^-) \approx -\mathrm{i}\frac{m_H^2}{v^2}\left[2 - \frac{1}{1-\frac{s}{m_H^2}} - \frac{1}{1-\frac{t}{m_H^2}}\right] \tag{2.71}$$

$$\approx \mathrm{i}\frac{s+t}{v^2} \,. \tag{2.72}$$

In the high-energy limit, the cross section is therefore proportional to

$$\sigma_{\text{Higgsless}} \sim s \,. \tag{2.73}$$

So we find that at high enough energy scales, the Higgsless amplitude becomes much larger than the full amplitude. In other words, there is a significant cancellation between the contributions from pure gauge diagrams and Higgs interactions.

Perturbative unitarity violation

This high-energy behaviour is not just an interesting curiosity, but has some important implications. A basic postulate of any quantum field theory is that the time evolution or equivalently the S-matrix is unitary. This can be reformulated in terms of the total cross section σ and the amplitude $\mathcal{M}$, giving the optical theorem

$$\sigma = \frac{1}{s} \operatorname{Im} \mathcal{M}_{\text{forward}} \,. \tag{2.74}$$

Here $\mathcal{M}_{\text{forward}}$ is the amplitude in the limit of identical final and initial states, i. e. in the case of extreme forward scattering.

It is immediately clear that the Higgsless cross section (2.73) violates the optical theorem. In the high-energy limit, the cross section increases with s, while the corresponding right-hand side of (2.74) remains constant. In other words, in leading perturbative order the Higgsless scenario violates the unitarity of the S-matrix. So either some effect of new physics has to restore the unitarity condition, or the leading contribution in perturbation theory does not describe the process well, making the WW system strongly interacting.

[3] In the derivation of the Feynman rules based on the equivalence theorem, we have effectively assumed the Standard Model structure including a Higgs boson. It is therefore not consistent to simply remove the Higgs contributions from the expression (2.69).

In order to estimate the energy scale at which such a mechanism has to appear to save perturbative unitarity, we expand the amplitude into partial waves in terms of the scattering angle θ:

$$\mathcal{M} = 16\pi \sum_l (2l+1) a_l P_l(\cos\theta)\,, \tag{2.75}$$

where θ is the scattering angle and P_l are the Legendre polynomials. In terms of the partial waves a_l, the cross-section reads

$$\sigma = \frac{16\pi}{s} \sum_l (2l+1) |a_l|^2\,. \tag{2.76}$$

The fundamental structure of QFT only requires the optical theorem (2.74) to hold for the full amplitudes $\mathcal{M}$, it does not say anything about the individual partial waves a_l. But if a partial wave on its own would violate the optical theorem, there would have to be large cancellations between the different partial waves, which would at least require a good explanation. Therefore any tasteful process should satisfy the optical theorem on the level of partial waves:

$$\frac{16\pi}{s}(2l+1)|a_l|^2 = \frac{1}{s} 16\pi (2l+1) \operatorname{Im} a_l \tag{2.77}$$

or

$$(\operatorname{Re} a_l)^2 + \left(\operatorname{Im} a_l - \frac{1}{2}\right)^2 = \frac{1}{4}\,. \tag{2.78}$$

In particular, this equation for a circle in the complex plane implies

$$|\operatorname{Re} a_l| < \frac{1}{2}\,. \tag{2.79}$$

Now let us impose this condition on the process of longitudinal $W^+W^- \to W^+W^-$ scattering. An expansion of the Standard Model amplitude (2.69) into multipoles gives the leading term [29]

$$a_0^{\mathrm{SM}} = \frac{m_H^2}{16\pi v^2}\left[2 + \frac{m_H^2}{s - m_H^2} - \frac{m_H^2}{s}\log\left(1 + \frac{s}{m_H^2}\right)\right]. \tag{2.80}$$

For $m_H = 125$ GeV, a_0^{SM} satisfies the perturbative unitarity inequality (2.79) up to arbitrarily high energies. Including higher partial waves gives similar results. With the observed value for the Higgs mass, the Standard Model is thus perfectly consistent and does not cause any problems with perturbative unitarity [8, 10–12].

The situation is different for the Higgsless scenario. Here the first partial wave reads

$$a_0^{\text{Higgsless}} = -\frac{s}{32\pi v^2}\,, \tag{2.81}$$

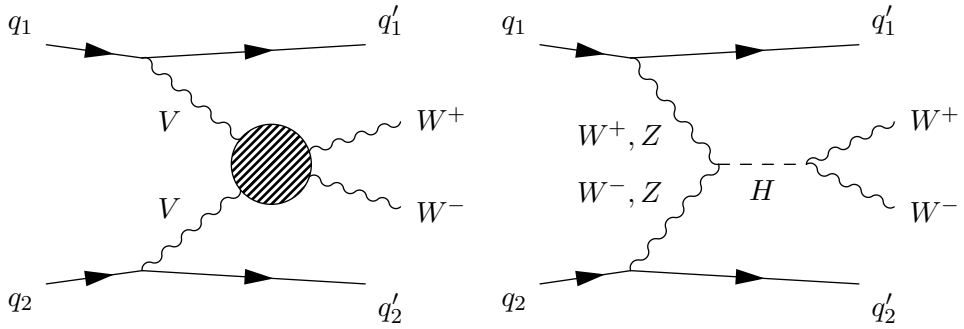

Figure 2.1.: Left: prototypical $VV \to W^+W^-$ scattering diagram, $V = \gamma, W^\pm, Z$. Right: s-channel Higgs diagram, which is the dominant contribution to gauge boson scattering at $m_{WW} \approx m_H$.

reflecting the increase of the full amplitude proportional to $(s+t)$. Perturbative unitarity therefore requires

$$\sqrt{s} \lesssim \sqrt{32\pi}v \approx 1.7 \text{ TeV} \,. \tag{2.82}$$

A more thorough calculation involving all diagrams and higher-order corrections gives a slightly lower bound of the order $\sqrt{s} \lesssim 1.2$ TeV [29].

So without a Higgs boson, perturbative unitarity is violated around the TeV scale. This means that some mechanism has to unitarise the scattering amplitude, and its effect should be visible at LHC energies. This was the reasoning behind the no-lose prediction for the LHC: either a Higgs boson would be found, or some new effect would have to appear around the TeV scale that unitarises the scattering of weak bosons. The latter scenario is known as *strongly interacting WW scattering* [13–20].

With the discovery of a Higgs-like boson, the Higgsless scenario became of course less relevant. Instead one can consider *partially strong WW scattering* [21–24]: if the coupling of longitudinal W or Z bosons to the Higgs boson deviates from the Standard Model, there is an increase of the cross section at larger energies, eventually violating unitarity. However, compared to the Higgsless case this increase is less pronounced and shifted to higher energy scales, which may or may not be accessible at the LHC. Therefore the unitarity argument has lost its urgency after the Higgs discovery.

2.3.2. Anatomy of the full process at the LHC

In reality there is no W^+W^- collider, unfortunately. The currently best place to probe gauge boson scattering is the LHC, where the relevant full process is

$$pp \to W^+W^- \, jj \,, \tag{2.83}$$

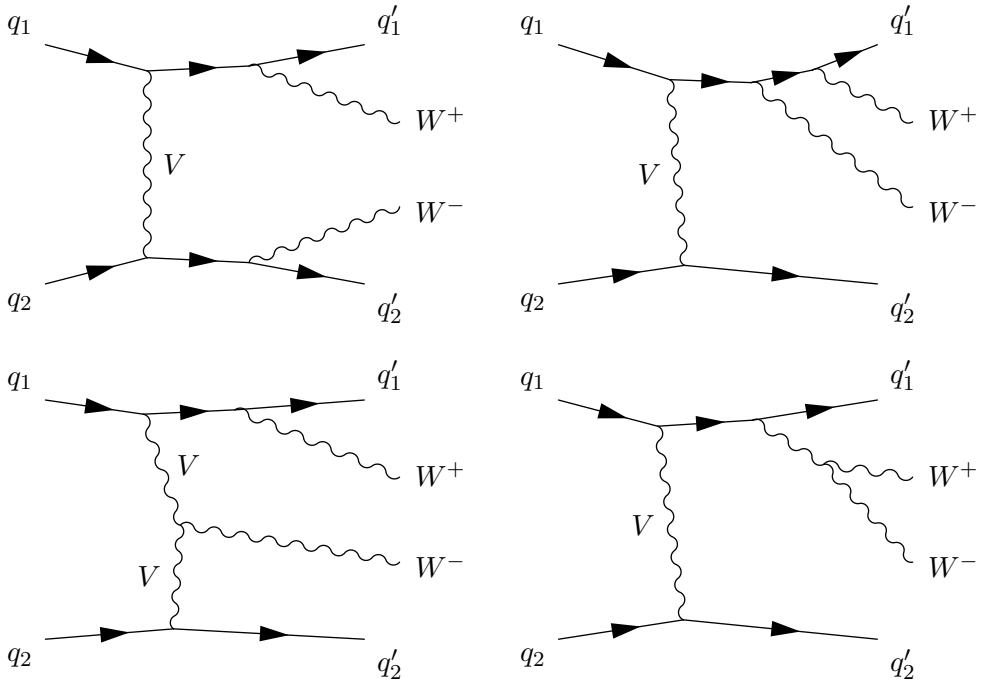

Figure 2.2.: Exemplary bremsstrahlung diagrams contributing to the process $pp \to W^+W^- jj$. Again $V = \gamma, W^\pm, Z$.

followed by leptonic or hadronic W decays. Again, the analysis of other diboson final states gives comparable results.

The amplitudes contributing to the process (2.83) at the leading electroweak order $\mathcal{O}(\alpha^4)$ can be grouped into two categories. First, there are $VV \to W^+W^-$ diagrams, where $V = \gamma, W^\pm, Z$, as given in the left panel of figure 2.1. This class of processes is similar to the pure gauge bosons amplitudes discussed above, and in fact we will find that many features expected for $W^+W^- \to W^+W^-$ scattering appear in the full process (2.83) as well. In particular, the Higgs contributions will again play a crucial role. The right panel of figure 2.1 shows the s-channel Higgs diagram, which dominates the full amplitude in the kinematic regime around a diboson mass $m_{WW} \approx m_H$. The main difference to the scattering process discussed in the previous section is that the initial gauge bosons are now not on-shell anymore, but have a t-channel topology.

The second contribution to (2.83) is due to bremsstrahlung of various gauge bosons. There are four different types of diagrams:

1. The two quark lines exchange a $\gamma, W^\pm$, or Z boson. In addition, a W boson is radiated off each of the two quark lines. See the top left panel of figure 2.2.

Leptonic cuts	Jet cuts
$\lvert\eta_\ell\rvert < 2.5$	$\lvert\eta_j\rvert < 5.0$
$p_{T,\ell} > 20$, 10 GeV	$p_{T,j} > 25$ GeV
	$m_{jj} > 500$ GeV
	$\eta_{j1} \cdot \eta_{j2} < 0$
$p_T^{\text{miss}} > 20$ GeV	$\Delta\eta_{jj} > 4.2$

Table 2.2.: Generic cuts used for the analysis of the interference structure of W^+W^- scattering.

Parameter	Value
Collider setup	pp collisions at $\sqrt{s} = 14$ TeV
m_H	125 GeV
Number of events	10,000 each
Parton density function	CTEQ6L [49]

Table 2.3.: Parameters used for the analysis of the interference structure of W^+W^- scattering.

2. The two quark lines exchange a $\gamma, W^\pm$, or Z boson. In addition, two W bosons are radiated off the same quark line. See the top right panel of figure 2.2.

3. Each quark line emits one gauge boson, which then fuse into a W. The second final W is radiated off one of the two quark lines. See the bottom left panel of figure 2.2.

4. The two quark lines exchange a $\gamma, W^\pm$, or Z boson. In addition, a γ or Z boson is radiated off a quark line and splits into a W^+W^- pair. See the bottom right panel of figure 2.2.

The contributions from $VV \to W^+W^-$ scattering and bremsstrahlung diagrams inevitably interfere with each other. We now analyse this interference quantitatively. For this we calculate the cross section for the process (2.83) with a decay cascade $W^+ \to \mu^+\nu_\mu$, $W^- \to e^-\bar{\nu}_e$ in `MadGraph 5`. For simplicity, only the dominant ud initial states are taken into account and the CKM matrix is set to the unit matrix. Acceptance cuts based on the ATLAS and CMS detectors are used and two tagging jets with an invariant mass of 500 GeV between them and a separation in pseudorapidity of 4.2 are required. All settings and cuts are given in table 2.2 and table 2.3. In this setup we evaluate the full process as well as the process based on certain diagrams only.

In table 2.4 we give the resulting cross sections. We find that there is a significant cancellation between the $VV \to W^+W^-$ scattering diagrams and the bremsstrahlung

Diagrams taken into account	Cross section [fb]
All diagrams	0.6
Only $VV \to W^+W^-$ diagrams (c. f. figure 2.1)	35.1
Only bremsstrahlung diagrams (c. f. figure 2.2)	35.0
Only $W^+W^- \to W^+W^-$ diagrams	17.7
Only $ZZ \to W^+W^-$ diagrams	6.9
Only $Z\gamma \to W^+W^-$ diagrams	3.9
Only $\gamma\gamma \to W^+W^-$ diagrams	0.2
Only bremsstrahlung diagrams of type 1	44.7
Only bremsstrahlung diagrams of type 2	44.2
Only bremsstrahlung diagrams of type 3	110.8
Only bremsstrahlung diagrams of type 4	6.6

Table 2.4.: Cross sections for the full process $ud \to W^+W^- \, jj \to (\mu^+\nu_\mu) \, (e^-\bar{\nu}_e) \, jj$ and for subprocesses limited to certain diagrams. The statistical uncertainties are irrelevant compared to the differences between the different cross sections. The categorisation of bremsstrahlung diagrams is explained in the text.

diagrams. The cross section for either of these categories on its own is three orders of magnitude larger than the cross section of the full process. If the two categories are further split into smaller groups of diagrams, these interference effects become even worse.

These cancellations are known and explained by the fact that the individual expressions of the diagrams in figures 2.1 and 2.2 are not gauge invariant (i. e. invariant under the choice of ξ in the R_ξ gauge) on their own, only the sum of all such diagrams is [50]. Due to this interplay, an analysis can never be restricted to $VV \to VV$ diagrams, one always has to include all electroweak tree-level processes in the simulation.

In a next step we analyse how this interference depends on the phase space. In figure 2.3 we give the m_{WW} distribution for the full process as well as the separated $VV \to W^+W^-$ and bremsstrahlung contributions. Clearly, the cancellation effects become stronger at large energies. A thorough analysis of different kinematic variables reveals that this destructive interference extends throughout the whole phase space and cannot be removed by simple cuts. There is only one exception: the Higgs resonance, i. e. the region around $m_{WW} \approx m_H$, visible as the sharp line peak in figure 2.3. Here the s-channel Higgs amplitudes dominate over all other contributions to the amplitude, and the bremsstrahlung diagrams can safely be neglected.

In a nutshell, the full process $pp \to W^+W^- \, jj$ is not a simple extension of $W^+W^- \to W^+W^-$ scattering. First, the initial gauge bosons are virtual t-channel propagators instead of on-shell external legs. There are irreducible contributions from

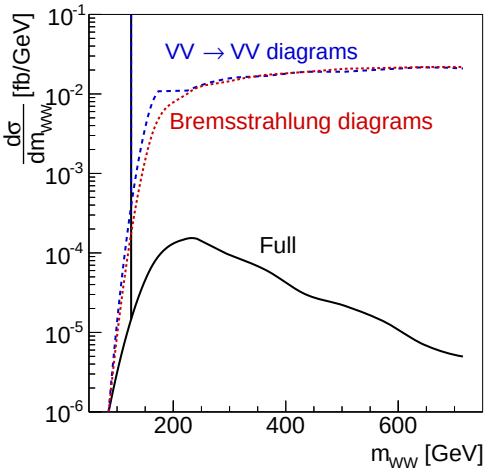

Figure 2.3.: The distribution of the energy scale m_{WW} in the full process $ud \to W^+W^- jj \to (\mu^+\nu_\mu)\,(e^-\bar{\nu}_e)\,jj$ and in subprocesses limited to certain diagrams.

$ZZ \to W^+W^-$, $Z\gamma \to W^+W^-$ and $\gamma\gamma \to W^+W^-$ diagrams. Most important, an analysis cannot be limited to the gauge boson scattering subprocesses, the large number of bremsstrahlung contributions have to be taken into account as well. Only this gives a consistent and gauge-invariant result. The only exception to this rule in the Standard Model is the Higgs resonance, where the s-channel Higgs contribution dominates.

2.3.3. The weak boson fusion signature

From a phenomenological point of view, not only the electroweak structure of gauge boson scattering is relevant, but also the efficient extraction of the relevant events from the vast amount of LHC data. We will first discuss the background processes, followed by the experimental signatures that we can use for their suppression.

Background processes

As discussed in the previous section, the electroweak bremsstrahlung contributions cannot be separated from the $VV \to VV$ subprocesses, so we consider the whole electroweak process as our signal. The relevant background processes depend on the final gauge bosons and their decay modes as well as on the kinematic region of interest. Typical backgrounds include the following:

- electroweak production of other $VV\,jj$ states,
- VV production with additional QCD jets (as in the top left panel of 2.4),

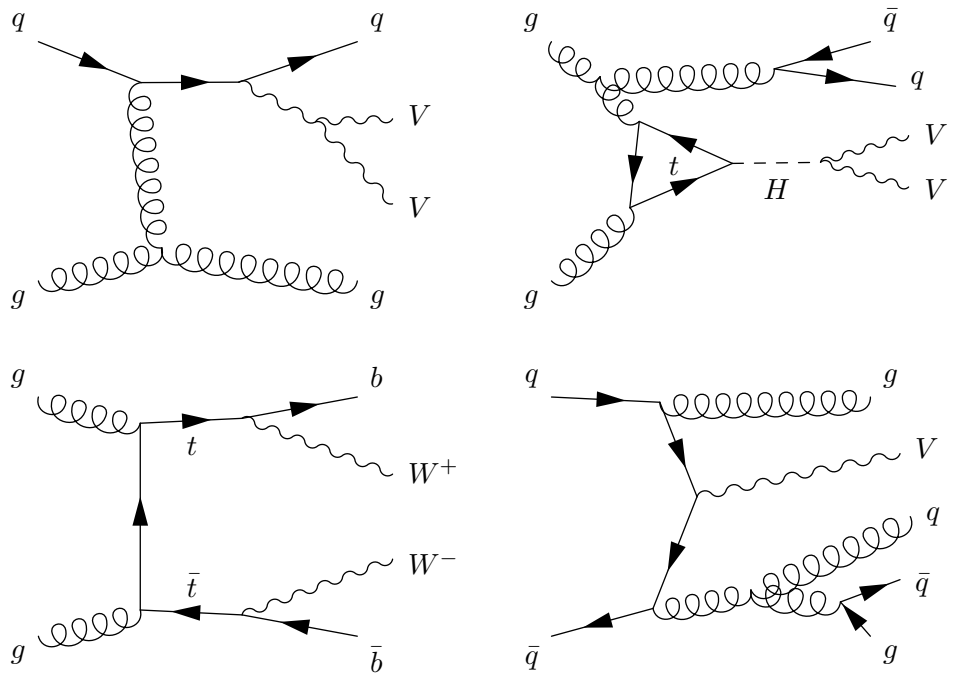

Figure 2.4.: Example diagrams for QCD backgrounds to electroweak gauge boson scattering.

- Higgs production in gluon fusion (c. f. the top right panel of figure 2.4),
- $t\bar{t}$ production (see for instance the bottom left panel of figure 2.4),
- $\tau^+\tau^-$ production, and
- $V +$ jets production (as in the bottom right panel of figure 2.4).

Generally, more classes of backgrounds are relevant for hadronic gauge boson decays than for leptonic modes, since QCD jets can mimic the hadronic decay products.

Decay products

The first part of the experimental signature of gauge boson scattering is the gauge boson pair itself, or more precisely, its decay products. These particles tend to hit the detector centrally, i. e. at low rapidities [29]. The details of the signature, of course, depend on the particular decay mode:

- A leptonically decaying Z boson leads to two leptons with an invariant mass $m_{\ell\ell} \approx m_Z$.[4]
- A leptonic W decay yields an isolated, central lepton and missing transverse momentum.
- Hadronic W and Z decays each give a pair of two central jets with an invariant mass compatible with the gauge boson mass.

Unfortunately, many of the background processes listed above involve gauge boson decays with just the same features.

Tagging jets

The signal process features two more final-state particles: the two quark lines that emit the initial gauge bosons. The initial quarks coming from the proton have very large energies dictated by the proton energy and the parton density functions for valence quarks, and are, at least in a first approximation, parallel to the beam line. The emission of a $W^\pm$ or Z boson only takes away energy of the order of the scale of the hard process. On the one hand, this implies that the jets coming from these final-state quarks still have very large energies. At the LHC the dijet mass m_{jj} can easily exceed 1 TeV. On the other hand, the low transverse momentum from the weak boson emission means that both jets are back-to-back and each jet points in forward direction. In other words, there is a large rapidity gap between them.

The appearance of these two *tagging jets* is unique to processes with a topology as in figure 2.1. Therefore the requirement of one or two such jets is a powerful tool that strongly suppresses many of the backgrounds.

Additional hadronic activity and the central jet veto

Another crucial phenomenological difference between the signal and background contributions is the level of additional hadronic activity. QCD background diagrams such as the ones shown in figure 2.4 all feature quark and gluon lines that can easily radiate off additional jets into the central detector region. A large fraction of background events therefore includes a number of central jets in addition to the two required tagging jets and the gauge boson decay products.

Signal events, on the other hand, typically do not feature any central jets, at least as long as all gauge boson decays are leptonic. In order to understand this lack of extra QCD radiation, consider corrections to the signal process by virtual gluon exchange first.

[4] On the Higgs resonance, one of the two gauge bosons is typically off its mass shell. Then this condition does not hold true anymore, but can be replaced with the condition that all decay products reconstruct the Higgs boson. We will discuss such kinematic features in section 3.3.2.

Usually, the leading-order correction to a tree-level amplitude is given by the interference between the tree-level process and the higher-order diagram. So for electroweak gauge boson scattering, the leading correction in α_s would be the interference between the diagram in figure 2.1 and the same diagram with an additional gluon exchange between the two quark lines. However, the colour structure of these two amplitudes is inherently different, and the interference term vanishes. This means that virtual gluon exchange is strongly suppressed by the colour structure of the signal process.

This in itself is not particularly relevant, but there is an intimate link between virtual gluon exchange and real gluon emission. The calculation of non-collinear gluon radiation and virtual gluon exchange each give an infrared divergence, and these two soft divergences cancel. So if there is no virtual gluon exchange in a process, there cannot be any non-collinear real gluon emission either. In other words, the suppression of virtual gluon exchange in our signal process implies that gluons are only radiated collinearly, i. e. along the beam line or the tagging jets. Baring hadronic gauge boson decays, there is very little hadronic activity in the central detector region.

The simplest strategy to use this difference between signal and background is the *central jet veto* [51–53]: discarding all events with central jets between the two tagging jets significantly reduces all QCD backgrounds without a large impact on the signal. More involved techniques do not simply throw away such events, but combine the information from the additional jets with other observables to optimise the signal acceptance and background rejection rates [54, 55]. Regardless of the specific implementation, the different jet radiation patterns between signal and background provide another powerful tool for the clean extraction of weak boson fusion signatures, at least as long as only leptonic gauge boson decays play a role.

2.3.4. Where to probe the Higgs-gauge sector

After analysing the structure of the gauge boson scattering amplitude and discussing the experimental features of this process at the LHC, we are now in a position to tackle the original question from the first two sections: how can the LHC experiments probe the Higgs-gauge sector, and more specifically the polarisation of the massive gauge bosons? There is more than one answer to this. In the following, we classify the possible strategies by the phase-space regime they probe and the observables they use.

Phase-space regime

The first choice is that of the phase-space regime one wants to probe. There are two well-motivated options:

1. The high-energy regime. In section 2.3.1 the scattering of longitudinal gauge bosons in the limit of large m_{VV} was analysed. It turned out that a Higgs-gauge

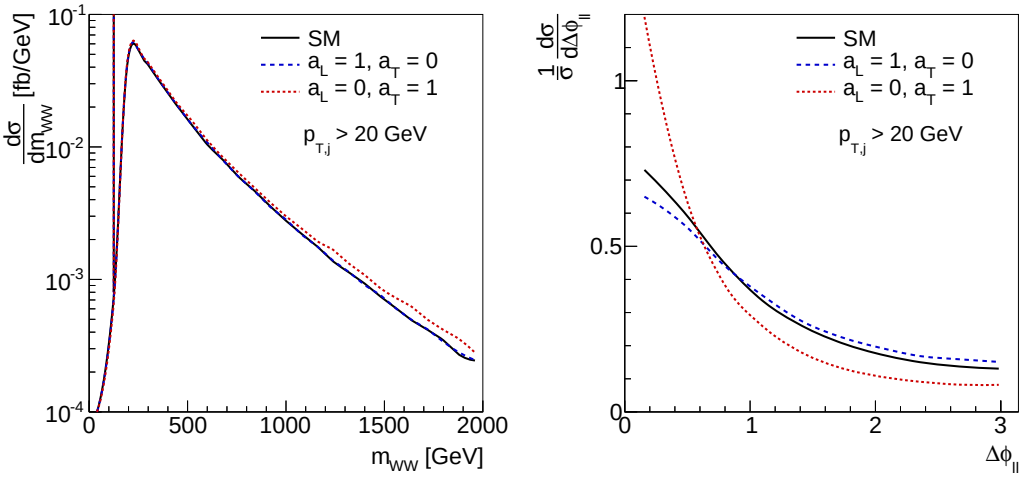

Figure 2.5.: Different approaches to the Higgs-gauge sector in the process $pp \to W^+W^- jj \to (\ell^+\nu)\,(\ell^-\bar{\nu})\,jj$. Left: distribution of m_{WW}. Right: azimuthal angle between the two leptons at the Higgs resonance. In both cases, the Standard Model is compared to scenarios with modified longitudinal Higgs-gauge couplings a_L and transverse Higgs-gauge couplings a_T, where $a_{L/T} = 1$ corresponds to the Standard Model coupling. For more details, see section 4.2. We require transverse jet momenta of 20 GeV to remove photon-exchange contributions.

coupling different from the Standard Model leads to an increase of the cross section at large energy scales, caused by the incomplete cancellation of Higgs and gauge amplitudes. This effect persists in the full process of gauge boson scattering in pp collisions. We demonstrate this in the left panel of figure 2.5, where we show the distribution of the invariant mass of the W^+W^- system for the Standard Model as well as for scenarios where the Higgs boson either couples only to transverse gauge bosons or only to longitudinal gauge bosons. At energies above 1 TeV, the missing longitudinal Higgs-gauge coupling induces a visible increase in the cross section. The transverse Higgs-gauge coupling, however, remains unaffected.

2. The Higgs resonance. The cross section and kinematics are clearly sensitive to the Higgs-gauge coupling structure in the region around $m_{VV} \approx m_H$, where the Higgs s-channel amplitude dominates the electroweak process. As discussed in section 2.3.2, this is the only region of the phase space without huge cancellations between gauge boson scattering and bremsstrahlung diagrams, which considerably simplifies the analysis.

Observables

In addition to total cross sections, the topology of weak boson scattering as shown in figure 2.1 provides two classes of kinematic observables:

1. Properties of the gauge boson decay products, which are sensitive to the final pair of gauge bosons. In particular, angular distributions of the decay products are sensitive to the polarisation of the final gauge bosons. The right panel of figure 2.5, for instance, shows the distribution of the azimuthal angle between the two leptons of the leptonic W^+W^- channel at the Higgs resonance. The Standard Model leads to a different distribution than models where the Higgs boson only couples to longitudinal or transverse gauge bosons.

2. Properties of the tagging jets, which probe the initial pair of gauge bosons. It is slightly less obvious than in the case of the decay products, but the tagging jets recoil against the initial gauge bosons and therefore carry information on their polarisation. At the Higgs pole, this approach is straightforward. Away from the resonance, however, the large interference between scattering and bremsstrahlung diagrams discussed in the previous section makes it hard to define initial gauge bosons.

Of course, correlations between these two sets of observables can also be of interest.

Analysis strategies

The classical approach to polarised gauge boson scattering is event counting in the high-energy regime. The separation of longitudinal and transverse gauge bosons is well established in these studies. For instance, in [13–15] analysis strategies to select highly energetic longitudinal gauge bosons are developed for all leptonic gauge boson topologies, including jet tagging, a central jet veto, and angular correlations between the decay products. The authors of [16] are the first to analyse the semileptonic W^+W^- channel and introduce the concept of boosted W tagging. The full set of semileptonic decay modes is discussed in [17–20]. High-energy gauge boson scattering is investigated in the context of a light Higgs boson with anomalous couplings to the gauge bosons in [21–23].

In [24] it was pointed out that such rate measurements at large energy scales suffer not only from low rates, but also from large systematic uncertainties due to scale ambiguities. The authors suggested measuring the polarisation of the final gauge bosons by fitting decay-angle distributions in the semileptonic WW channel. In such a relative measurement, the problematic theoretical uncertainties cancel. In chapter 3 of this thesis we will follow this idea and expand it to other gauge boson channels.

A second class of publications investigates the Higgs resonance in order to determine properties of the Higgs boson. Most studies focus on the cross section in order to measure the Higgs-gauge couplings [42], which have been interpreted in terms of effective field

theory [36, 43]. The kinematic properties of the Higgs-decay products and the tagging jets, in particular angular correlations, have been used in measurements of the Higgs spin and CP properties [41, 56–64]. In chapter 4 of this thesis we will propose a new strategy that uses the tagging jet kinematics at the Higgs resonance to measure the polarisation of the initial gauge bosons.

3. Polarisation measurements with decay angles

The most straightforward handle to the polarisation of gauge bosons are angular distributions in their decay products [65]. These observables are sensitive to the final pair of gauge bosons. This approach has the advantage of being independent of the model and the phase-space region, which means that it can be used both at the Higgs resonance and in the high-energy regime. Originally, this strategy was suggested in [24] for high-energy W^+W^- scattering with semileptonic decays. The authors found that such a relative measurement of longitudinal and transverse polarisations significantly reduces scale uncertainties as compared to the usual cut-and-count approach. But while the basic idea is straightforward, it is not easy to find an optimal channel for such an analysis at the LHC. In some topologies, neutrinos spoil the reconstruction of the decay angles, while other final states are plagued by low rates or large QCD backgrounds.

In this chapter we implement such a polarisation measurement for various diboson channels and briefly evaluate the prospects for its realisation. First, the angular distributions in the decays of longitudinal and transverse vector bosons are derived. Section 3.2 then gives an overview of the various VV channels. In section 3.3 we present our strategy to reconstruct decay angles and measure the final-state gauge boson polarisation. We give our results in section 3.4 and draw conclusions on the feasibility of such a strategy in section 3.5.

3.1. From polarised gauge bosons to decay angles

A straightforward tree-level calculation of the differential cross-section reveals that longitudinal W or Z bosons decay into two fermions according to the distribution

$$\frac{\mathrm{d}\sigma(V_L \to f_1 f_2)}{\mathrm{d}\cos\theta^*} \propto E_1^* E_2^* + \mathbf{p}^{*2}(1 - 2\cos^2\theta^*) + 2\frac{c_L c_R}{c_L^2 + c_R^2} m_1 m_2 \,. \tag{3.1}$$

Transverse gauge bosons are distributed according to

$$\frac{\mathrm{d}\sigma(V_T \to f_1 f_2)}{\mathrm{d}\cos\theta^*} \propto E_1^* E_2^* + \mathbf{p}^{*2}\cos^2\theta^* \pm \frac{c_L^2 - c_R^2}{c_L^2 + c_R^2}(E_1^* + E_2^*)\,|\mathbf{p}^*|\,\cos\theta^* + 2\frac{c_L c_R}{c_L^2 + c_R^2} m_1 m_2 \,. \tag{3.2}$$

Here θ^* is the angle between the fermion direction in the V rest frame and the direction of V ($V = W, Z$ throughout this chapter).[1] c_L and c_R are the couplings of V to the left-handed and right-handed fermions in question. m_V, m_1 and m_2 are the masses of the gauge boson and its decay products. Finally, the energies and spatial momenta of the fermions in the V rest frame, E_1^*, E_2^*, $\mathbf{p}^*$ and $-\mathbf{p}^*$, are fixed by energy-momentum conservation to

$$E_1^* = \frac{m_V^2 + m_1^2 - m_2^2}{2m_V}\,, \tag{3.3}$$

$$E_2^* = \frac{m_V^2 + m_2^2 - m_1^2}{2m_V}\,, \tag{3.4}$$

$$|\mathbf{p}^*| = \frac{1}{2} m_V \lambda^{\frac{1}{2}}\Big(1, \frac{m_1^2}{m_V^2}, \frac{m_2^2}{m_V^2}\Big) \tag{3.5}$$

with the usual kinematic function

$$\lambda(x, y, z) = x^2 + y^2 + z^2 - 2xy - 2yz - 2xz\,. \tag{3.6}$$

For W bosons, which couple only to left-handed particles, and in the limit of massless fermions, the distributions simplify considerably and give the more familiar results

$$\frac{1}{\sigma}\frac{\mathrm{d}\sigma(V_L \to f_1 f_2)}{\mathrm{d}\cos\theta^*} = \frac{3}{4}(1 - \cos^2\theta^*)\,, \tag{3.7}$$

$$\frac{1}{\sigma}\frac{\mathrm{d}\sigma(V_T \to f_1 f_2)}{\mathrm{d}\cos\theta^*} = \frac{3}{8}(1 \pm \cos\theta^*)^2. \tag{3.8}$$

Figure 3.1 shows the expected angular distributions of a leptonic W decay as well as a Z decay into an $u\bar{u}$ pair.

A detailed derivation of (3.1) and (3.2) can be found in appendix A.2. These distributions are exact only at tree level. QCD corrections to the decays into quarks are of order $\mathcal{O}(1\%)$ [66] and should not be relevant for the general procedure developed here.

The distributions (3.1) to (3.2) are the main ingredient for the measurement strategy discussed in this section: after collecting enough events with VV decays, we can fit these distributions to data and thus determine the relative fractions of longitudinal and transverse gauge bosons. This strategy should significantly reduce scale uncertainties compared to cut-and-count searches for highly energetic longitudinal gauge bosons [24].

3.2. Gauge boson channels at the LHC

Fitting the distributions presented in the previous section to gauge boson data at the LHC is straightforward from a theoretical perspective. The situation becomes more

[1] Note that the angle θ^* depends on the choice of reference frame. While it is invariant under boosts along the momentum of V, it changes with any other boost. This corresponds to the reference frame dependence of the polarisation of gauge bosons discussed in section 2.2.2, as it must.

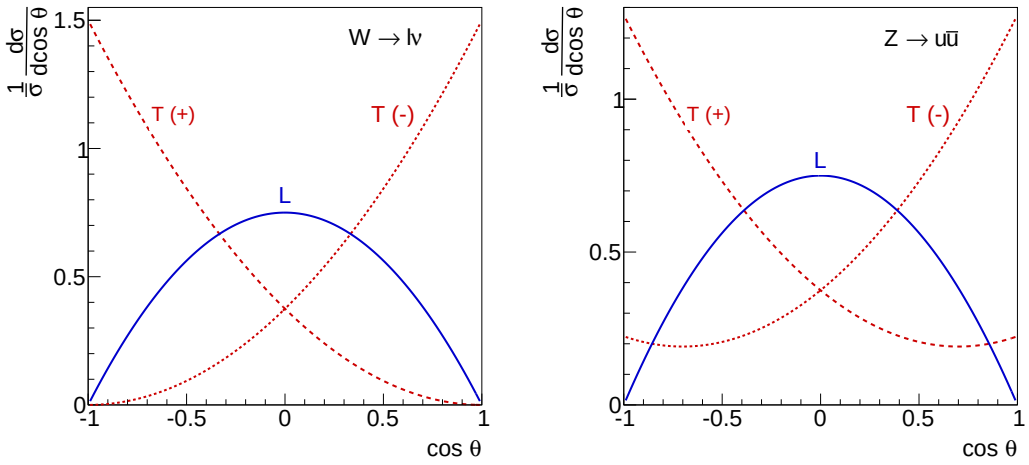

Figure 3.1.: Expected angular distribution in different V decays. Left: leptonic W decay. Right: Z boson decaying into $u\bar{u}$ pair.

complicated, though, when we try to pick a specific VV decay channel. So let us take a step back and have a look at the different diboson states and their decay modes at the LHC.

The four different VV states W^+W^-, $W^\pm W^\pm$, $W^\pm Z$ and ZZ and their various leptonic, semileptonic and hadronic decay channels each feature distinct rates, backgrounds and kinematic properties. They are also sensitive to different models of new physics. It is by no means obvious which of them are suited for a polarisation analysis at the LHC. Only the purely hadronic channels are easy to dismiss. While their rates are large, they yield a final state consisting of six jets without any leptons or missing transverse energy. Of course, the QCD background to this 'signature' is overwhelming.

This leaves five leptonic channels,

$$\begin{aligned} W^+W^- &\to (\ell^+\nu)\,(\ell^-\bar{\nu})\,, \\ W^\pm W^\pm &\to (\ell^\pm\nu)\,(\ell^\pm\nu)\,, \\ WZ &\to (\ell^\pm\nu)\,(\ell^+\ell^-)\,, \\ ZZ &\to (\ell^+\ell^-)\,(\ell^+\ell^-)\,, \\ ZZ &\to (\ell^+\ell^-)\,(\nu\bar{\nu})\,, \end{aligned} \tag{3.9}$$

and four semileptonic channels,

$$\begin{aligned} WW &\to (\ell^{\pm}\nu)\,(jj)\,, \\ WZ &\to (\ell^{\pm}\nu)\,(jj)\,, \\ WZ &\to (jj)\,(\ell^{+}\ell^{-})\,, \\ ZZ &\to (\ell^{+}\ell^{-})\,(jj)\,. \end{aligned} \tag{3.10}$$

Here ℓ denotes an electron or muon, ν any (anti-)neutrino, and j denotes a jet coming from an u, d, c or s quark. We do not consider τ leptons and b jets. This is because τ decays involve either neutrinos or jets, in both cases making the analysis more complicated, and because the b jets would fall victim to a b-jet veto, which is necessary to reduce top backgrounds as discussed in section 2.3.3.

For a polarisation measurement by decay-angle fits, a channel has to satisfy three criteria:

- Its rate has to be large enough for sufficient statistics to be collected at the LHC. Here W bosons generally fare better than Z bosons due to the larger production cross-section and larger leptonic branching ratio.
- QCD and other backgrounds are sufficiently small. This is especially problematic for semileptonic states due to the large QCD background.
- The relevant kinematic properties of the V bosons can be reconstructed from their measurable decay daughters with sufficient precision. This will be a crucial point for all states involving neutrinos, especially for the leptonic WW states, which feature two neutrinos.

In this chapter we answer the question which of the eight channels given in (3.9) to (3.10) satisfy these three criteria.

3.3. Analysis strategy

3.3.1. Event generation

We generate event samples with `MadGraph 5` for each channel in (3.9) and (3.10), including all tree-level electroweak diagrams at leading perturbative order $\mathcal{O}(\alpha^4)$. For simplicity, we limit ourselves to the parton level and do not simulate QCD backgrounds.

Inspired by the design of the ATLAS and CMS detectors [67–69] and various analyses [70–72], we impose the typical weak boson fusion selection cuts given in table 3.1. Most important is the requirement of two tagging jets in opposite hemispheres with an invariant mass of $m_{j1,j2} > 500$ GeV between them and a separation in pseudorapidity of $\Delta\eta_{j1,j2} > 4.2$. These cuts are designed to suppress QCD backgrounds to a manageable

Leptonic cuts	Jet cuts
$\lvert\eta_\ell\rvert < 2.5$	$\lvert\eta_j\rvert < 5.0$
$p_{T,\ell} > 20$, 10 GeV	$p_{T,j} > 25$ GeV
	$m_{j1,j2} > 500$ GeV
	$\eta_{j1} \cdot \eta_{j2} < 0$
($p_T^{\text{miss}} > 20$ GeV)	$\Delta\eta_{j1,j2} > 4.2$

Table 3.1.: Generic acceptance cuts applied in this chapter. The cut on p_T^{miss} is only applied in the channels involving neutrinos.

Parameter	Value
Collider setup	pp collisions at $\sqrt{s} = 13$ TeV
m_H	125 GeV
Number of events	100,000 each
Parton density function	CTEQ6L [49]

Table 3.2.: Parameters used in the event generation for the final-state polarisation measurements.

level, as discussed in section 2.3.3. Other settings for the event generation can be found in table 3.2.

We also generate event samples limited to specific polarisations of the final vector bosons. This will later allow for a sanity check of our analysis strategy. For this purpose, polarisations are defined in the laboratory frame following the definitions in section 2.2.2.

3.3.2. Event reconstruction

In this chapter we aim to measure the gauge boson polarisation by means of the decay angle θ^*, for which we rely on the knowledge of the four-momenta of the decaying V bosons. For Z bosons decaying leptonically or hadronically, and for hadronic W decays, this is not a problem. The energies and momenta of the resulting jets and charged leptons can be measured quite precisely in a detector such as ATLAS or CMS. By analysing the flavours and charges of leptons as well as the invariant mass of lepton and jet pairings, it can be determined which pair originated from which vector boson and what its momentum was.

The decay of a ZZ state into a pair of leptons and a pair of neutrinos is a special case: the leptonic Z boson can be reconstructed precisely, while the neutrinos only let us measure the sum of their transverse momenta in form of the missing transverse momentum. Here we simply ignore this invisible Z decay.

In leptonic W decays, however, we cannot neglect the neutrinos. These events can still be reconstructed approximately, but this procedure introduces an intrinsic uncertainty and relies on certain assumptions. In this analysis we will distinguish two phase-space regions and prescribe different reconstruction procedures. In the first scenario, we assume both vector bosons to be on the mass shell. This is a good approximation for VV pairs above the $m_{VV} > 2m_V$ threshold. In the second scenario, we assume the VV pair to stem from the decay of an on-shell Higgs boson with $m_H < 2m_V$. In the following the reconstruction procedures for leptonic W decays are presented for both scenarios.

Both vector bosons on shell

As long as only one leptonic W decay takes place in an event, and neglecting experimental uncertainties, the measurable total missing transverse momentum $\mathbf{p}_T^{\text{miss}}$ is equal to the transverse momentum of the neutrino. The remaining longitudinal component of its momentum can be reconstructed by postulating the W on-shell condition

$$(p_\ell + p_\nu)^2 = m_W^2 \,. \tag{3.11}$$

This quadratic equation gives two solutions for the missing component of p_ν, in the following denoted by $p_{z,\nu}^{(1)}$ and $p_{z,\nu}^{(2)}$. Hence the neutrino four-momentum can be reconstructed to be one of two solutions

$$p_\nu^{(k)\,\mu} = \left(\sqrt{\mathbf{p}_T^{\text{miss}\,2} + p_{z,\nu}^{(k)\,2}}, \mathbf{p}_T^{\text{miss}\,2}, p_{z,\nu}^{(k)\,2}\right)^\mu \tag{3.12}$$

with $k = 1, 2$. In this analysis, we use both solutions, with an appropriately reduced event weight and corrected statistical uncertainties. We find that this approach leads to better results than either averaging (as in [24]) or just using one solution (as in [70]). Events where the on-shell condition 3.11 has no solutions are rejected.

For the fully leptonic WW states this procedure does not work. Two neutrinos escape the detector, and only the sum of their transverse momenta is measurable as missing transverse momentum. An exact reconstruction of the true ν momenta $p_{\nu 1}^\mu$ and $p_{\nu 2}^\mu$ is therefore impossible. Fortunately, observable quantities contain enough information for an approximate reconstruction. For such topologies, i. e. two massive particles, each decaying into one observable and one undetectable daughter, it is common to calculate the variable

$$m_{T2} = \min_{\tilde{\mathbf{p}}_{T,\nu 1} + \tilde{\mathbf{p}}_{T,\nu 2} = \mathbf{p}_T^{\text{miss}}} \left\{ \max\left[m_{T,W}\left(\mathbf{p}_{T,\ell 1}, \tilde{\mathbf{p}}_{T,\nu 1}\right),\ m_{T,W}\left(\mathbf{p}_{T,\ell 2}, \tilde{\mathbf{p}}_{T,\nu 2}\right) \right] \right\}, \tag{3.13}$$

where $\mathbf{p}_{T,\ell 1}$ and $\mathbf{p}_{T,\ell 2}$ are the transverse momenta of the charged leptons and

$$m_{T,W}\left(\mathbf{p}_{T,\ell}, \tilde{\mathbf{p}}_{T,\nu}\right) = \sqrt{m_\ell^2 + 2(E_{T,\ell} E_{T,\nu} - \mathbf{p}_{T,\ell} \tilde{\mathbf{p}}_{T,\nu})} \tag{3.14}$$

is the transverse mass of a single W boson. The m_{T2} variable [73, 74] has acquired quite some fame as a lower bound for the mass of a particle decaying into the WW system. But the value of m_{T2} is not the only result of this procedure. In this minimisation, values are assigned to the neutrino transverse momenta $\tilde{\mathbf{p}}_{T,\nu 1}$ and $\tilde{\mathbf{p}}_{T,\nu 2}$. It can be shown that they follow a Gaussian distribution around the true values and thus provide an estimate of the true neutrino momenta [75]. These estimates better for larger values of m_{T2}, hence a cut on this variable can lead to a more precise reconstruction [76]. As in the case of final states with one neutrino, an on-shell condition (3.11) can then be imposed for each W boson to give estimates for the missing component, again leading to a discrete ambiguity.

This procedure is known as *m_{T2}-assisted on-shell reconstruction (MAOS)* [75, 76] and will be used for the reconstruction of the W boson momenta in the leptonic WW channels throughout this chapter. We will later evaluate how well the results based on this technique agree with the ones that are obtained from the unobservable true W momenta, and whether requiring a large m_{T2} improves the reconstruction accuracy.

Off-shell bosons at the Higgs resonance

The Higgs boson with $m_H = 125$ GeV cannot decay into two on-shell vector bosons. The Breit-Wigner distribution suggests that one of the two final W bosons is approximately on shell, while the other has a lower invariant mass of about 40 GeV. Therefore a different reconstruction protocol is required on the Higgs pole.

In the one-neutrino channels, we use the following strategy:

- An on-shell condition for the leptonically decaying W boson is imposed and the system is reconstructed up to the usual discrete ambiguity.
- If one of the two solutions is compatible with an on-shell Higgs boson, it is used (and the second solution discarded).
- If none of the solutions reconstruct the Higgs boson, the invariant mass of the leptonic W is set to 40 GeV instead and the system is again reconstructed, yielding two additional solutions.
- If this second reconstruction leads to a solution compatible with a Higgs boson, this solution is used.
- If none of these solutions is compatible with an on-shell Higgs boson, the event is rejected.

This strategy leads to a high efficiency for true Higgs-boson decays, while keeping the samples relatively pure.

As before, the leptonic WW states require a more involved treatment:

- Using m_{T2} minimisation, we assign values to the neutrino transverse momenta as discussed in the previous section.
- The W on-shell condition (3.11) is imposed on the vector boson with the larger reconstructed transverse momentum. The other gauge boson is reconstructed by assuming that both W bosons reconstruct an on-shell H:

$$(p_\ell + p_\nu + p_{\text{other V}})^2 = m_H^2. \tag{3.15}$$

  This again introduces a discrete ambiguity.
- If (3.15) has no solutions, the procedure is repeated with swapped gauge bosons, assuming the W with the lower transverse momentum to be on-shell.
- If this also does not give any solutions, the event is rejected.

We will analyse the efficiency of this approach in section 3.4.

3.3.3. Data selection

In this chapter we do not aim to propose a detailed analysis strategy with optimised cuts. We rather try to assess the general prospects of a angular decay measurement for different final states and in different relevant regions of phase space. Therefore we will use three different event selections for the analysis, representing different possible strategies.

All

First, we analyse the full set of events passing the acceptance cuts in table 3.1 and the reconstruction procedure for on-shell V bosons. These samples demonstrate an upper limit on the statistics that can be accumulated in a VV channel while still providing a decent background suppression by means of the WBF cuts.

High energies

As a second approach, we analyse events that pass a high-energy cut in addition to the acceptance cuts in table 3.1. Such a selection is sensitive to an increase of the VV cross sections due to a non-cancellation between Higgs and gauge amplitudes as discussed in section 2.3. In the reconstructable channels (i. e. those with 0 or 1 neutrinos), we require

$$m_{VV} > 400 \text{ GeV}. \tag{3.16}$$

In the channels with two neutrinos, we define a transverse mass for the VV system [77, 78] as

$$m_T^2 = \left(E_{T,\ell\ell} + E_{T,\nu\nu}\right)^2 - \left(\mathbf{p}_{T,\ell\ell} + \mathbf{p}_T^{\text{miss}}\right)^2 \tag{3.17}$$

with

$$E_{T,\ell\ell} = \sqrt{\mathbf{p}_{T,\ell\ell}^2 + m_{\ell\ell}^2}\,, \tag{3.18}$$

$$E_{T,\nu\nu} = \sqrt{\mathbf{p}_T^{\text{miss}\,2} + m_{\ell\ell}^2}\,. \tag{3.19}$$

We require

$$m_T > 250 \text{ GeV} \tag{3.20}$$

instead of the m_{VV} cut. Note that this VV transverse mass is not the same observable as the transverse mass of a single W used in the definition of m_{T2} (3.14).

Higgs resonance

Finally, we analyse W^+W^- and ZZ events compatible with the Higgs pole. In addition to the acceptance cuts in table 3.1 and the Higgs-resonance reconstruction procedure, we require

$$120 \text{ GeV} < m_{VV} < 130 \text{ GeV} \tag{3.21}$$

in the reconstructable channels and

$$50 \text{ GeV} < m_T < 130 \text{ GeV} \tag{3.22}$$

in modes involving two neutrinos.

3.3.4. Polarisation measurement

After the event samples have passed the reconstruction procedure described in section 3.3.2 and the selection cuts given in section 3.3.3, the distributions of the decay angle θ^* are calculated. Then the expected longitudinal and transverse distributions given in (3.1) and (3.2) are fitted to the data.

There is a final complication due to the limited acceptance regions for the V decay products, especially due to the η and p_T cuts. A significant fraction of vector bosons is produced in moderate forward direction, but not strongly boosted. Events where these gauge bosons emit leptons or quarks collinearly are less likely to pass the acceptance cuts than events with gauge bosons decaying orthogonally. Thus the observable $\cos\theta^*$ distributions are suppressed at $|\cos\theta^*| \sim 1$.

This bias can be corrected with different strategies:

1. Additional cuts can be imposed, requiring that the reconstructed gauge bosons hit the detector centrally and highly boosted. This reduces the already low rates further.

2. The impact of the acceptance effect can be reduced by limiting the fit of (3.1) and (3.2) to the region of low and moderate values of $|\cos\theta^*|$, i. e. excluding the problematic forward and backward directions. Of course, this also leads to a small loss of information.

3. By simulating event samples with and without the acceptance cuts, the acceptance effect can be measured, quantified as a function of the decay angle and removed from the data. Such an approach relies on the kinematic distributions of the V bosons and thus to some degree on the physics model, but retains all events.

The third option should be used in a thorough analysis. For simplicity, we choose the second strategy and fit the decay distributions to data only in the region

$$|\cos\theta^*| \leq 0.75. \tag{3.23}$$

We find that this measure reduces the acceptance effects to a manageable level, and retains most of the information in the distributions.

The fit does not only yield the best values for the fractions of longitudinal and transverse gauge bosons, but also uncertainties for these parameters. We set the error bars of the distributions such that they correspond to the expected statistical fluctuations after 300 fb^{-1} of data. In this way the parameter errors from the fit are a first approximation for the uncertainty of the polarisation measurement at the coming years of LHC operation.

3.4. Results

3.4.1. Rates

The first results of interest are the cross sections before and after the reconstruction procedure, which are given in table 3.3. Without further selection cuts, we find rates spanning more than two orders of magnitude, from 0.1 fb for the leptonic ZZ states to 30 fb for semileptonic WW events. Generally, W bosons feature higher production cross sections than Z bosons, and semileptonic decays are more likely than leptonic decays, in agreement with the W and Z branching ratios. The high-energy event selection reduces event rates by a factor of two to three. Both for the full samples and for the high-energy events, the reconstruction procedure does not induce a significant rate loss.

To put these numbers into perspective, consider that the LHC is expected to soon record data equivalent to 40 fb^{-1} per year [79, 80]. After some years of operation,

Channel	σ_0 [fb]	σ_{Reco} [fb]	ϵ_{Reco}
$W^+W^- \to (\ell^+\nu)\,(\ell^-\bar{\nu})$	7.90 ± 0.02	7.82 ± 0.02	0.99
$W^\pm W^\pm \to (\ell^\pm\nu)\,(\ell^\pm\nu)$	0.42 ± 0.01	0.42 ± 0.01	0.99
$WZ \to (\ell^\pm\nu)\,(\ell^+\ell^-)$	0.78 ± 0.01	0.68 ± 0.01	0.87
$ZZ \to (\ell^+\ell^-)\,(\ell^+\ell^-)$	0.09 ± 0.01	0.09 ± 0.01	1.00
$ZZ \to (\ell^+\ell^-)\,(\nu\bar{\nu})$	0.66 ± 0.01	0.66 ± 0.01	1.00
$WW \to (\ell^\pm\nu)\,(jj)$	29.36 ± 0.08	25.80 ± 0.08	0.88
$WZ \to (\ell^\pm\nu)\,(jj)$	5.08 ± 0.01	4.41 ± 0.01	0.87
$WZ \to (jj)\,(\ell^+\ell^-)$	2.05 ± 0.01	2.05 ± 0.01	1.00
$ZZ \to (\ell^+\ell^-)\,(jj)$	1.10 ± 0.01	1.10 ± 0.01	1.00

(a) All events

Channel	σ_0 [fb]	σ_{Reco} [fb]	ϵ_{Reco}
$W^+W^- \to (\ell^+\nu)\,(\ell^-\bar{\nu})$	2.86 ± 0.01	2.79 ± 0.01	0.98
$W^\pm W^\pm \to (\ell^\pm\nu)\,(\ell^\pm\nu)$	0.26 ± 0.01	0.26 ± 0.01	0.99
$WZ \to (\ell^\pm\nu)\,(\ell^+\ell^-)$	0.33 ± 0.01	0.29 ± 0.01	0.89
$ZZ \to (\ell^+\ell^-)\,(\ell^+\ell^-)$	0.03 ± 0.01	0.03 ± 0.01	1.00
$ZZ \to (\ell^+\ell^-)\,(\nu\bar{\nu})$	0.25 ± 0.01	0.25 ± 0.01	1.00
$WW \to (\ell^\pm\nu)\,(jj)$	11.39 ± 0.05	10.09 ± 0.05	0.89
$WZ \to (\ell^\pm\nu)\,(jj)$	2.41 ± 0.01	2.10 ± 0.01	0.87
$WZ \to (jj)\,(\ell^+\ell^-)$	0.96 ± 0.01	0.96 ± 0.01	1.00
$ZZ \to (\ell^+\ell^-)\,(jj)$	0.42 ± 0.01	0.42 ± 0.01	1.00

(b) High-energy selection.

Channel	σ_0 [fb]	σ_{Reco} [fb]	ϵ_{Reco}
$W^+W^- \to (\ell^+\nu)\,(\ell^-\bar{\nu})$	2.35 ± 0.01	0.16 ± 0.01	0.07
$ZZ \to (\ell^+\ell^-)\,(\ell^+\ell^-)$	0.03 ± 0.01	0.03 ± 0.01	1.00
$ZZ \to (\ell^+\ell^-)\,(\nu\bar{\nu})$	0.06 ± 0.01	0.06 ± 0.01	1.00
$WW \to (\ell^\pm\nu)\,(jj)$	3.13 ± 0.02	1.95 ± 0.02	0.62
$ZZ \to (\ell^+\ell^-)\,(jj)$	0.14 ± 0.01	0.14 ± 0.01	1.00

(c) Higgs-resonance selection.

Table 3.3.: Partonic cross-sections before the reconstruction procedure σ_0, after the reconstruction procedure σ_{Reco}, and reconstruction efficiencies ϵ_{Reco}. The given errors are purely statistical.

the leptonic and semileptonic WW channels might yield enough events for a statistical analysis of these events. The WZ states and the ZZ decay to leptons and neutrinos might also be feasible. The leptonic and semileptonic ZZ states are rarer and will only become relevant at a high-luminosity LHC (HL-LHC), which is planned to give an integrated luminosity of up to 3000 fb^{-1} after 10 years of operation [80, 81].

After the Higgs-resonance selection, the ZZ decays are again too rare to allow for a statistical polarisation analysis. The ZZ decay to leptons and neutrinos suffers from the fact that the transverse-mass cut (3.22) is very inefficient when the two neutrinos come from the off-shell Z. The leptonic WW signature gives a larger rate. However, we find that the MAOS reconstruction procedure performs badly in this part of the phase space, where one of the W bosons is off its mass shell: only 7% of the Higgs decays survive the reconstruction and selection procedure, pushing the rate to a useless level. So only the semileptonic WW channel remains, troubled by a reconstruction efficiency of around 60% and potentially large backgrounds.

Therefore, based on the cross sections, the leptonic W^+W^- channel away from the Higgs resonance seems most promising. It remains to be seen how well the reconstruction procedure works in this channel with its two neutrinos. Other leptonic states suffer from low rates, while the semileptonic channels have to fight against overwhelming QCD backgrounds.

3.4.2. Decay angles

Before we turn to the results of the polarisation fits, let us first analyse the effect of the reconstruction procedure on the decay distribution. We give distributions of truth-level and reconstructed decay angles for some of the channels in figure 3.2, the results for all channels are given in appendix B.1. In figure 3.3, the difference between truth-level and reconstructed results is plotted.

We find that longitudinal gauge bosons generally decay more centrally than transverse ones. The distributions are in agreement with the predictions (3.1) and (3.2). Small deviations can be explained as off-shell effects. All distributions are suppressed at $|\cos\theta^*| \sim 1$ compared to the expectations, which is due to the acceptance effects discussed in section 3.3.4.

In the one-neutrino channels, the reconstruction introduces a slight smearing of the decay angles, as can be seen in the left panels of figure 3.3. This effect is less pronounced in the high-energy and Higgs-resonance samples, where the strong boost of the gauge bosons or the additional kinematic condition that the gauge bosons reconstruct the Higgs, respectively, improve the reconstruction. All in all, the reconstruction has a visible, but not critical impact on these distributions.

The reconstruction for two-neutrino states gives much worse results, shown in the right panels of figure 3.3. The involved MAOS procedure yields an estimate for $\cos\theta^*$ which is distributed around the true value, but with a significant variance and a bias towards

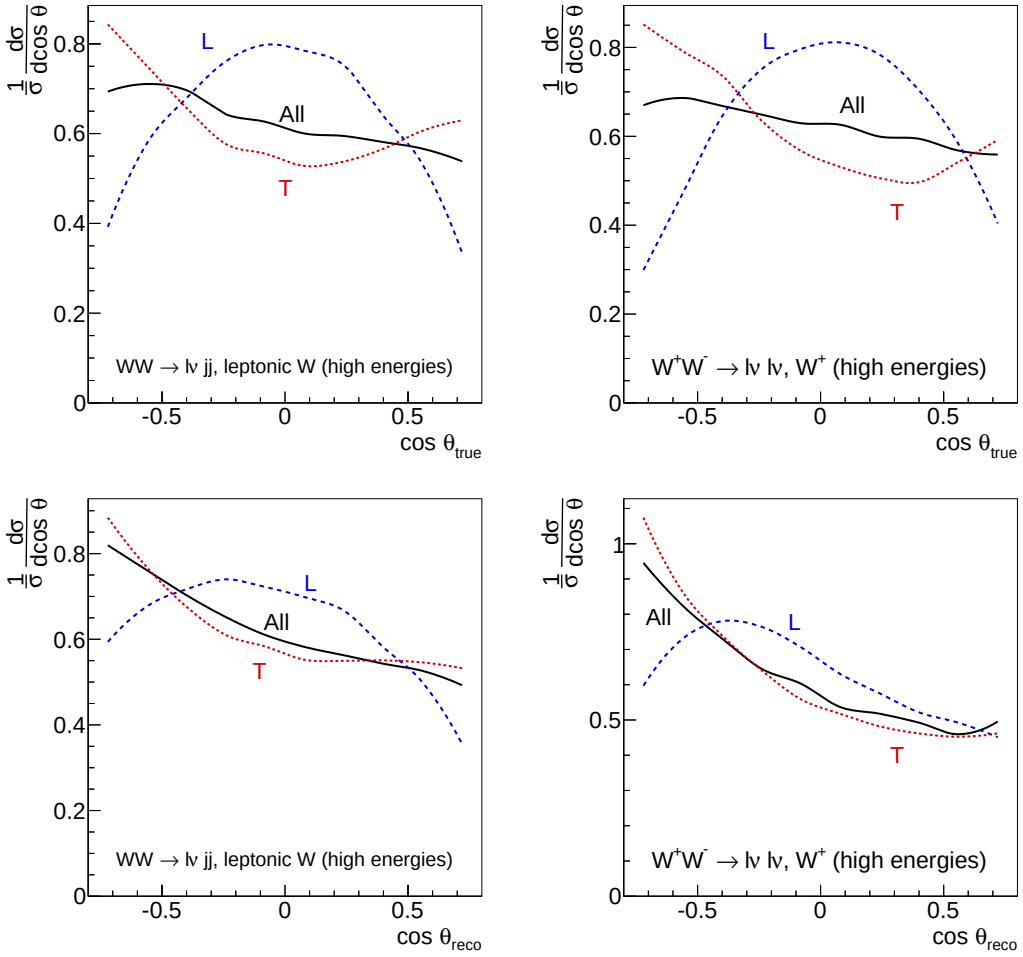

Figure 3.2.: Distribution of decay angles on truth-level (top panels) and after the reconstruction procedure (bottom panels). Only events passing the high-energy cut are shown. Left: leptonic W decay in the semileptonic WW channel. Right: W^+ decay in the leptonic W^+W^- channel after the m_{T2} cut (3.24).

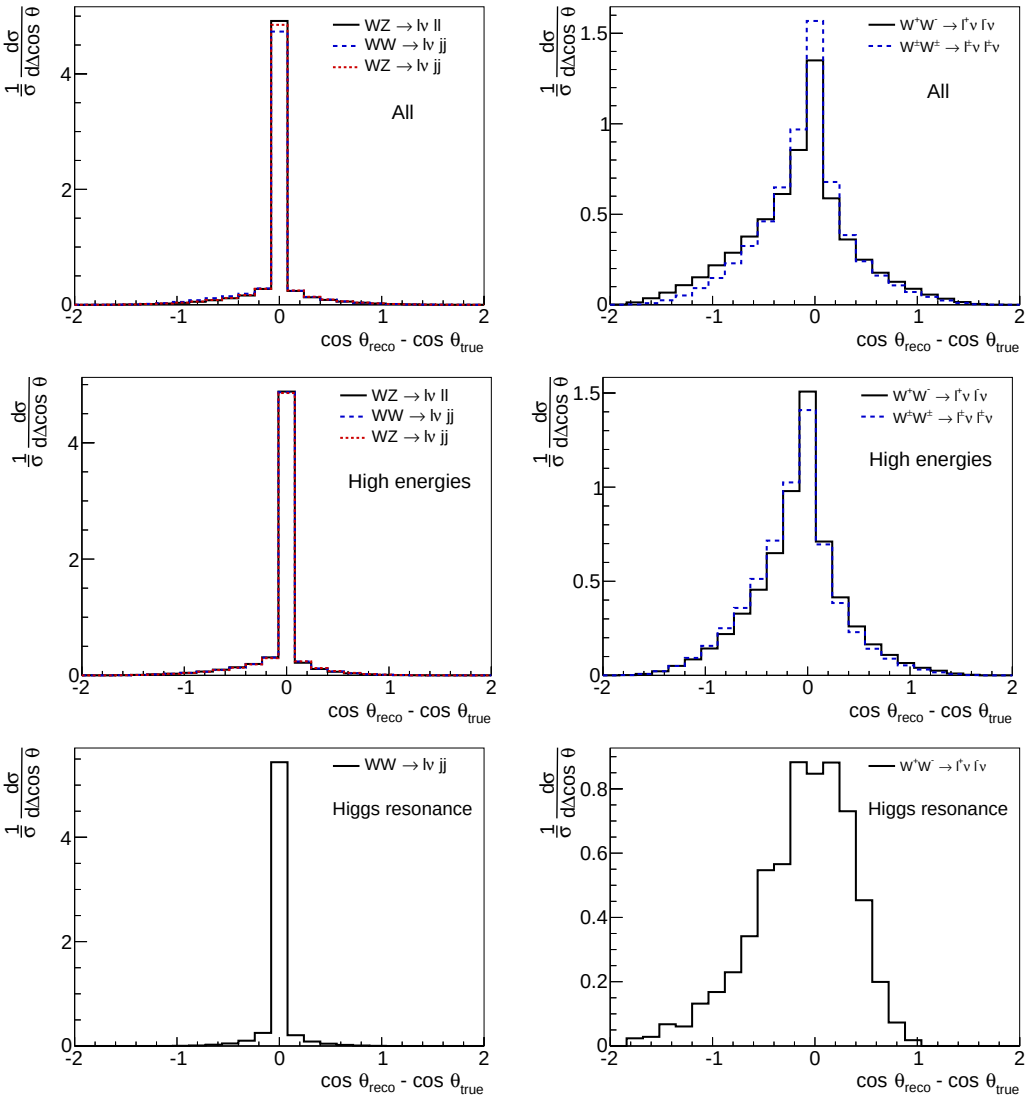

Figure 3.3.: Smearing of the decay angles induced by the reconstruction procedure. The left panels show the channels involving one neutrino, the right panels those with two neutrinos. In the top row, all events are shown, while the middle and bottom rows only show events satisfying high-energy and Higgs-resonance cuts, respectively.

lower values of $\cos\theta^*$. This dramatically changes the shape of the angular distributions. We find that the situation is slightly improved by requiring

$$m_{T2} > 40 \text{ GeV}\,, \tag{3.24}$$

as discussed in section 3.3.2. The difference between longitudinal and transverse gauge bosons is at least partially conserved and there is still some discrimination power between the samples, visible in the bottom right panel of figure 3.2. Still, it is clear that these channels are not suited for a simple fit to the theoretical expectations.

3.4.3. Polarisation fits

Now, a simple fit of the expected angular distributions (3.1) and (3.2) to the samples gives the fraction of longitudinal and transverse bosons. We give our results in tables 3.4 to 3.6. As a sanity check, we perform the same fits on polarised samples, the results of which can be found in appendix B.2. As explained in section 3.3.4, we also give uncertainty estimates based on the expected statistical fluctuations for data equivalent to 300 fb^{-1}. This number should not be mistaken for consistent statistical limit setting, but serves as a first approximation for the precision of such a measurement at the LHC in the coming years.

Let us first take a look at the truth-level polarisation. The fits to the polarised samples generally reproduce the correct polarisations. Small deviations of longitudinal fractions from 0 or 1 are expected due to off-shell effects, as the theoretical angular distributions (3.1) and (3.2) are only strictly true for on-shell gauge bosons. Unexpectedly large deviations appear only in hadronic decays of transverse bosons, which decay more centrally than expected. This might be an artefact of acceptance effects as discussed in section 3.3.4.

In the full, unpolarised samples, the longitudinal fractions vary between 30% and 40% for leptonic decays, as given in table 3.4. In the high-energy event selections, the fraction is around 20% to 30%, while the Higgs-resonance samples are dominated by longitudinal gauge bosons as expected. This is especially true for the reconstructable channels, where the m_{VV} cut gives a much pure sample than the m_T cut in the non-reconstructable channel can provide. Again, the hadronic decays give larger longitudinal fractions, which can be explained by the different acceptance regions for jets compared to leptons.

Fitting the reconstructed distributions instead of the true results induces small deviations in the channels with one neutrino. These effects should be carefully monitored in a more thorough study, but they appear not to pose a serious problem. In the leptonic WW channels with two neutrinos, however, the fitting algorithm fails to converge. The approximate MAOS reconstruction procedure distorts the distributions to such a large degree that our simple fit does not work any longer. Other, more robust observables or a template-based approach to decay distributions are needed to deal with these channels.

VV channel	Gauge boson	Longitudinal fraction	
		True	Reconstructed
$W^+W^- \to (\ell^+\nu)\,(\ell^-\bar{\nu})$	W^+	0.38 ± 0.11	–
	W^-	0.40 ± 0.11	–
$W^\pm W^\pm \to (\ell^\pm\nu)\,(\ell^\pm\nu)$	lower-η W	0.30 ± 0.39	–
	larger-η W	0.32 ± 0.39	–
$WZ \to (\ell^\pm\nu)\,(\ell^+\ell^-)$	W	0.31 ± 0.22	0.30 ± 0.22
	Z	0.33 ± 0.22	0.33 ± 0.22
$ZZ \to (\ell^+\ell^-)\,(\ell^+\ell^-)$	lower-η Z	0.46 ± 0.72	0.46 ± 0.72
	larger-η Z	0.46 ± 0.72	0.46 ± 0.72
$ZZ \to (\ell^+\ell^-)\,(\nu\bar{\nu})$	leptonic Z	0.41 ± 0.22	0.41 ± 0.22
$WW \to (\ell^\pm\nu)\,(jj)$	leptonic W	0.53 ± 0.03	0.30 ± 0.04
	hadronic W	0.68 ± 0.03	0.68 ± 0.03
$WZ \to (\ell^\pm\nu)\,(jj)$	W	0.38 ± 0.09	0.35 ± 0.09
	Z	0.51 ± 0.08	0.51 ± 0.08
$WZ \to (jj)\,(\ell^+\ell^-)$	W	0.57 ± 0.12	0.57 ± 0.12
	Z	0.33 ± 0.13	0.33 ± 0.13
$ZZ \to (\ell^+\ell^-)\,(jj)$	leptonic Z	0.41 ± 0.18	0.41 ± 0.18
	hadronic Z	0.57 ± 0.16	0.57 ± 0.16

Table 3.4.: Relative fraction of longitudinally polarised gauge bosons as determined by a decay fit. The given uncertainties are a first approximation for the expected statistical uncertainty of such a measurement at the LHC after 300 fb^{-1} of data. See the discussion in the text for more details. In the reconstructed leptonic WW states, the fitting procedure does not converge.

VV channel	Gauge boson	Longitudinal fraction	
		True	Reconstructed
$W^+W^- \to (\ell^+\nu)\,(\ell^-\bar{\nu})$	W^+	0.31 ± 0.17	–
	W^-	0.21 ± 0.17	–
$W^\pm W^\pm \to (\ell^\pm\nu)\,(\ell^\pm\nu)$	lower-η W	0.27 ± 0.63	–
	larger-η W	0.29 ± 0.64	–
$WZ \to (\ell^\pm\nu)\,(\ell^+\ell^-)$	W	0.30 ± 0.32	0.24 ± 0.32
	Z	0.29 ± 0.32	0.29 ± 0.32
$ZZ \to (\ell^+\ell^-)\,(\ell^+\ell^-)$	lower-η Z	0.27 ± 0.62	0.27 ± 0.62
	larger-η Z	0.23 ± 0.70	0.23 ± 0.70
$ZZ \to (\ell^+\ell^-)\,(\nu\bar{\nu})$	leptonic Z	0.24 ± 0.34	0.24 ± 0.34
$WW \to (\ell^\pm\nu)\,(jj)$	leptonic W	0.40 ± 0.06	0.31 ± 0.06
	hadronic W	0.52 ± 0.05	0.52 ± 0.05
$WZ \to (\ell^\pm\nu)\,(jj)$	W	0.38 ± 0.12	0.31 ± 0.12
	Z	0.47 ± 0.12	0.47 ± 0.12
$WZ \to (jj)\,(\ell^+\ell^-)$	W	0.49 ± 0.17	0.49 ± 0.17
	Z	0.30 ± 0.19	0.30 ± 0.19
$ZZ \to (\ell^+\ell^-)\,(jj)$	leptonic Z	0.26 ± 0.28	0.26 ± 0.28
	hadronic Z	0.42 ± 0.26	0.42 ± 0.26

Table 3.5.: Relative fraction of longitudinally polarised gauge bosons in the high-energy event selection. The given uncertainties are a first approximation for the expected statistical uncertainty of such a measurement at the LHC after 300 fb^{-1} of data. In the reconstructed leptonic WW states, the fitting procedure does not converge.

VV channel	Gauge boson	Longitudinal fraction	
		True	Reconstructed
$W^+W^- \to (\ell^+\nu)\,(\ell^-\bar{\nu})$	W^+	0.58 ± 0.41	–
	W^-	1.00 ± 0.64	–
$ZZ \to (\ell^+\ell^-)\,(\ell^+\ell^-)$	lower-η Z	0.80 ± 0.88	0.80 ± 0.88
	larger-η Z	0.80 ± 0.88	0.80 ± 0.88
$ZZ \to (\ell^+\ell^-)\,(\nu\bar{\nu})$	leptonic Z	0.90 ± 0.94	0.90 ± 0.94
$WW \to (\ell^\pm\nu)\,(jj)$	leptonic W	1.00 ± 0.07	0.97 ± 0.05
	hadronic W	1.00 ± 0.01	1.00 ± 0.01
$ZZ \to (\ell^+\ell^-)\,(jj)$	leptonic Z	0.88 ± 0.80	0.88 ± 0.80
	hadronic Z	1.00 ± 0.95	1.00 ± 0.95

Table 3.6.: Relative fraction of longitudinally polarised gauge bosons in the Higgs-resonance event selection. The given uncertainties are a first approximation for the expected statistical uncertainty of such a measurement at the LHC after 300 fb^{-1} of data. In the reconstructed leptonic WW state, the fitting procedure does not converge.

Finally, most of the channels are severely limited by statistics, which can be seen by the uncertainties in tables 3.4 to 3.6. The leptonic channels other than W^+W^- simply produce too few events for the coming years of LHC operation. The semileptonic WW and WZ channels fare better, but they will have to survive large QCD backgrounds, which are not included in this first analysis.

3.5. Conclusions

In this chapter we presented a basic strategy to measure the polarisation of the final-state gauge bosons: the reconstruction of their decay angles allows a fit to the distributions expected for longitudinal and transverse modes. This approach is independent of the model and the phase-space region. We find that it works in principle and gives the correct results for polarised samples. As found in [24], this strategy also reduces the large systematic uncertainties of counting experiments. It is thus well suited to analyse gauge boson signatures, at least in channels with sufficiently large rates, low backgrounds and fully reconstructable gauge bosons.

Alas, such a decay mode does not exist. We have analysed all leptonic and semileptonic VV channels, which can be grouped into nine categories with different strengths and weaknesses:

- $W^+W^- \to (\ell^+\nu)\,(\ell^-\bar{\nu})$: This channel features a large rate and low backgrounds.

But the two neutrinos make the reconstruction of the event difficult. We find that a method based on m_{T2} minimisation can provide approximated decay distributions, but they are too different from the true distributions for a straightforward fit. Instead of the reconstruction of decay angles, more robust observables such as the angular correlation of the two leptons should be considered. Unlike decay angles, such distributions are not model-independent.

- $W^{\pm}W^{\pm} \to (\ell^{\pm}\nu)\ (\ell^{\pm}\nu)$: The same-sign version is similar to the opposite-sign signature above, but with lower rate and lower backgrounds. The reconstruction problem due to the two neutrinos persists. Again, a different approach to this channel is preferable.

- $WZ \to (\ell^{\pm}\nu)\ (\ell^{+}\ell^{-})$: This channel also has low backgrounds and is well reconstructable regardless of the neutrino. The rate is too low for such an analysis in the next years, but it may become feasible with larger integrated luminosities.

- $ZZ \to (\ell^{+}\ell^{-})\ (\ell^{+}\ell^{-})$: There are low backgrounds and a perfect reconstructability, but the cross section is way too low to be relevant at any time before the HL-LHC upgrade.

- $ZZ \to (\ell^{+}\ell^{-})\ (\nu\bar{\nu})$: One of the bosons can be reconstructed precisely. The rate is low, but larger than in the fully leptonic ZZ case. This channel may become relevant in a few years.

- $WW \to (\ell^{\pm}\nu)\ (jj)$: The channel originally suggested for such an analysis [24] has a large rate and is well reconstructable despite the neutrino. There are large QCD backgrounds which require further evaluation. This might still be the most promising channel for an analysis in the near future.

- $WZ \to (\ell^{\pm}\nu)\ (jj)$: This channel is similar to the semileptonic WW channel, but has a lower rate. If the large backgrounds can be controlled, this measurement may become feasible at the HL-LHC.

- $WZ \to (jj)\ (\ell^{+}\ell^{-})$: In comparison to the other semileptonic WZ channel, this mode offers a better reconstruction, but gives a lower rate. Its analysis might only become possible with a good background rejection and a lot of statistics.

- $ZZ \to (\ell^{+}\ell^{-})\ (jj)$: This is the semileptonic state with the lowest rate, but similarly large backgrounds. It is unlikely to work in the near future.

There is no golden channel, and any analysis strategy will face challenges due to low rates, QCD backgrounds, or unreconstructable decay modes. Still, some of these channels might become feasible for an LHC analysis.

We have limited ourselves to a very basic analysis on parton level, without any attempt to simulate backgrounds or to optimise cuts. There are other loose ends, including deviations from the theoretical distributions for some hadronic decay angles. A more thorough study should also work on the reconstruction of the leptonic WW states. A next logical step would be the simulation of scenarios of new physics, e. g. in an effective field theory approach, and the measurement of their impact on the polarisation fit results. But such a detailed analysis goes beyond the scope of this thesis, in which we are content with a basic demonstration of the technique. Instead of further developing this approach, we focus on something completely different in the next chapter.

4. Polarisation measurements with tagging jets

In this chapter we develop a novel approach to the Higgs-gauge sector: we propose to measure the polarisation of the initial gauge bosons in gauge boson scattering processes in the kinematics of the tagging jets. We focus on the Higgs pole rather than the high-energy regime. These two features distinguish our analysis from existing studies, which have either investigated the high-energy regime or the decay products of the final gauge bosons, as discussed in section 2.3.4.

Our strategy is motivated by the effective W approximation, which predicts an analytical relation between the transverse momenta of the tagging jets and the polarisation of the initial gauge bosons. We discuss this framework and its implications and analyse its validity. We then use the full process to search for signatures of the gauge boson polarisation in jet observables and evaluate their significance. We compare our results to those from established techniques.

Often the Higgs-gauge sector is parameterised in terms of higher-dimensional operators as discussed in section 2.1.3. However, this effective field theory approach has problems to ask the simple and physical question of gauge boson polarisation. This is why we use a simple model in which the couplings of the Higgs boson to longitudinal and transverse massive gauge bosons are two independent parameters. This definition requires the choice of a reference frame, breaking Lorentz invariance. Later in this chapter we will discuss this worrisome property of the simple model and link it to an approach based on effective field theory.

In section 4.1, we discuss the relation of gauge boson polarisation and tagging jet kinematics in the framework of the effective W approximation. Our simple model is introduced in section 4.2 and we develop our analysis strategy in section 4.3. The results follow in section 4.4. In section 4.5, we link our model to an approach based on higher-dimensional operators and discuss the dependence on reference frames. Our conclusions are given in section 4.6.

The work presented in this chapter has been submitted for publication [28]. There is some overlap in text, tables, and figures between this chapter and the submitted draft.

4.1. The effective W approximation

4.1.1. Introduction

Hadrons are usually considered as a sea of only quarks and gluons. However, under certain conditions the radiation of electroweak gauge bosons off incoming quarks can be factorised out of scattering processes, effectively allowing for the treatment of $W^{\pm}$ and Z bosons as partons. Consider a process $qX \to q'Y$ where the interaction is mediated by a W boson. In the effective W approximation (EWA), this process is factorised into a splitting function describing the radiation of a W off a quark and a hard process initiated by an on-shell W:

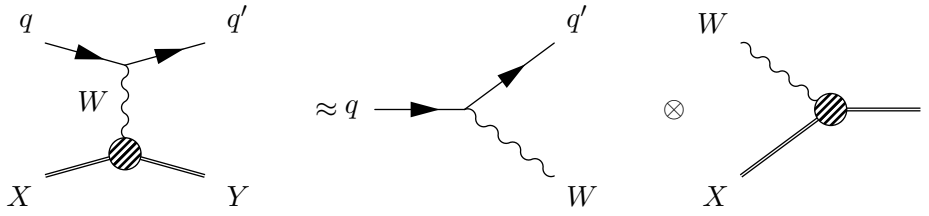

(4.1)

Essentially, this turns the t-channel W of the full process into an on-shell s-channel propagator.

To be more precise, in the effective W approximation the cross-section is given by [27]

$$\frac{\mathrm{d}\sigma_{\mathrm{EWA}}(qX \to q'Y)}{\mathrm{d}x\mathrm{d}p_T} = P_T(x,p_T)\,\mathrm{d}\hat{\sigma}(W_T X \to Y) \;+\; P_L(x,p_T)\,\mathrm{d}\hat{\sigma}(W_L X \to Y)\,. \quad (4.2)$$

Here

$$P_T(x,p_T) = \frac{g^2}{16\pi^2}\,\frac{1+(1-x)^2}{x}\,\frac{p_T^3}{((1-x)m_W^2+p_T^2)^2} \quad (4.3)$$

and

$$P_L(x,p_T) = \frac{g^2}{16\pi^2}\,\frac{1-x}{x}\,\frac{2p_T(1-x)m_W^2}{((1-x)m_W^2+p_T^2)^2} \quad (4.4)$$

are the splitting functions for transverse and longitudinal W bosons carrying a longitudinal momentum fraction x of the quark and a transverse momentum p_T relative to the quark. P_T and P_L are the analogue of p_T-dependent parton density functions. For us, the relevant feature of these functions is the different p_T dependence between longitudinal and transverse gauge bosons. A similar result is obtained for processes mediated by Z bosons.

For hadronic cross-sections, (4.2) has to be convoluted with the parton density function $f_i(x)$ of quark flavour i inside a proton:

$$\frac{\mathrm{d}\sigma_{\mathrm{EWA}}(pX \to q'Y)}{\mathrm{d}p_T} = \sum_i \int_0^1 \mathrm{d}x_q \int_0^1 \mathrm{d}x_W \; f_i(x_q) \Big[P_T(x_W, p_T) \; \mathrm{d}\hat{\sigma}(W_T X \to Y) + P_L(x, p_T) \; \mathrm{d}\hat{\sigma}(W_L X \to Y) \Big] . \quad (4.5)$$

The sum includes all relevant quark flavours i. x_q is the fraction of the proton energy carried by q, while x_W describes the fraction of the longitudinal momentum of q carried by the W boson. The longitudinal momentum of a W boson radiating off a proton with energy E is therefore given by $x_W x_q E$.

It is straightforward to generalise this result to processes of the form $pp \to q_1' q_2' XY$ where again the interaction is mediated by two W bosons radiating off initial-state quarks. This is exactly the topology of vector boson scattering at the LHC. The effective W approximation then reads

$$\frac{\mathrm{d}\sigma_{\mathrm{EWA}}(pp \to q_1' q_2' XY)}{\mathrm{d}p_{T1}\mathrm{d}p_{T1}} = \sum_i \sum_j \sum_m \sum_n \int_0^1 \mathrm{d}x_{q1} \int_0^1 \mathrm{d}x_{q2} \int_0^1 \mathrm{d}x_{W1} \int_0^1 \mathrm{d}x_{W2} \times f_i(x_{q1}) \; f_j(x_{q2}) \; P_m(x_{W1}, p_{T1}) \; P_n(x_{W2}, p_{T2}) \; \mathrm{d}\hat{\sigma}(W_m W_n \to Y), \quad (4.6)$$

where the sums run over all allowed combinations of quark flavours i, j and W polarisation states m, n.

To first order the initial quarks inside the proton have vanishing transverse momenta, so the transverse momenta of the final-state quarks are equal to those of the W bosons. Thus, (4.6) together with (4.3) and (4.4) presents an analytical relation between the transverse momenta of the tagging jets in weak boson fusion processes and the polarisation of the initial gauge bosons. The effective W approximation thus predicts that longitudinal W bosons correspond to lower transverse jet momenta than transverse W bosons.

4.1.2. Validity at the Higgs pole

But is the effective W approximation valid in the regime of our analysis, which is WW scattering at the Higgs resonance? The EWA essentially considers the W as a parton inside the proton. This assumes a hierarchy

$$E_p \sim E_q \gg m_H \gg p_{T,j} \sim m_W \, , \quad (4.7)$$

where m_H is the scale of the hard WW scattering process. In [27], this hierarchy is expressed in terms of two validity conditions:

$$\frac{m_W}{E_q} \ll 1 \quad (4.8)$$

Parameter	Value
Collider setup	pp collisions at $\sqrt{s} = 14$ TeV
m_H	400 GeV, 1000 GeV
Number of events (`MadGraph` samples)	100,000 each
Number of points (MC integration of EWA)	10,000,000 each
Parton density function	CTEQ6L [49]

Table 4.1.: Parameters used for the validation of the effective W approximation.

and

$$\frac{p_{T,j}}{E_q} \ll 1\,. \tag{4.9}$$

We analyse the validity of the effective W approximation by comparing the EWA prediction to a simulation of the full amplitude. For simplicity, we limit ourselves to the subprocess

$$ud \to du\, W^+W^- \to du\, H\,, \tag{4.10}$$

which is the dominant contribution to the weak boson fusion production of Higgs bosons, as discussed in 2.3.3.

This process is fully simulated in `MadGraph 5` [46] with different Higgs masses. We also generate samples where the polarisations of the initial W bosons are limited to longitudinal or transverse. The polarisation states are defined in the Higgs rest frame. Table 4.1 summarises the parameters used for the event generation.

The EWA prediction for weak-boson-fusion topologies is given in (4.6). A straightforward calculation gives the cross section for the hard process $W^+W^- \to H$ as

$$\mathrm{d}\hat{\sigma}(W_T^+W_T^- \to H) = \frac{\pi g^2 m_W^2}{2m_H\sqrt{m_H^2 - 4m_W^2}}\,\delta(x_{W1}x_{W2}x_{q1}x_{q2}s - m_H^2), \tag{4.11}$$

$$\mathrm{d}\hat{\sigma}(W_L^+W_L^- \to H) = \frac{\pi g^2 (m_H^2 - 2m_W^2)^2}{4m_W^2 m_H\sqrt{m_H^2 - 4m_W^2}}\,\delta(x_{W1}x_{W2}x_{q1}x_{q2}s - m_H^2), \tag{4.12}$$

$$\mathrm{d}\hat{\sigma}(W_T^+W_L^- \to H) = 0, \tag{4.13}$$

$$\mathrm{d}\hat{\sigma}(W_L^+W_T^- \to H) = 0. \tag{4.14}$$

This assumes both W bosons and the Higgs boson to be on-shell. The calculation is given in appendix A.3. For a Higgs boson with the observed mass of 125 GeV, this gives a vanishing cross section, reflecting the assumption of on-shell W bosons. Hence only the production of heavy Higgs bosons with $m_H > 2m_W$ is analysed.

m_H [GeV]	Initial W	Cross section [fb]		
		Full process	EWA (bare)	EWA (cuts)
1000	All	45.0		
	Longitudinal	45.1	48.4	47.0
	Transverse	0.084	0.200	0.108
400	All	267		
	Longitudinal	276	272	225
	Transverse	5.14	37.8	11.1
180	All	747		
	Longitudinal	931	191	103
	Transverse	105	1343	212

Table 4.2.: Cross sections for Higgs production in weak boson fusion for the full process simulated with `MadGraph` and according to the effective W approximation, both before and after applying the validity cuts (4.15) to (4.16). The statistical uncertainties on these results are negligible.

We calculate the EWA prediction for this process, given in (4.6) and (4.11) to (4.14), by Monte-Carlo integration. All parameters are chosen to be consistent with the full simulation with `MadGraph`. The parton density functions are included with the `LHAPDF` library [82]. A number of sanity checks verify that the Monte-Carlo integration performs as expected.

The effective W approximation is assumed to be valid only in the regime where (4.8) and (4.9) hold. In addition to the numerical calculation of the full integrals in (4.6), we therefore calculate the EWA cross section with the additional phase-space cuts

$$\frac{m_W}{E_{qi}} \leq \frac{1}{4} \tag{4.15}$$

and

$$\frac{p_{Ti}}{E_{qi}} \leq \frac{1}{4}\,. \tag{4.16}$$

These conditions cut off the integrals where the EWA fails to be valid.

We give the cross sections for the full simulation and the EWA prediction in table 4.2. As expected, Higgs boson production is dominated by longitudinal modes, especially for heavy Higgs bosons. The rates for longitudinal W bosons only are larger than the result for the full process, which is evidence for destructive interference between transverse and longitudinal contributions. For $m_H = 1000$ GeV, the effective W approximation

agrees with these rates within $\mathcal{O}(10\%)$, at least after the application of the EWA validity cuts (4.15) and (4.16). For smaller Higgs boson masses, the agreement becomes gradually worse, and at $m_H = 180$ GeV the results differ by as much as an order of magnitude.

The distributions of the transverse jet momenta in the full process and in the effective W approximation are compared in figure 4.1. Again, we find good agreement for a heavy Higgs boson of $m_H = 1000$ GeV, especially in the longitudinal modes. But even in this high-mass regime, the transverse modes show a different fall-off behaviour at large p_T. With decreasing Higgs mass, the deviations become more prominent. Close to the threshold $m_H = 2m_W$, the EWA loses its validity entirely.

So longitudinal W bosons and heavy Higgs bosons give a better agreement between the effective W approximation and the full process than light Higgs bosons or transverse vector bosons. To demonstrate the reason for this, we show the distribution of the critical ratios $p_{T,j}/E_q$ and m_W/E_q in figure 4.2. We find that for $m_H = 1000$ GeV and especially for longitudinal W modes, the conditions (4.15) and (4.16) are easily satisfied. There is a hierarchy between the energy scales of the proton, the hard process and the weak scale, as required by the effective W approximation. For lower Higgs masses as well as for transverse W bosons (corresponding to less collinearly emitted gauge bosons), this hierarchy becomes weaker, and the validity conditions begin to fail.

All in all, we find that the effective W approximation works well at a hypothetical heavy resonance, where a clean hierarchy between the proton energy, the energy scale of the hard process and the weak scale exists. In particular, at such a heavy resonance the p_T dependence of longitudinal and transverse vector bosons is well described by (4.3) and (4.4). At the observed Higgs mass of $m_H = 125$ GeV, however, the EWA loses its validity, and its quantitative predictions are not useful for our analysis. Still, it serves as a motivation to analyse the relation between the polarisation of gauge bosons and the transverse momenta of the tagging jets.

4.2. A simple model

Since the effective W approximation gives a poor description at the Higgs resonance, we now leave it behind and analyse the full process. Motivated by the equivalence theorem as discussed in section 2.2.3, we aim to measure the couplings of longitudinal and transverse gauge bosons to the Higgs separately. This separation is unproblematic for final states, which depending on the phase-space region are often nearly on-shell. It is also well defined in the limit of high energies, where the longitudinal modes are just the Goldstone bosons. For initial gauge bosons at finite energies, the separation is less clean. As discussed in section 2.3.2, the initial vector bosons are t-channel propagators and therefore far off-shell. The definition of their polarisation requires the choice of a reference frame and requires us to break Lorentz invariance. However, this technical

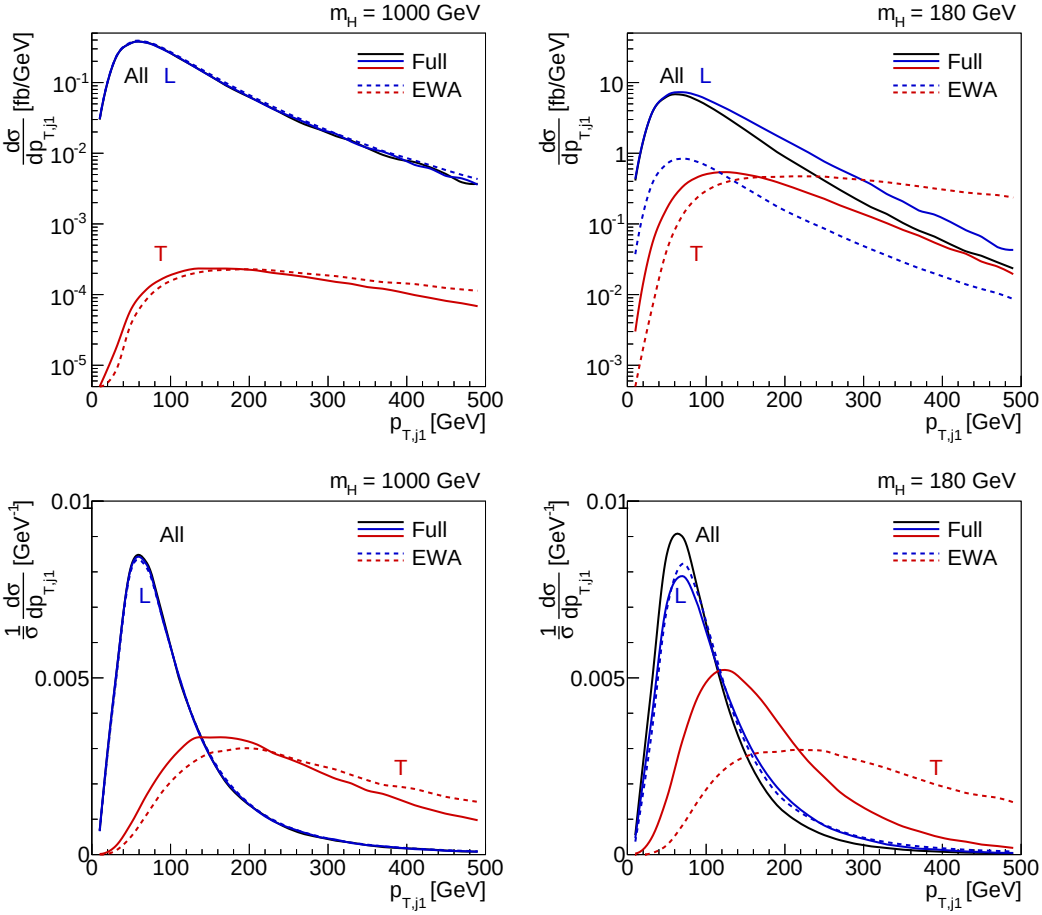

Figure 4.1.: $p_{T,j1}$ distributions for the full process given in (4.10), and predictions based on the effective W approximation after the validity cuts (4.15) and (4.16). The left panels assume a heavy Higgs with $m_H = 1$ TeV, the right ones $m_H = 180$ GeV. The lower panels show the normalised distributions.

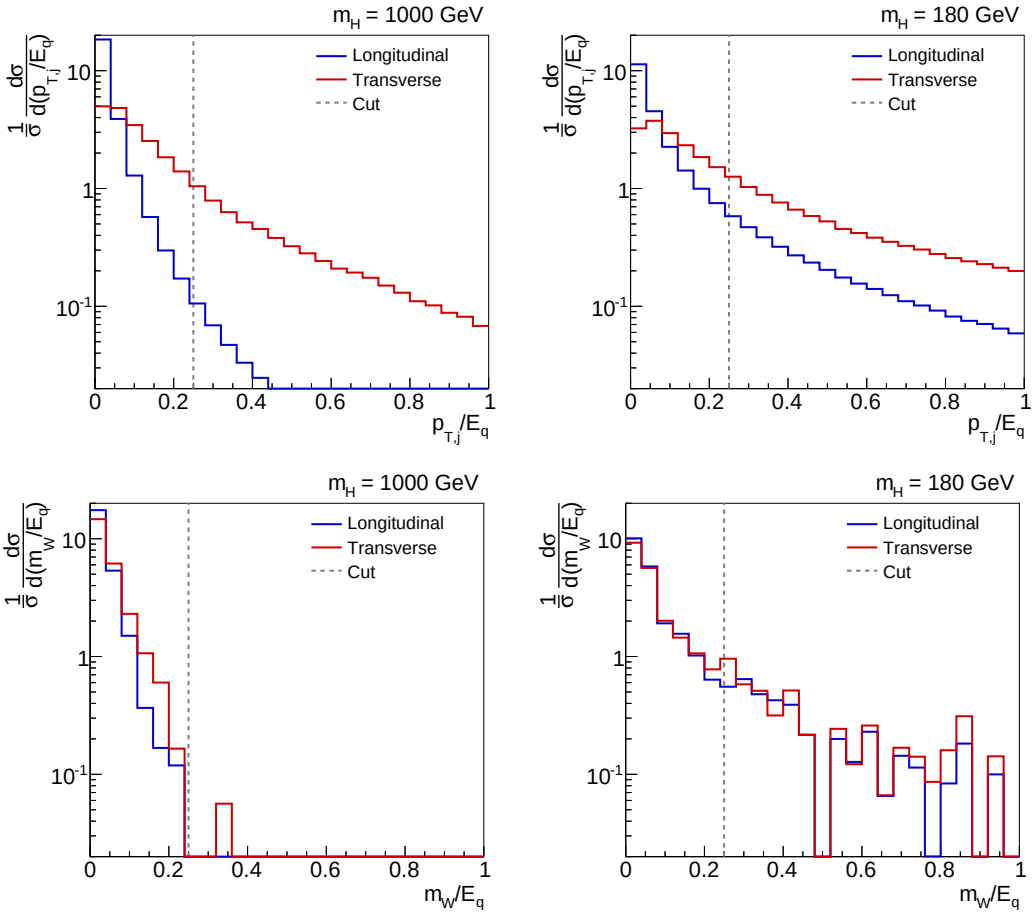

Figure 4.2.: Distribution of p_T/E_q and m_W/E_q for transverse (red) and longitudinal (blue) W bosons in the Monte-Carlo integration of the EWA prediction. The EWA assumes both quantities to be much smaller than 1.

complication does not make the question of how longitudinal and transverse vector bosons couple to the Higgs any less relevant.

We use the definition of polarisation states discussed in section 2.2.2. This allows us to split the Higgs-gauge interaction term into its longitudinal and transverse components. We choose to apply this definition in the W^+W^- rest frame, which for the dominant s-channel Higgs amplitude is the Higgs rest frame. There are two reasons for this: first, this choice of reference frame is best suited for an interpretation in terms of effective field theory, as we will discuss in 4.5.2. Second, this definition disposes of mixed contributions $H\,V_LV_T$ and the Standard Model Higgs-gauge vertex becomes

$$\mathcal{L}_{\text{SM}} \supset g_{\text{SM}}\, H\, VV = g_{\text{SM}}\, (H\, V_LV_L + H\, V_TV_T) \tag{4.17}$$

with $V = W, Z$. In section 4.5.1, other choices of the reference frame will be discussed.

We define a simple model by introducing scaling factors a_L and a_T for the coupling of the Higgs boson to longitudinal and transverse gauge bosons:

$$\mathcal{L} \supset a_L\, g_{\text{SM}}\, H\, V_LV_L + a_T\, g_{\text{SM}}\, H\, V_TV_T\,. \tag{4.18}$$

The parameters a_L and a_T are real numbers, and we do not enforce their sign or a sum rule protecting the total Higgs production and decay rates. We will use this model as a test scenario for our analysis strategy.

As mentioned before, this model is neither gauge invariant nor Lorentz invariant. Clearly it does not pose a consistent quantum field theory. However, independent longitudinal and transverse Higgs-gauge couplings can be induced by perfectly valid models of new physics. In section 4.5.2 we will demonstrate this by linking the simple model to an approach based on effective field theory, which respects Lorentz and gauge symmetry intrinsically. The couplings a_L and a_T then become momentum-dependent.

4.3. Analysis strategy

4.3.1. Choosing a laboratory

As debated in section 2.3.4, there are essentially two choices to make for an analysis of the Higgs-gauge sector, namely the phase-space region and the observables. Regarding the first question, we choose to probe the longitudinal and transverse Higgs-gauge couplings in Higgs production in weak boson fusion. As a decay mode we analyse the leptonic W^-W^+ state. In other words, we are interested in W^+W^- scattering of the form

$$pp \to W^+W^-\, jj \to (\ell^+\bar{\nu})\, (\ell^-\nu)\, jj \tag{4.19}$$

with scattering energies close to the Higgs resonance. This channel is appealing for different reasons. Since the observed resonance resembles the Standard Model Higgs

boson, we know that a large fraction of the events actually come from the s-channel Higgs diagram. Higgs production in weak boson fusion probes the couplings of the initial gauge bosons to the Higgs, while the decay mode is sensitive to the couplings of the final bosons. The cross section of the process is reasonably large. Finally, its two forward jets and its lack of additional hadronic activity mean that QCD backgrounds can be suppressed quite well, as discussed in section 2.3.3.

A key feature of our approach is that we probe the Higgs-gauge sector at the Higgs resonance rather than in the high-energy regime. Looking for longitudinal scattering in the region of a large invariant m_{WW} has a long history, as discussed in section 2.3.4. But these analyses suffer from low rates and large scale uncertainties. In addition, the Higgs discovery takes away some of the motivation for this kind of challenging measurement. It is safe to assume that the increase of the cross section at large energies with its eventual violation of perturbative unitarity is at least partially cured by the newly discovered boson. This postpones any critical behaviour to higher energies and thus lower rates. Since most of the $WW\,jj$ cross section comes from the Higgs pole, it seems natural to analyse the Higgs-gauge sector at this resonance rather than in the region of high energies.

The second question is the choice of observables. Of course, the leptons are sensitive to the final HVV coupling. As a matter of fact, the LHC Higgs analyses already use correlations between the two leptons based on the scalar nature of the Higgs [1, 2]. The most straightforward observables are decay angles, which were extensively examined in chapter 3. However, we found that the two neutrinos of the channel (4.19) make the reconstruction of these angles very difficult, especially close to the Higgs resonance where at least one of the final W bosons is forced off shell. Alternative observables include the lepton transverse momenta, the dilepton invariant mass, angular correlations between the two leptons, or the missing transverse momentum. We will later briefly discuss an analysis based on such quantities.

Instead of the leptons, we focus on the tagging jets, which provide a handle to the initial HVV vertex [58–64]. This is motivated by the effective W approximation, which predicts an analytical relationship between the polarisation of the initial gauge bosons and the transverse jet momenta, as discussed in the previous section. We will later see that the information encoded in the tagging jets is similar to the information in the lepton kinematics. Our approach has the advantage of being independent of the decay channel, allowing for an efficient combination of individual Higgs decay modes.

4.3.2. Event generation and selection

We implement the simple model defined in section 4.2 in `MadGraph 5` and generate event samples. The full amplitude for the process (4.19) at the leading electroweak order $\mathcal{O}(\alpha^4)$ is taken into account. This includes the signal s-channel Higgs amplitude as well as continuum electroweak W^+W^- production as a first background. As an

Parameter	Value
Collider setup	pp collisions at $\sqrt{s} = 13$ TeV
m_H	125 GeV
Number of events	$> 100,000$ each
Parton density function	CTEQ6L [49]

Table 4.3.: Parameters for the event generation.

Leptonic cuts	Jet cuts
$\lvert\eta_\ell\rvert < 2.5$	$\lvert\eta_j\rvert < 5.0$
$p_{T,\ell} > 20$, 10 GeV	$p_{T,j} > 25$ GeV
	$m_{jj} > 500$ GeV
	$\eta_{j1} \cdot \eta_{j2} < 0$
$p_T^{\text{miss}} > 20$ GeV	$\Delta\eta_{jj} > 4.2$

Table 4.4.: Acceptance and weak boson fusion cuts required during event generation.

additional background, Higgs production in gluon fusion (GF) with the same final state at order $\mathcal{O}\left(\alpha_{ggH}\,\alpha_s^2\,\alpha\right)$ is included. Finally, we simulate continuum W^+W^- production at order $\mathcal{O}\left(\alpha_s^2\,\alpha^2\right)$. The most dangerous background missing in our simulation is $t\bar{t}$ production. As discussed in section 2.3.3, it can be kept at bay with techniques such as a central jet veto [77, 78], and should be studied in a more thorough analysis at hadron level. There is also background from $\tau^+\tau^-$ and ZZ production with additional jets, but these contributions do not pose a serious threat [77, 78].

These processes are simulated for pp collisions at an energy of $\sqrt{s} = 13$ TeV. Since it is established that weak boson fusion signatures can be extracted experimentally, we limit our study to the parton level. We assume a Higgs mass of $m_H = 125$ GeV and a corresponding decay width of $\Gamma_H = 4.4$ MeV, calculated with `HDecay` [83]. For the Higgs-gauge coupling parameters (a_L, a_T), a total of 529 parameter points are simulated, 441 of which are evenly distributed in the range $a_{L/T} \in [-2, 2]$, while the remaining 88 are chosen close to the Standard Model value $a_L = a_T = 1$ to increase the sensitivity in this region of interest. A map of the simulated parameter points is shown in figure B.10 in appendix B.3. Between these points cross sections, kinematic quantities and p-values are interpolated by Delauny triangulation [84]. Other settings used in the event generation are given in table 4.3.

We simulate typical detector acceptance regions [67–69] and suppress the backgrounds by imposing the standard weak boson fusion cuts given in table 4.4. We require two tagging jets with an invariant mass of $m_{jj} > 500$ GeV between them and a separation of pseudorapidity of at least $\Delta\eta_{jj} > 4.2$. In order to select events from the Higgs pole,

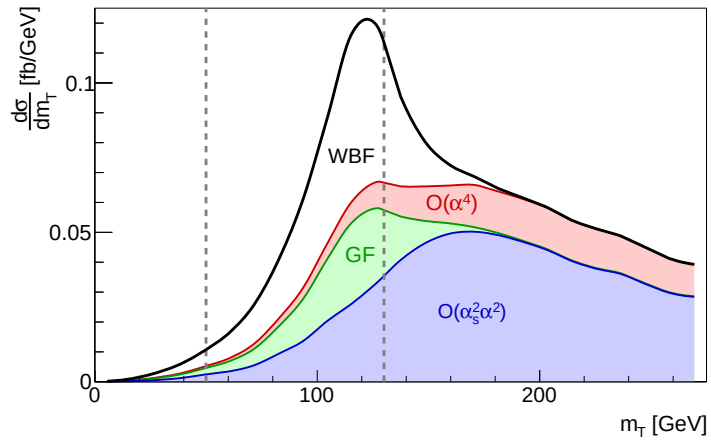

Figure 4.3.: Transverse mass distribution for the signal (white) and background (red, green, and blue) contributions in the Standard Model. The dashed lines indicate the selection cuts.

we again use the transverse mass of the WW system,

$$m_T^2 = \left(E_{T,\ell\ell} + E_{T,\nu\nu}\right)^2 - \left(\mathbf{p}_{T,\ell\ell} + \mathbf{p}_T^{\text{miss}}\right)^2 \tag{4.20}$$

with

$$E_{T,\ell\ell} = \sqrt{\mathbf{p}_{T,\ell\ell}^2 + m_{\ell\ell}^2}\,, \tag{4.21}$$

$$E_{T,\nu\nu} = \sqrt{\mathbf{p}_T^{\text{miss}\,2} + m_{\ell\ell}^2}\,, \tag{4.22}$$

and require the events to satisfy

$$50 \text{ GeV} < m_T < 130 \text{ GeV}\,. \tag{4.23}$$

4.4. Results

4.4.1. Signal and background contributions

Before analysing the effect of the longitudinal and transverse Higgs-gauge couplings on observables, we give the signal and background distributions to the transverse mass distribution in figure 4.3. The selection cut (4.23) retains 74% of the true Higgs-resonance events and gives a signal-to-background ratio of approximately unity (c.f. table 4.5).

Contribution	Cross section [fb]	
	Before m_T cut	After m_T cut
WBF $H \to W^+W^-$	3.15 ± 0.01	2.34 ± 0.01
Continuum $\mathcal{O}(\alpha^4)$	4.54 ± 0.01	0.31 ± 0.01
GF $H \to W^+W^-$	1.62 ± 0.01	1.13 ± 0.01
Continuum $\mathcal{O}(\alpha_s^2\alpha^2)$	11.01 ± 0.01	1.17 ± 0.01
$S/(S+B)$	0.15	0.47

Table 4.5.: Cross sections in fb for the different contributions before and after the m_T cut (4.23). The given uncertainties are purely statistical.

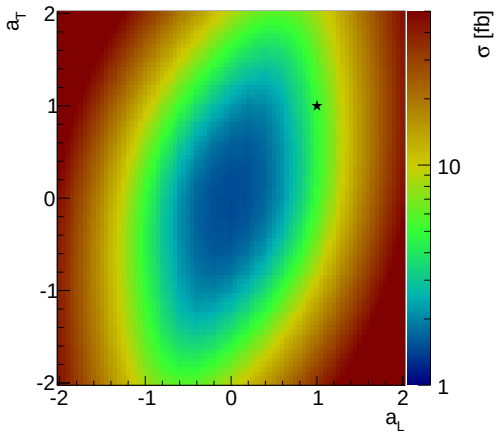

Figure 4.4.: Cross section at the Higgs resonance as a function of the Higgs couplings to longitudinal and transverse vector bosons. The star marks the Standard Model.

4.4.2. Resonance cross section

In the following sections we answer the question how a modification of the longitudinal and transverse Higgs-gauge couplings translates into observables. First, we give the cross section on the Higgs resonance as a function of the parameter space in figure 4.4. Close to the Standard Model, the rate is nearly insensitive to the transverse Higgs-gauge coupling. This agrees with the expectation that the Standard Model Higgs boson couples predominantly to longitudinal W bosons.

Further away from the Standard Model, we find that the curve with a constant rate is approximately an ellipse in the (a_L, a_T) plane. This reflects the fact that the Higgs production rate is quadratic in $a_{L/T}$:

$$\sigma_{\text{production}} = \int \mathrm{d}\Omega \, | \, [a_L \mathcal{M}_L + a_T \mathcal{M}_T + \mathcal{M}_{ew}] \, |^2 + \sigma_{QCD} \, . \tag{4.24}$$

Here Ω denotes the phase space, including the parton density functions and all other prefactors, $\mathcal{M}_{L(T)}$ are the amplitudes corresponding to initial longitudinal (transverse) gauge bosons, $\mathcal{M}_{ew}$ is the amplitude from electroweak non-Higgs diagrams, and σ_{QCD} is the cross-section from all QCD-involving background processes that do not interfere with the electroweak signal due to the different colour structure. (4.24) is the equation of an ellipse in (a_L, a_T) space. However, also the $H \to W^+W^-$ decay is governed by the parameters $a_{L/T}$, which introduces higher powers of $a_{L/T}$ into the expression for the cross section and leads to deviations from a purely elliptical shape. This parameter space region of constant cross section is where we need additional kinematic information to constrain the individual couplings $a_{L,T}$.

4.4.3. Tagging jet kinematics

Transverse momentum

In section 4.1 we found that the effective W approximation predicts an analytical relation between the polarisation of the initial gauge boson pair and the transverse momenta of the tagging jets. It turned out that the EWA is not a good approximation for light Higgs resonances. Nevertheless, it motivates an analysis of the transverse jet momenta. In the left panel of figure 4.5 we give these distributions for the leading jet, based on the Standard Model and on four additional parameter points which give the same cross section. In the right panel of the same figure the average transverse momentum of the leading jet is shown as a function of the parameters a_L and a_T. An analysis of the subleading jet shows a qualitatively similar, but less pronounced behaviour.

We find that deviations from the Standard Model typically shift the distribution to larger transverse jet momenta. The Standard Model does not mark the parameter-space point with the minimal jet p_T scale, but it is not far away from this minimum. All in all, the effect of a modified Higgs-gauge sector on these distributions is clearly visible, but

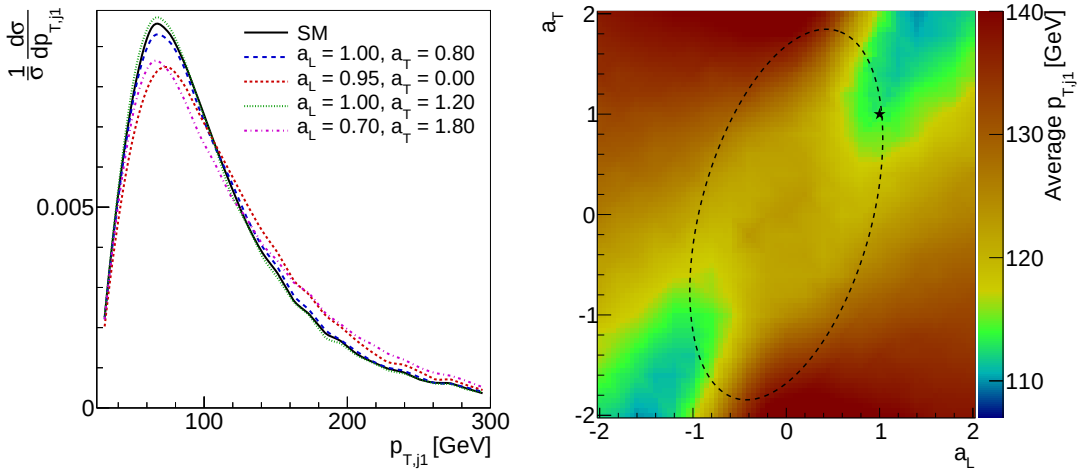

Figure 4.5.: Left: distribution of the transverse momentum of the leading jet in the Standard Model and in four scenarios with modified Higgs-gauge coupling structures, all giving the same cross section. Right: average transverse momentum of the leading jet as a function of the parameter space of our simple model. The Standard Model is marked with a star, and the ellipse denotes the region giving a constant cross section.

it is not huge. These signatures will be further reduced by hadronisation, jet clustering, and detector resolution.

The individual transverse momenta of the leading and subleading jet are not the only potentially relevant parameterisation. We also evaluate the average transverse momentum,

$$\bar{p}_T = \frac{1}{2}\left(p_{T,j1} + p_{T,j2}\right) , \tag{4.25}$$

and the asymmetry in the transverse momenta between the two jets,

$$A_{pT} = \frac{\left(p_{T,j1} - p_{T,j2}\right)}{\left(p_{T,j1} + p_{T,j2}\right)} . \tag{4.26}$$

This asymmetry is particularly robust under systematic uncertainties such as the jet energy scale.

The average transverse momentum behaves similar to the transverse momentum of the leading jet: modifications of the Standard Model Higgs-gauge sector typically shift it to larger values. Regarding the asymmetry A_{pT} we find that a deviation from the Standard Model tends to marginally shift the distribution to lower values, as can be seen in the right panel of figure 4.6. So moving away from the Standard Model in parameter space

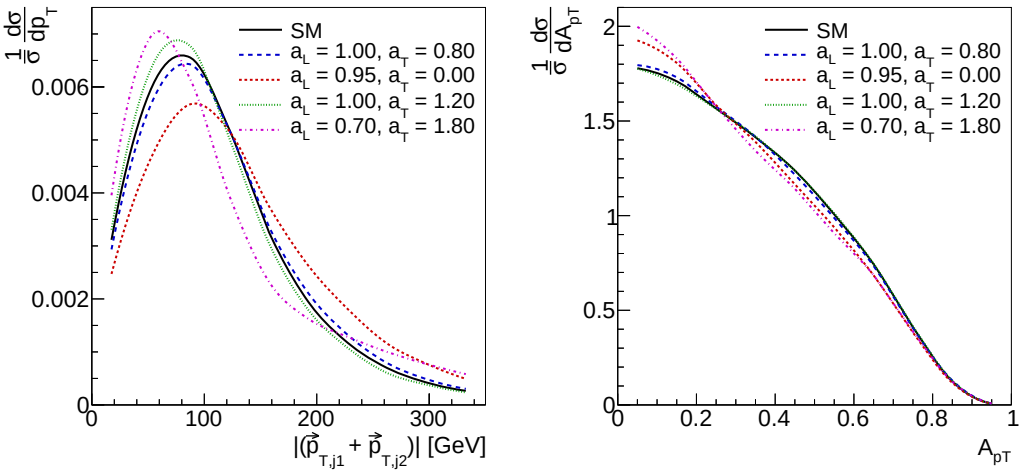

Figure 4.6.: Alternative parameterisations of the transverse jet momenta. As before, the distributions in the Standard Model and in four scenarios with modified Higgs-gauge coupling structures are shown. Left: vectorial sum of the transverse jet momenta. Right: p_T asymmetry between the two jets as defined in (4.26).

lets both jets gain transverse momentum, but the subleading jet increases its transverse momentum by a larger factor than the leading jet.

As a final parameterisation we consider the vectorial sum and difference of the two transverse jet momenta. Unlike the observables discussed so far, these quantities include the angular correlation between the two jets. We find that the vectorial sum is shifted to larger (lower) values for $a_L > a_T$ ($a_L < a_T$), as can be seen in the left panel of figure 4.6. The vectorial difference shows the opposite behaviour, but the differences are less pronounced.

Azimuthal angle

As a next observable we consider the azimuthal angle between the two tagging jets, $\Delta\phi_{jj}$, which has a long tradition as an observable sensitive to the HVV vertex in weak boson fusion signatures [58–64]. In particular, it has been proposed as a measure of the Higgs spin and CP properties. Its distribution for the same parameter points as before is given in the left panel of figure 4.7. Indeed, deviations from the Standard Model leave a very clear signature in this observable. With $a_L > a_T$, jets are more collinear in the transverse plane. Conversely, a small increase of a_T with respect to the longitudinal coupling favours back-to-back geometries.

This effect can be quantified in a way that minimises systematic uncertainties by

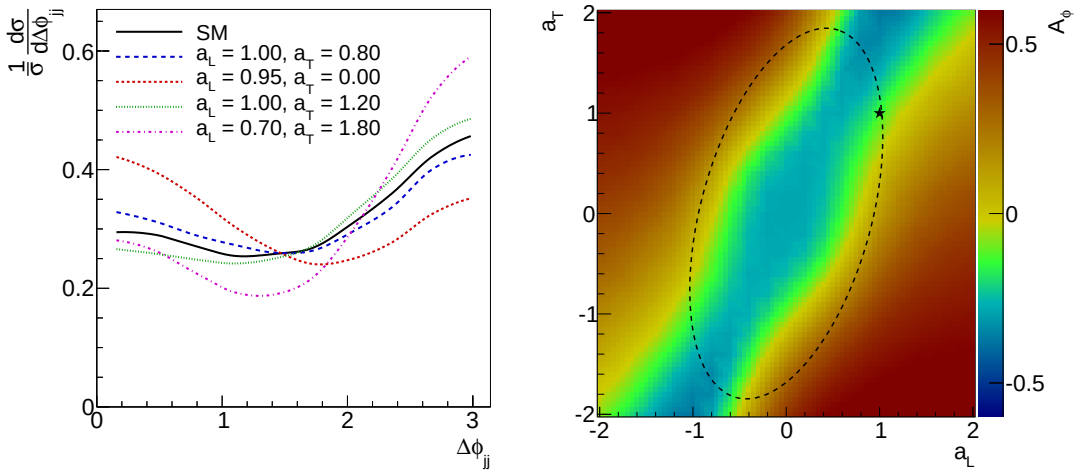

Figure 4.7.: Left: distribution of the azimuthal angle between the two jets in the Standard Model and in four scenarios with modified Higgs-gauge coupling structures, all giving the same cross section. Right: asymmetry A_ϕ as defined in (4.27) as a function of the parameter space of our simple model. Again, the Standard Model is marked with a star, and the ellipse denotes the region giving a constant cross section.

defining the asymmetry [58]

$$A_\phi = \frac{\sigma(\Delta\phi_{jj} < \frac{\pi}{2}) - \sigma(\Delta\phi_{jj} > \frac{\pi}{2})}{\sigma(\Delta\phi_{jj} < \frac{\pi}{2}) + \sigma(\Delta\phi_{jj} > \frac{\pi}{2})} \,. \tag{4.27}$$

The distribution of this asymmetry as a function of the parameter space can be seen in the right panel of figure 4.7. Its behaviour agrees with the results from the full $\Delta\phi_{jj}$ distribution, and any modification of the Higgs-gauge couplings is clearly visible in the A_ϕ value.

Comparing the right panels of figures 4.5 and 4.7 to figure 4.4, one can see that the information encoded in the $p_{T,j}$ and $\Delta\phi_{jj}$ distributions is orthogonal to that of the cross section. Therefore we expect their combination to improve the discrimination power in the parameter space.

Other observables

So far our analysis was restricted to the jet kinematics in the transverse plane, which indeed turned out to be sensitive to the structure of the Higgs-gauge sector. Now let us focus on quantities that are mostly sensitive to the longitudinal jet momenta. We analyse the jet energies, the dijet invariant mass m_{jj}, and the separation pseudorapidity between

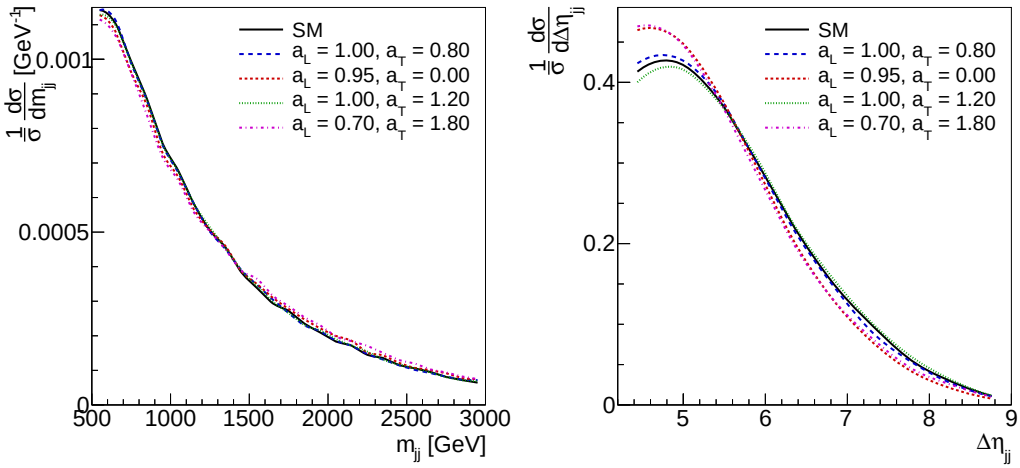

Figure 4.8.: Left: distribution of the dijet mass in the Standard Model and in scenarios with a modified Higgs-gauge coupling structure. Right: distribution of the rapidity gap between the two jets in the same scenarios.

the two jets $\Delta\eta_{jj}$. In figure 4.8 the distributions of the latter two observables are given for the usual parameter points. We find that they are less sensitive to the Higgs-gauge couplings than the transverse quantities discussed before. As a matter of fact, what little discrimination is visible in these distributions can be traced to the transverse jet momenta, which contribute to these quantities as well. The longitudinal components of the jet momenta are almost entirely insensitive to the Higgs-gauge couplings.

This observation is no surprise. The longitudinal momenta of the final-state quarks in weak boson fusion processes are dictated by the incoming quarks, which in turn have an energy scale given by the proton energies and the parton density functions. At the LHC this scale is much larger than that describing the hard WW scattering process. Therefore the transverse components of the jet momenta are much more sensitive to the hard process than the longitudinal parts. As a demonstration we give the distribution of the Mandelstam variable t of the hard $WW \to WW$ process for different $p_{T,j1}$ and $p_{L,j1}$ slices in figure 4.9. It is obvious that the transverse momentum is strongly correlated with this energy scale of the hard process, while there is very little sensitivity to t in the longitudinal jet momentum.

Including these variables does not improve the discrimination power in parameter space, which is why we limit this analysis to the transverse jet momenta and azimuthal angles discussed above.

As an aside, we also search for correlations between the tagging jet properties and the polarisation of the final gauge bosons, which can for instance be measured with decay

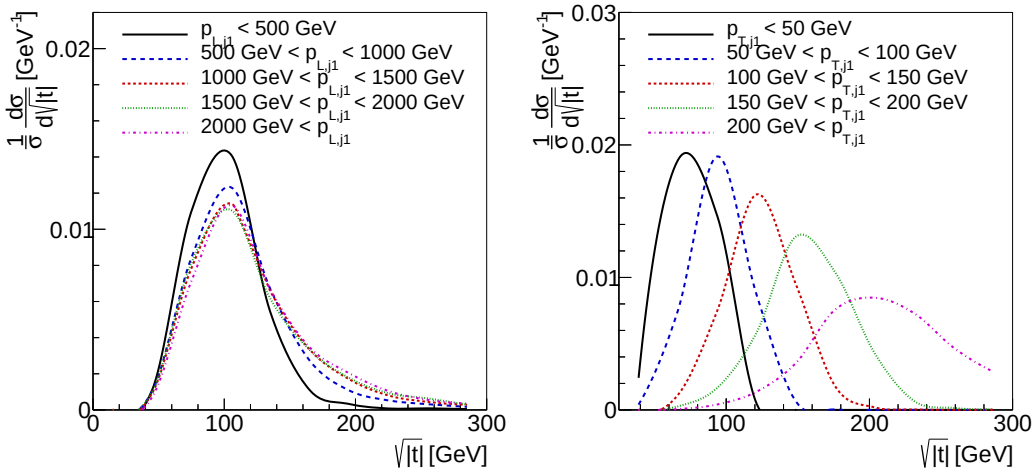

Figure 4.9.: Distributions of the energy scale $\sqrt{|t|}$ of the hard $W^+W^- \to W^+W^-$ process for various p_L (left) or p_T (right) slices of the leading jet.

angles. Limiting the analysis to the signal, i. e. the true Higgs resonance, we find that the tagging jet kinematics and the final-state polarisation are entirely uncorrelated. In other words, the Higgs decay knows nothing about its production. This is of course due to the scalar nature of the Higgs. Including the backgrounds, however, we find a correlation between tagging jet properties and the final polarisation. This reflects the fact that final-state longitudinal gauge bosons have a higher probability to be Higgs decay products, while transverse vector bosons are more likely to stem from background interactions.

4.4.4. Statistical significance

It is now clear that a modification of the Higgs-gauge coupling structure induces qualitative changes in the distributions of different tagging jet properties. In a next step, we estimate the sensitivity in the parameter space based on these different observables, thus quantifying the significance of the signatures discussed above. To this end we ask the question which region of the parameter space can be excluded given a certain statistical sample size, assuming there is no new physics beyond the Standard Model.

More specifically, we generate a number of toy data samples based on the Standard Model. Each of them includes statistical fluctuations for a given integrated luminosity. Then the (a_L, a_T) parameter space of the simple model is checked for compatibility with each of these data samples. These compatibility tests are done for all observables discussed above. In case of the cross section and the asymmetry A_ϕ, the full probability density functions are calculated. For all other kinematic observables, the compatibility

Observables	Limit on a_L	Limit on a_T
σ	(≤ 1.07)	(≤ 1.97)
σ, $p_{T,j1}$	(0.76 – 1.08)	(0.25 – 1.79)
σ, $p_{T,j1}$, $p_{T,j2}$	(0.82 – 1.08)	(0.56 – 1.68)
σ, $\bar{p}_T$	(0.79 – 1.07)	(0.41 – 1.73)
σ, A_{pT}	(0.65 – 1.08)	(≤ 1.86)
σ, $\bar{p}_T$, A_{pT}	(0.78 – 1.09)	(0.39 – 1.73)
σ, $\Delta\phi_{jj}$	(0.49 – 0.54), (0.95 – 1.06)	(0.83 – 1.17), (1.89 – 1.94)
σ, A_ϕ	(0.52 – 0.64), (0.94 – 1.06)	(0.82 – 1.15), (1.77 – 2.00)
σ, $\lvert(\vec{p}_{T,j1} + \vec{p}_{T,j1})\rvert$	(0.93 – 1.06)	(0.66 – 1.28)
σ, $\lvert(\vec{p}_{T,j1} - \vec{p}_{T,j1})\rvert$	(≤ 0.61), (0.85 – 1.08)	(≤ 1.96)
σ, $p_{T,j1}$, $p_{T,j2}$, $\Delta\phi_{jj}$	(0.92 – 1.08)	(0.82 – 1.19)
σ, $p_{T,j1}$, $p_{T,j2}$, A_ϕ	(0.92 – 1.08)	(0.80 – 1.18)

Table 4.6.: Limits on $a_{L,T} \in [0, 2]$ in the absence of a signal based on different combinations of observables. The limits are given at 95% CL assuming statistics representing an integrated luminosity of 300 fb^{-1}. For the limit on a_L, a_T is allowed to float freely, and vice versa.

is probed by χ^2 tests on the normalised distributions.

These tests give a number of p-values for each combination of parameter point (a_L, a_T) and tested observable. If the median of these values is below 0.05, the parameter point (a_L, a_T) is expected to be excluded at 95% CL in the absence of a signal based on this observable. The results from certain combinations of observables are statistically independent. In this case they can be combined, for which we use Fisher's method [85].

In table 4.6 the resulting limits on the parameters $a_{L,T}$ based on different combinations of observables are given. It turns out that observables including the cross section and the angular correlation between the jets impose the strongest constraints on the parameter space. On the other hand, an analysis based only on these observables leads to a binary ambiguity: there is a phase-space region around $a_L \approx 0.6$, $a_T \approx 1.8$ which yields rates and angular correlations between the jets similar to the Standard Model. This blind spot can be removed by including the transverse jet momenta in the analysis. In the end, the strongest exclusion limits come from a combination of the Higgs-resonance cross section, the asymmetry A_ϕ or equivalently the full $\Delta\phi_{jj}$ distribution, and the transverse momenta of the leading and subleading jet.

The expected exclusion regions based on these observables are shown in the left panels of figure 4.10. Assuming data equivalent to 300 fb^{-1}, most of the (a_L, a_T) plane can be excluded. We find that the longitudinal coupling a_L should be measurable at a precision

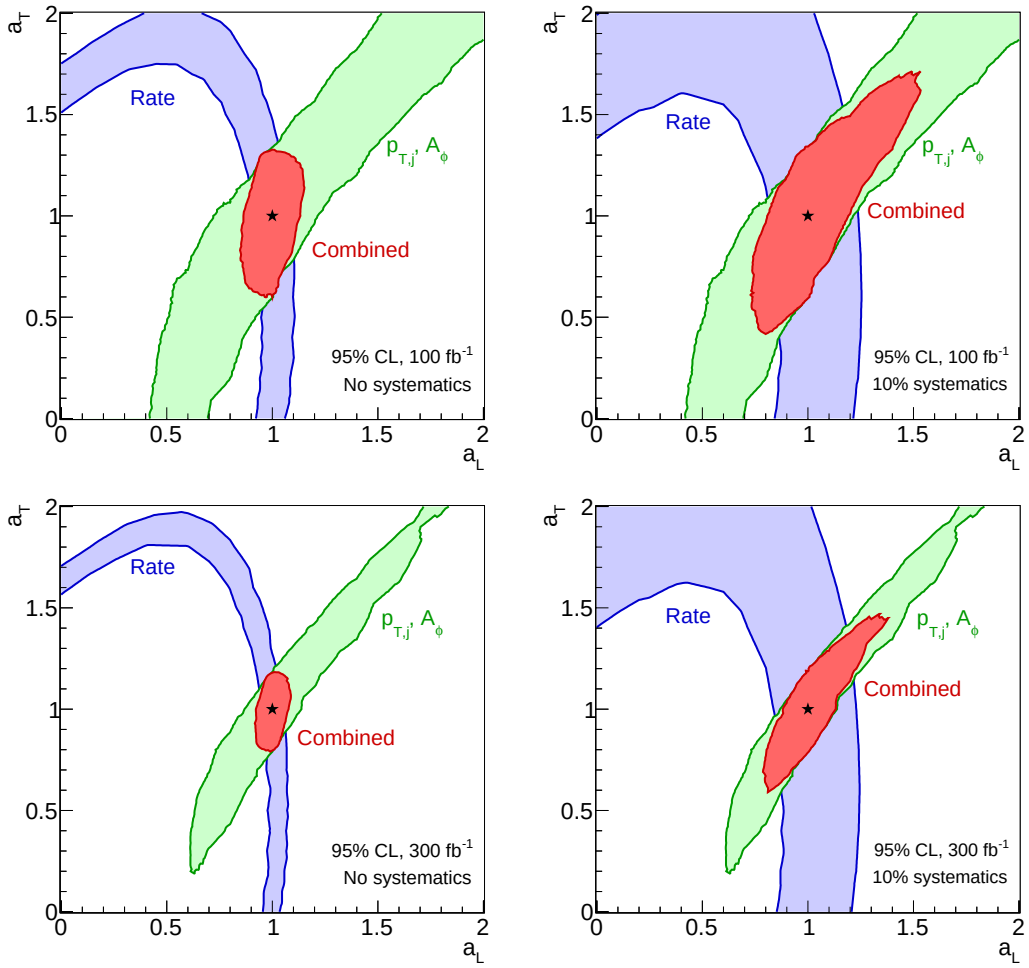

Figure 4.10.: Expected exclusion regions at 95% CL after 100 fb^{-1} (top panels) and 300 fb^{-1} (bottom panels) of data in the absence of a signal. The constraints from the Higgs-resonance cross section (blue), kinematic properties of the tagging jets (green), and their combination (red) are shown. The results in the left panels do not take into account any systematic uncertainties. In the right panels we include an additional 10% uncertainty on the Higgs production and decay rate.

of $\mathcal{O}(10\%)$, while the transverse coupling a_T should be measurable at $\mathcal{O}(20\%)$. The mirrored solution with $a_L \approx -1$, $a_T \approx -1$ cannot be excluded in this channel, but the $H \to \gamma\gamma$ decay, mediated by a top loop and a W loop, should easily be sensitive to this sign change.

Note that these results only take into account statistical uncertainties within our parton-level analysis. A realistic analysis will have to consider theoretical and systematic uncertainties as well. As a rough demonstration, the right panels of figure 4.10 show the exclusion limits based on the same observables, assuming an additional Gaussian uncertainty of 10% on the measurement of the cross section.

4.4.5. Comparison to other approaches

The analysis strategy of this chapter focuses on the kinematics of the tagging jets at the Higgs resonance. But, as discussed in section 2.3.4 and in the introduction of this chapter, there are other approaches to the Higgs-gauge sector. On the one hand, it is possible to measure lepton properties instead of tagging-jet observables, and thus probe the polarisation of the final gauge boson pair. On the other hand, one can leave the Higgs resonance and analyse the high-energy regime of gauge boson scattering. We will now briefly demonstrate both of these approaches inside our framework and discuss their results.

Lepton kinematics

We begin with the lepton kinematics at the Higgs resonance. The observables most sensitive to the polarisation of the final gauge bosons are decay angles, which have been discussed in detail in chapter 3. But in the leptonic W^+W^- mode, these angles cannot be reconstructed well due to the two neutrinos. As alternative observables, the transverse momenta of the two leptons, their separation in the azimuthal angle $\Delta\phi_{\ell\ell}$, their invariant mass $m_{\ell\ell}$, and the missing transverse momentum have been suggested [13].

An analysis of these observables shows that $\Delta\phi_{\ell\ell}$ and $m_{\ell\ell}$ are indeed sensitive to the Higgs-gauge coupling structure. In figure 4.11 their distributions for the usual parameter points are given. We find that longitudinal gauge bosons favour back-to-back leptons, while transverse gauge bosons yield more collinear leptons, in agreement with the literature [13]. However, these signatures are not as pronounced as those we found in the tagging jet observables in the previous sections.

A statistical analysis of the significance of these deviations confirms this result. Following the same procedure as in the previous section, we determine exclusion regions in the (a_L, a_T) plane based on the leptonic observables and the Higgs-resonance cross section. We find that after 300 fb^{-1} of data and without taking systematic uncertainties into account, the longitudinal coupling can be measured on the $\mathcal{O}(40\%)$ level, while the transverse coupling can only be measured to a precision of $\mathcal{O}(80\%)$. Of course, lepton

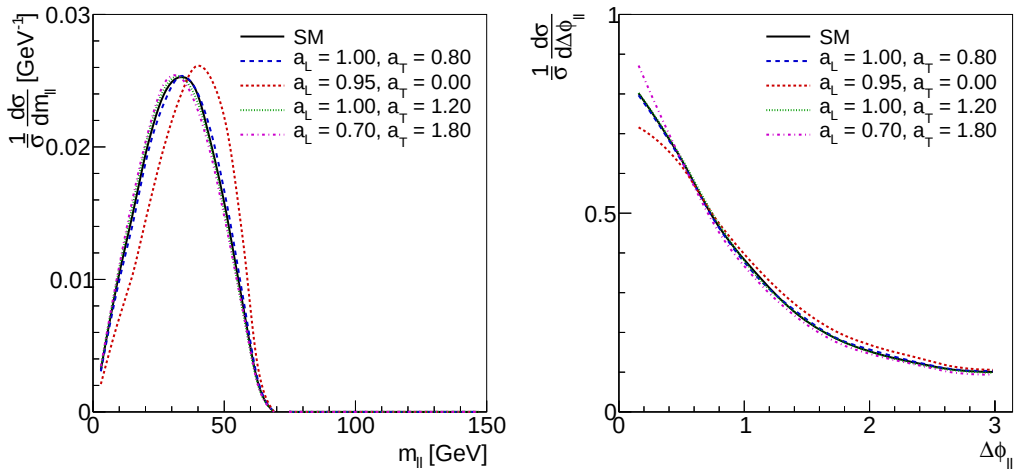

Figure 4.11.: Left: distribution of the dilepton mass in the Standard Model and in four scenarios with modified Higgs-gauge couplings. Right: distribution of the azimuthal angle between the two leptons in the same five scenarios.

observables will suffer less from systematic uncertainties than jet measurements, but this is still significantly worse than the $\mathcal{O}(20\%)$ precision of the tagging-jet approach presented above. Keeping in mind the limitations of our study, it seems that tagging-jet observables are sensitive to the Higgs-gauge coupling structure at lower statistics than lepton observables.

High-energy cross section

As a second alternative approach, we analyse the cross section after a selection optimised for high-energy longitudinal gauge boson pairs. As demonstrated in section 2.3.1, a longitudinal Higgs-gauge coupling different from the Standard Model should lead to a non-cancellation of Higgs and gauge amplitude. This should give an increase of the cross section at large energy scales.

Many sets of selection cuts for such an analysis have been suggested [13, 14, 16–18, 21–23]. Following [14], we analyse the cross section after the cuts of table 4.7. This selection utilises kinematic features both of the leptons and the tagging jets to suppress transverse gauge bosons with respect to longitudinal vector bosons. We apply these cuts in addition to the acceptance cuts of table 4.4, which leads to a difference to the literature: the authors of [14] only require one tagging jet, while our event samples are generated with the requirement of two tagging jets with certain properties. Hence our selection is slightly tighter, and indeed we find lower cross sections than the results quoted in [14].

Leptonic cuts	Jet cuts
$\lvert\eta_\ell\rvert < 2.0$	$\lvert\eta_j\rvert > 3.0$
$p_{T,\ell} > 100$ GeV	$p_{T,j} > 40$ GeV
$\lvert(\mathbf{p}_{T,\ell 1} - \mathbf{p}_{T,\ell 2})\rvert > 440$ GeV	$E_j > 800$ GeV
$\cos\Delta\phi_{\ell\ell} < -0.8$	
$m_{\ell\ell} > 250$ GeV	

Table 4.7.: Selection cuts optimised for high-energy longitudinal gauge boson pairs, as suggested by [14].

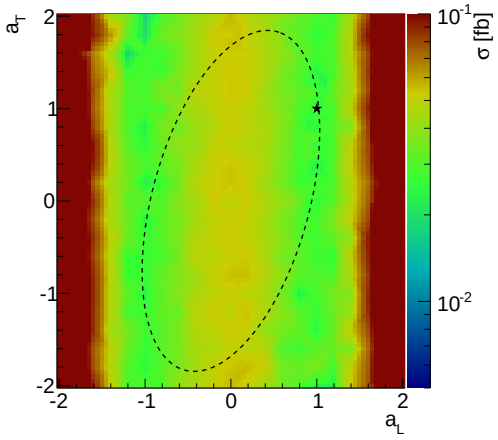

Figure 4.12.: Cross sections after the high-energy selection of table 4.7 as a function of the parameter space of our simple model. The star marks the Standard Model, while the ellipse denotes the parameter-space region giving a constant cross section at the Higgs resonance.

In figure 4.12 we show the cross section after this selection as a function of the coupling parameters a_L and a_T. Indeed, this high-energy rate does not depend on the transverse Higgs-gauge coupling at all, showing that the selection successfully suppresses transverse contributions. Any modification of the longitudinal coupling, regardless of whether $|a_L| < 1$ or $|a_L| > 1$, leads to an increase in the cross section. This is exactly the expected behaviour and reflects the non-cancellation between the gauge and Higgs amplitudes at high energies for longitudinal Higgs-gauge couplings different from the Standard Model value.

While this effect is clearly visible, the cross sections in question are quite low. Again, the significance of these signatures is measured by calculating exclusion regions in parameter space. We find that even without taking into account the large systematic uncertainties of such a high-energy rate measurement, 300 fb^{-1} of data are not enough to constrain the coupling parameters further than just with the Higgs-resonance cross section. Data of at least $\mathcal{O}\left(1000\ \text{fb}^{-1}\right)$ are needed for this method to become useful, but then the information from jet and lepton kinematics is already much more precise.

Of course we do not claim that such an analysis is useless. On the one hand, the discussion in this chapter is limited to one exemplary set of selection cuts. Other, preferably more loose, selections might yield a better performance. On the other hand, our simple model might not capture all relevant physics that can lead to a cross-section increase at high energies. Heavy resonances or momentum-dependent couplings due to some higher-scale dynamics might be invisible at the Higgs resonance, but give clear signatures in the high-energy limit. Still it is safe to conclude that with the discovery of the Higgs boson the most natural place to analyse the Higgs-gauge sector is the Higgs pole and not the high-energy regime of gauge boson scattering.

4.5. Beyond the simple model

In the analysis above, the Higgs-gauge sector was parameterised in terms of independent longitudinal and transverse Higgs-gauge couplings. While this approach is simple and gives results in agreement with the equivalence theorem and the effective W approximation, one has to pick a reference frame for the definition of the polarisation states, thus breaking Lorentz invariance. The model is also not gauge invariant. In this section these worrisome properties of the simple model are addressed. First the choice of other reference frames is discussed, then the simple model is linked to an approach based on effective field theory.

4.5.1. Reference frame dependence

In the simple model introduced in section 4.2, the polarisation states of the massive gauge bosons are defined in the Higgs rest frame. There are different reasons for this. The Higgs rest frame is in a sense the natural frame of the hard W^+W^- scattering

process. This choice also simplifies the Higgs-gauge coupling structure by removing mixed HV_LV_T contributions. We will later show that this definition also provides an agreement between the simple model and higher-dimensional operators.

But how do the results of the simple model change if the polarised gauge bosons are defined in a different reference frame? To answer this question, we have to understand how polarisation states behave under boosts. In section 2.2.2, the frame dependence of the polarisation basis was discussed in general. Now we will analyse how longitudinal and transverse modes change specifically at the Higgs resonance. For the tagging jet kinematics the polarisations of the initial gauge bosons producing the Higgs are the quantities of interest. For simplicity, we consider the final gauge bosons instead. Typically, the Higgs boson decays to an on-shell and an off-shell W boson, which fixes most of the kinematics.

We assume such a final pair of W^+W^- bosons in the Higgs rest frame with given polarisation. Then a boost into another reference frame is applied in which the Higgs boson has a non-zero momentum $\mathbf{p}_H$. The probability of a transverse boson becoming longitudinal or vice versa during this boost depends on the size of the boost as well as the angle between the boost direction and the W momentum. In section 2.2.2 we have argued that a boost parallel to the momentum of a gauge boson does not induce any mixing between longitudinal and transverse modes, while a boost orthogonal to the momentum maximises this mixing. We average over the angle between the W momentum and the direction of the boost, and calculate the mixing probabilities as a function of the size of the boost, quantified by the Higgs momentum $\mathbf{p}_H$ in the new frame.

The results are given in the left panel of figure 4.13. It turns out that for Higgs momenta around 200 GeV or, equivalently, for γ factors around 2, the probability for a polarisation change reaches $\mathcal{O}(50\%)$. Such a boost essentially randomises the polarisation, washing out any effect that is clear in the Higgs rest frame. As an aside, in the limit of large boosts we find that all modes become longitudinal. This reflects the dominance of longitudinal modes at large energy scales as discussed in section 2.2.2.

In the right panel of figure 4.13, we give the Higgs momentum in the laboratory frame in the Standard Model for the signal process (4.19) after the usual acceptance and Higgs-resonance cuts. Typical values range from 100 to 300 GeV. In the rest frame of the two colliding partons, the Higgs momenta are slightly lower. We therefore expect that the clear phenomenological differences between longitudinal and transverse gauge bosons in the Higgs rest frame mostly vanish if the definition of polarisation states is shifted to the laboratory or partonic centre-of-mass frame. Indeed we find that defining the simple model in one of these alternative frames gives qualitatively similar, but much less pronounced results.

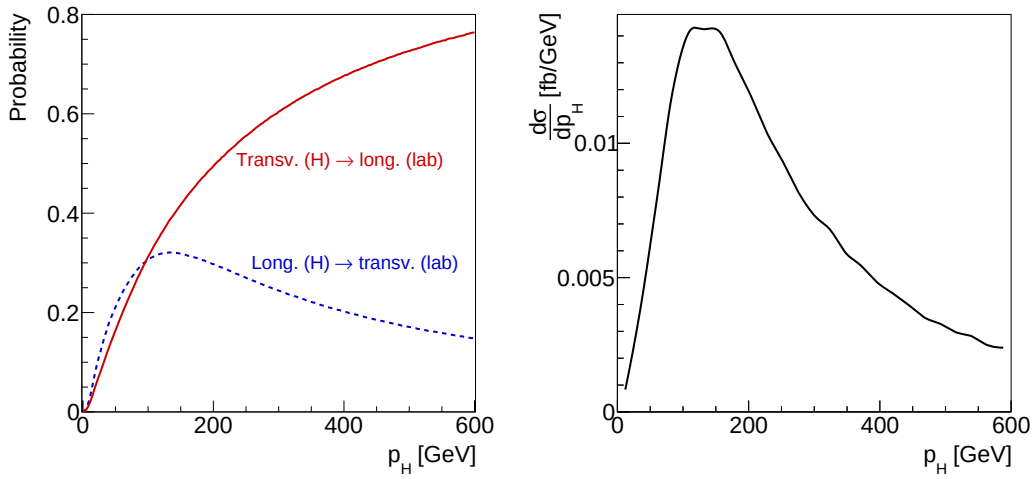

Figure 4.13.: Left: probabilities for a change in polarisation during a boost from the Higgs rest frame to the laboratory frame as a function of the Higgs momentum in the laboratory frame. Right: distribution of the Higgs momentum in the laboratory frame in the Standard Model after our selection cuts.

4.5.2. Effective field theory

Higher-dimensional operators and the Higgs-gauge coupling

Deviations from the Standard Model in the Higgs-gauge sector are often parameterised in the language of effective field theory, i. e. in terms of higher-dimensional operators, as introduced in section 2.1.3. These operators are manifestly gauge invariant and Lorentz invariant. A link between effective field theory and the simple model of section 4.2 can thus demonstrate that the separation of longitudinal and transverse Higgs-gauge couplings at finite energies is indeed physical and does not necessarily imply Lorentz violation.

As examples we consider the two dimension-six electroweak operators

$$\mathcal{O}_{\phi,2} = \frac{1}{2}\partial_\mu \left(\phi^\dagger\phi\right) \partial^\mu \left(\phi^\dagger\phi\right) \tag{4.28}$$

and

$$\mathcal{O}_W = (D_\mu\phi)^\dagger \hat{W}^{\mu\nu} (D_\nu\phi) \ , \tag{4.29}$$

following the conventions of [34]. As discussed in section 2.1.3, these operators can for instance arise in strongly interacting Higgs sectors such as Little Higgs and Holo-

graphic Higgs models. We will now analyse the effect of these operators on the HWW interaction.

The operator $\mathcal{O}_{\phi,2}$ does not contain a direct contribution to the HWW vertex. However, it generates a new contribution to the kinetic term of the Higgs boson,

$$\mathcal{L} \supset \frac{c_{\phi,2} v^2}{\Lambda^2} \partial_\mu H \partial^\mu H \,. \tag{4.30}$$

The canonical normalisation of the Higgs kinetic term can be restored by a field redefinition

$$H \to \frac{1}{\sqrt{1 + c_{\phi,2} v^2/\Lambda^2}} H \,, \tag{4.31}$$

which also introduces a form factor at every Higgs vertex. At leading order in $c_{\phi,2}/\Lambda^2$, this operator therefore modifies the HWW interaction by a universal, constant factor

$$a_L = a_T = 1 - \frac{c_{\phi,2}}{2} \frac{v^2}{\Lambda^2} \,. \tag{4.32}$$

This is equivalent to the $a_L = a_T$ case in our simple model.

The operator $\mathcal{O}_W$ has a more complex phenomenology. It contributes to the interaction of the pure gauge bosons W^i with the Higgs boson, but there is no term of order ϕ^3 or higher representing Higgs-Goldstone couplings. The equivalence theorem therefore predicts that in the high-energy limit $\mathcal{O}_W$ affects the transverse Higgs-gauge couplings, but not the interaction of longitudinal gauge bosons with the Higgs. The Higgs resonance hardly constitutes a high-energy limit, but we still expect that $\mathcal{O}_W$ affects the transverse coupling more strongly than the longitudinal coupling.

An expansion of $\mathcal{O}_W$ in unitary gauge reveals two corrections to the HWW vertex:

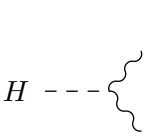

$$= igm_W \Big[\underbrace{g_{\mu\nu} - g_{\mu\nu} \frac{c_W}{2\Lambda^2} \Big((p^H p^+) + (p^H p^-) \Big)}_{a_{L,T}^{(1)}} + \underbrace{\frac{c_W}{2\Lambda^2} \Big(p_\mu^H p_\nu^+ + p_\mu^- p_\nu^H \Big)}_{a_{L,T}^{(2)}} \Big] \,, \tag{4.33}$$

where $p_\mu^\pm$ and p_μ^H are the incoming momenta of the $W^\pm$ and the H, respectively. The first two terms of (4.33) are the Standard Model vertex and a higher-dimensional correction with unchanged Lorentz structure. Assuming the Higgs boson to be on-shell, and since $p^+ + p^- + p^H = 0$, these two terms are equivalent to a coupling modification of

$$a_L^{(1)} = a_T^{(1)} = 1 - \frac{c_W}{2\Lambda^2} (p^H \cdot p^+ + p^H \cdot p^-) = 1 + \frac{c_W m_H^2}{2\Lambda^2} \,. \tag{4.34}$$

The last term in (4.33), on the other hand, features contractions of the type $(p^H \varepsilon^\pm)$, where $\varepsilon^\pm$ are the polarisation vectors of the $W^\pm$ bosons. In the Higgs rest frame, these terms vanish for transverse gauge bosons, but contribute towards the coupling of longitudinal gauge bosons to the Higgs. This contribution is a function of the momenta. So all in all we find

$$a_T^{(2)} = 0\,, \tag{4.35}$$

$$a_L^{(2)} = \frac{c_W}{\Lambda^2} F(p^+, p^-) \tag{4.36}$$

with a momentum-dependent function $F(p^+, p^-)$. This momentum dependence goes beyond the simple model of the previous sections, where a_L and a_T were constants.

The full effect of the operator $\mathcal{O}_W$ on the HWW interaction should then in leading order in c_W/Λ^2 be given by

$$a_L = a_L^{(1)} + a_L^{(2)} = 1 + \frac{c_W}{\Lambda^2}\left(\frac{m_H^2}{2} + F(p^+, p^-)\right)\,, \tag{4.37}$$

$$a_T = a_T^{(1)} + a_T^{(2)} = 1 + \frac{c_W m_H^2}{2\Lambda^2}\,. \tag{4.38}$$

So the operator $\mathcal{O}_W$ affects longitudinal and transverse Higgs-gauge couplings differently. Unlike in our simple model, these couplings are now momentum dependent.

Comparison of signatures

In a next step, we analyse the effects of these operators on the kinematics of the tagging jets and compare the results to the signatures of our simple model. In the case of $\mathcal{O}_{\phi,2}$ this is straightforward: the operator is exactly equivalent to the $a_L = a_T$ part of the parameter space of the simple model. Indeed we find that the cross sections and the kinematic distributions agree exactly between both approaches, confirming (4.32).

For $\mathcal{O}_W$, we first consider the contributions from the first and second part of (4.33) separately before discussing the effect of the full operator. We choose

$$\frac{c_W}{\Lambda^2} = \pm 10\ \text{TeV}^{-2}\,, \tag{4.39}$$

roughly representing current exclusion limits [43]. Using `MadGraph`, samples are generated in these setups for the signal process of (4.19). No backgrounds are included, otherwise the same cuts and technical details as in the previous section are used. In figure 4.14 the resulting $p_{T,j1}$ and $\Delta\phi_{jj}$ distributions are shown as the solid red and blue lines.

The first term of (4.33) leads to an increase of the cross section with positive c_W and a decrease with negative c_W, while the kinematic features remain unaffected, as can

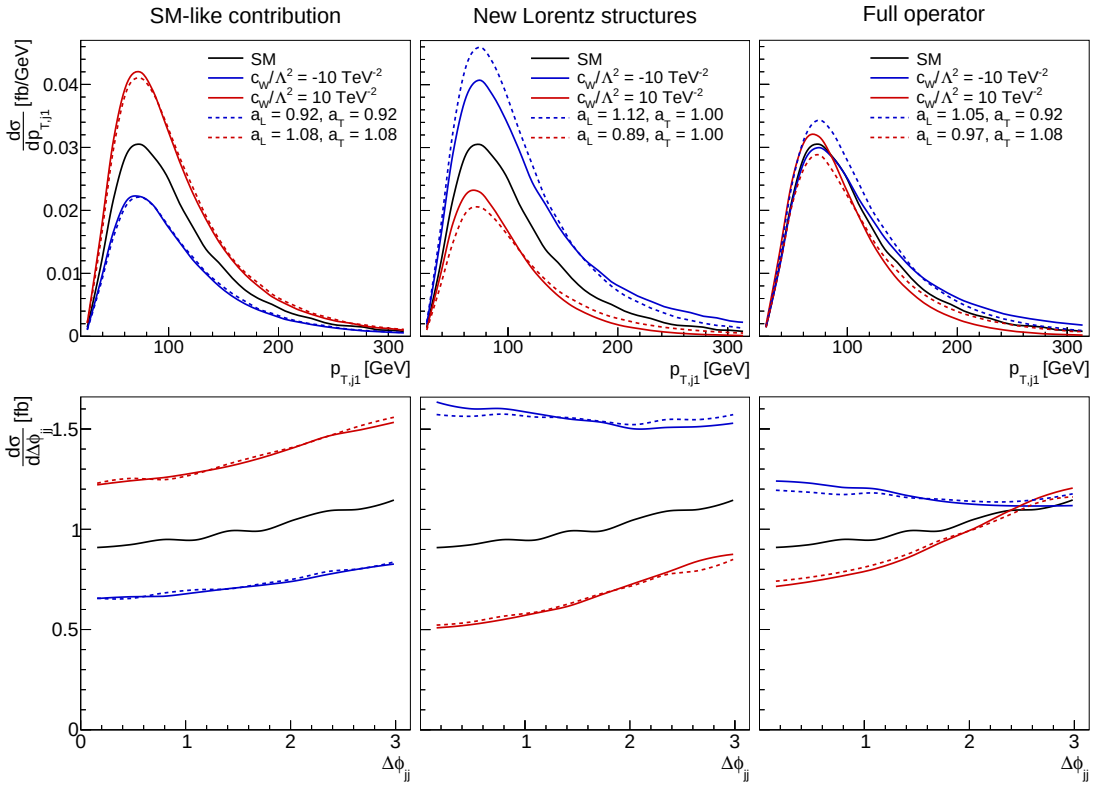

Figure 4.14.: Effects of $\mathcal{O}_W$ on kinematic distributions and the corresponding results from our simple model. We separate the first term (left panels) and second term (middle panels) as defined in (4.33). The right panels show the effect of the full operator.

be seen in the left panels of figure 4.14. This is just the behaviour expected from the discussion above. For comparison, the dashed lines show the results based on our simple model, with parameters following (4.34). The operator results and our simple model agree very well. This is not surprising, since for on-shell Higgs bosons both approaches should be equivalent according to (4.34). Deviations can only arise from off-shell Higgs contributions.

The effect of the second term of (4.33) on the distributions is shown in the middle panels of 4.14. The effect on the rate is now anti-proportional to c_W, reflecting the relative sign between the first and second part of 4.33. Unlike the first part, this term introduces new Lorentz structures and thus also modifies the kinematic distributions. In particular, positive values of c_W slightly soften the tagging jets and favour back-to-back jets. Negative c_W, on the other hand, lead to harder tagging jets and induce a preference for aligned jets.

In order to compare these results to our simple model, we fit a constant a_L to these distributions, while keeping $a_T = 0$ fixed as discussed above. The results are shown as the dotted curves. For $c_W/\Lambda^2 = 10\ \text{TeV}^{-2}$, the fit yields

$$a_L^{(2)} = 0.89\,, \tag{4.40}$$

or equivalently

$$F(p^+, p^-) = -(105\ \text{GeV})^2\,. \tag{4.41}$$

This choice gives good agreement between the operator results and the simple model in both the cross section and the angular correlation between the jets, as can be seen in the bottom middle panel of 4.14. However, there are substantial deviations in the distribution of the transverse jet momentum (upper middle panel of figure 4.14). For positive (negative) c_W, the jets are softer (harder) in the effective field theory results than in our simple model. This discrepancy is due to the fact that the constant couplings a_L and a_T of the simple model cannot account for the momentum-dependent function $F(p^+p^-)$ describing the dynamics of $\mathcal{O}_W$.

Ignoring this complication, the best fit value for $F(p^+, p^-)$ given in (4.41) is interesting. Its negative sign indicates that the effect on the longitudinal coupling from the second part of (4.33) is anti-proportional to the effect of the first term. For the full operator $\mathcal{O}_W$ these contributions are combined and nearly cancel, while the transverse coupling is unaffected by the second part. For $c_W/\Lambda^2 = 10\ \text{TeV}^{-2}$, we find

$$a_L = a_L^{(1)} + a_L^{(2)} = 1 + \frac{c_W}{\Lambda^2}\left(\frac{1}{2}m_H^2 - (105\ \text{GeV})^2\right) = 0.97\,, \tag{4.42}$$

$$a_T = a_T^{(1)} + a_T^{(2)} = 1 + \frac{c_W}{2\Lambda^2}m_H^2 \qquad = 1.08\,. \tag{4.43}$$

It turns out that the operator primarily affects the coupling of transverse gauge bosons to the Higgs, with a suppressed effect on the longitudinal Higgs-gauge couplings. This is exactly what is expected from the simple argument based on the equivalence theorem given above.

Finally, the effect of the full operator on the tagging jet kinematics is shown in the right panels of figure 4.14. The large effects on the cross sections from the individual two terms partly cancel, only a small decrease of the rate for positive c_W and a small increase for negative c_W remains. This corresponds to the large contributions to the longitudinal coupling from the individual two terms, which mostly cancel for the full operator. The kinematic features are the same as for the second term only. Again, the dotted lines show the equivalent results for the simple model. There is good agreement between $\mathcal{O}_W$ and the simple model in the cross section and the angular correlation, but the discrepancy in the distribution of the jet momenta remains as well.

Taking everything into account, the analysed dimension-six operators can be translated into longitudinal and transverse Higgs-gauge couplings. Unlike in our simple model, these couplings can be momentum-dependent. While the qualitative features of both approaches generally agree, this momentum dependence can lead to substantial deviations in certain distributions.

4.6. Conclusions

In this chapter we have developed a new approach to the Higgs-gauge sector. Its aim is the measurement of the polarisation of the initial gauge bosons in W^+W^- scattering at the Higgs resonance. We parameterise the Higgs-gauge sector in a simple model in terms of independent couplings of the Higgs boson to longitudinal and transverse massive gauge bosons. From a theoretical perspective, this model has some worrisome properties: in order to define the polarisation states, Lorentz invariance must be broken. However, we have shown that independent longitudinal and transverse Higgs-gauge couplings can also be generated in an approach based on effective field theory, giving comparable results.

As observables we propose the kinematic properties of the tagging jets, which recoil against the initial gauge bosons and are thus sensitive to their properties. In particular, the effective W approximation predicts that the transverse jet momenta reflect the polarisation of the initial gauge bosons. We find its prediction to be valid at energies much larger than the weak scale, but not at the observed Higgs mass, where the scale of the hard process and the weak scale are not separated enough for the effective W approximation to hold.

Still, an analysis of the full process shows that the transverse momenta of the two jets and the azimuthal angle between them are sensitive to the structure of the Higgs-gauge sector. In a brief comparison, these jet observables in fact give rise to stronger limits on the longitudinal and transverse couplings than alternative approaches based on lepton kinematics or the high-energy cross section. The constraints from these jet observables are orthogonal to those based on the cross section. A combination of these distributions with the rate at the Higgs resonance allows the measurement of the individual longitudinal and transverse Higgs-gauge couplings at the $\mathcal{O}(20\%)$ level using 300 fb^{-1} of data at 13 TeV. While our analysis is limited to the parton level and does not take systematic uncertainties into account, it is safe to assume that this strategy is feasible at the upcoming LHC run.

5. Conclusions

In this thesis we have investigated how a measurement of the polarisation of $W^\pm$ and Z bosons can aid our understanding of the nature of electroweak symmetry breaking. This idea is motivated by the Goldstone boson equivalence theorem, which links longitudinal vector bosons to the Goldstone bosons of the Higgs sector and transverse states to the original electroweak gauge bosons. While this correspondence is only exact in the high-energy limit, a physical difference between longitudinal and transverse modes remains at finite energies.

A well-established approach to polarised gauge boson scattering is the measurement of the cross section at large energies. Any deviation from the Standard Model Higgs-gauge sector leads to an increase of this rate. However, this strategy suffers from large systematic uncertainties and low cross sections, especially after the discovery of a scalar resembling the Standard Model Higgs boson. In this thesis we have analysed two alternative methods.

The first approach is the measurement of angular distributions in the decays of gauge boson pairs. These observables are a model-independent measure of the polarisation of the final gauge bosons in $VV \to VV$ scattering ($V = W^\pm, Z$). In particular, such a strategy is feasible both in the high-energy regime and at the Higgs resonance, and therefore does not necessarily suffer from low rates. Since the relative longitudinal and transverse fractions are measured, the large systematic uncertainties associated to the individual rates cancel.

We demonstrate that this strategy reproduces the correct polarisation fractions. However, when we try to pick a particular gauge boson channel, we face a dilemma: none of them comes without significant problems. In the leptonic WW states, the two neutrinos make the exact reconstruction of the decay angles impossible, and approximate reconstruction methods do not give satisfactory results. The leptonic ZZ and WZ decay modes are reconstructable, but suffer from low rates. The semileptonic gauge boson channels face dangerous QCD backgrounds. All in all, such a measurement is challenging and requires large statistics as well as a careful monitoring of the backgrounds. A more thorough analysis is necessary to judge its feasibility at the LHC.

Our second approach is more radical. We propose to measure the polarisation of the initial gauge bosons in $VV \to VV$ scattering with the kinematic properties of the tagging jets. Instead of the high-energy limit, we focus on the Higgs resonance with its larger cross section. We parameterise the Higgs-gauge sector in a simple model where the couplings of the Higgs boson to longitudinal and transverse massive gauge bosons

are two independent parameters. This definition requires the choice of a reference frame, which means that our model is not Lorentz invariant. We justify this by showing that such independent longitudinal and transverse Higgs-gauge couplings can be generated in the consistent framework of effective field theory, giving comparable results to our simple model.

With this model, we first evaluate the effective W approximation, which predicts an analytical relation between the transverse jet momenta and the polarisation of the initial gauge bosons. While this approximation provides a good description at the resonance of a heavy Higgs boson with $m_H \gtrsim 1$ TeV, we find that its validity becomes worse closer to the weak scale and in particular at the observed Higgs resonance at $m_H = 125$ GeV. We explain this observation in terms of a missing separation between the scale of the hard process and the weak scale, which is necessary for the effective W approximation to hold.

In a next step, we look for the kinematic signatures of a modified Higgs-gauge coupling structure. It turns out that in addition to the cross section at the Higgs resonance, the transverse momenta and angular correlations of the tagging jets are indeed sensitive to the Higgs-gauge sector. The constraints from these kinematic distributions are orthogonal to the constraints from the cross section, so their combination permits an efficient determination of the Higgs-gauge coupling structure. We find that 300 fb^{-1} of LHC data at 13 TeV allow us to measure both longitudinal and transverse couplings at the $\mathcal{O}(20\%)$ level. A brief comparison shows that the bounds based on our novel strategy are stronger than those based on lepton observables and especially than the limits from high-energy rate measurements. We conclude that after the Higgs discovery the natural laboratory to probe the electroweak sector is the Higgs resonance, not the high-energy regime.

This thesis is only a first step towards a measurement at the LHC, and there are several omissions and loose ends. This is especially true for the decay-angle analysis, where the next logical steps are the simulation of scenarios of new physics and the inclusion of backgrounds. The tagging-jet analysis can be extended to other Higgs decay modes, thus improving the statistics, and additional backgrounds such as $t\bar{t}$ production should be simulated. Both approaches presented in this thesis are limited to the parton level, a more thorough analysis should include hadronisation and detector effects. At the same time, the cuts can be optimised and additional techniques such as a central jet veto have to be investigated. Ultimately, both measurement strategies should be combined in order to analyse correlations between the polarisations of initial and final states.

To summarise, we have analysed different strategies to measure the polarisation of massive gauge bosons as probes of the Higgs-gauge sector. In $VV \to VV$ scattering, the final polarisation may be determined with angular distributions in the gauge boson decays. While this model-independent technique works, it is not clear whether it can be realised anytime soon at the LHC. Alternatively, the initial polarisation can

be measured in the kinematics of the tagging jets. We have developed a measurement strategy for this novel approach and found that it should be feasible at the upcoming LHC run. Hopefully, these ideas can contribute to a better understanding of electroweak symmetry breaking, which is one of the fundamental building blocks in our current model of high-energy physics.

Appendix A.

The fine print

A.1. Gauge boson scattering

The process $W_L^+ W_L^- \to W_L^+ W_L^-$ was studied in section 2.3.1. In the Standard Model, it involves seven tree-level diagrams, which are the four-W interaction vertex as well as s-channel and t-channel diagrams involving a photon, a Z boson, or a Higgs boson. According to the Goldstone boson equivalence theorem, their matrix elements in the high-energy limit can be calculated by replacing the external $W^\pm$ bosons with the corresponding Goldstone bosons $w^\pm$. The Feynman rules needed for these diagrams can be derived from the Standard Model Lagrangian (2.28). The Higgs potential contains the interactions between Goldstone bosons and other Goldstone bosons or Higgs bosons:

$$\mathcal{L}_{\text{SM}} \supset -\lambda(\phi^\dagger\phi)^2 \tag{A.1}$$

$$= -\frac{\lambda}{4}(w_1^2 + w_2^2 + w_3^2 + (v+H)^2)^2 \tag{A.2}$$

$$\supset -\frac{\lambda}{4}(2w^+w^- + 2vH)^2 \tag{A.3}$$

with

$$w^\pm \equiv \frac{w_1 \pm \mathrm{i}w_2}{\sqrt{2}}\,. \tag{A.4}$$

Including combinatorial factors, the vertices of interest are given by

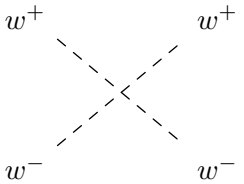

$$\leftrightarrow \quad -4\mathrm{i}\lambda\,, \tag{A.5}$$

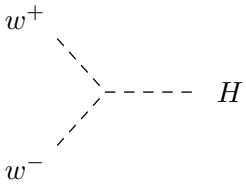

$$\leftrightarrow \quad -2\mathrm{i}\lambda v\,. \tag{A.6}$$

The coupling of the Goldstone bosons to the gauge bosons stems from the kinetic terms of the scalar doublet:

$$\mathcal{L}_{\text{SM}} \supset (D_\mu \phi)^\dagger D^\mu \phi \tag{A.7}$$

$$= \left| (\partial_\mu + \mathrm{i}g\frac{\tau}{2}\cdot W_\mu + \mathrm{i}g'\frac{1}{2}B_\mu)\frac{1}{\sqrt{2}}\begin{pmatrix} -\mathrm{i}w_1 - w_2 \\ v + H + \mathrm{i}w_3 \end{pmatrix}\right|^2 \tag{A.8}$$

$$\supset \left| \frac{1}{\sqrt{2}}(\partial_\mu + \mathrm{i}g\frac{1}{2}W_\mu^3 + \mathrm{i}g'\frac{1}{2}B_\mu)(\mathrm{i}w_1 + w_2)\right|^2 \tag{A.9}$$

$$= (\partial_\mu - \mathrm{i}eA_\mu - \mathrm{i}\frac{e}{2}\left(\frac{s_W}{c_W} - \frac{c_W}{s_W}\right)Z_\mu)w^+(\partial^\mu + \mathrm{i}eA^\mu + \mathrm{i}\frac{e}{2}\left(\frac{s_W}{c_W} - \frac{c_W}{s_W}\right)Z^\mu)w^- \tag{A.10}$$

$$\supset \left[\mathrm{i}eA^\mu + \mathrm{i}\frac{e}{2}\left(\frac{s_W}{c_W} - \frac{c_W}{s_W}\right)Z^\mu\right]\left[w^-\partial_\mu w^+ - w^+\partial_\mu w^-\right]. \tag{A.11}$$

This yields the Feynman rules

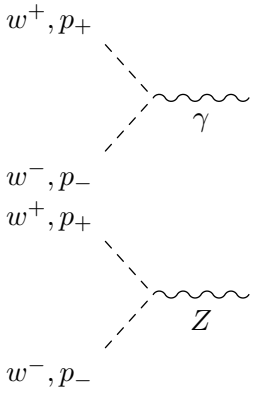

$$\leftrightarrow \quad \mathrm{i}e(p_+^\mu - p_-^\mu)\,, \tag{A.12}$$

$$\leftrightarrow \quad \frac{\mathrm{i}e}{2}\left(\frac{s_W}{c_W} - \frac{c_W}{s_W}\right)(p_+^\mu - p_-^\mu)\,. \tag{A.13}$$

where p_+ and p_- are the incoming four-momenta of the W^+ and W^-, respectively.

With the couplings (A.5), (A.6), (A.12), and (A.13), it is straightforward to write down the matrix elements for all contributing diagrams:

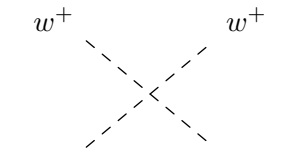

$$= \quad -4\mathrm{i}\lambda\,, \tag{A.14}$$

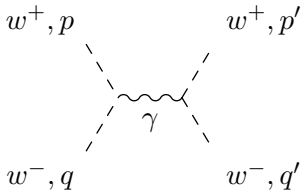

$$= \quad \frac{-\mathrm{i}e^2(p-q)(p'-q')}{s}\,, \tag{A.15}$$

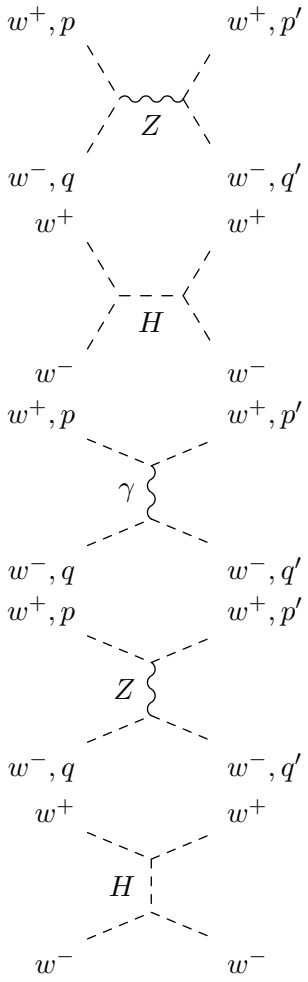

$$= \frac{-\frac{1}{4}\mathrm{i}e^2(\frac{s_W}{c_W} - \frac{c_W}{s_W})^2(p-q)(p'-q')}{s - m_Z^2}\,, \tag{A.16}$$

$$= \frac{-4\mathrm{i}\lambda^2 v^2}{s - m_H^2}\,, \tag{A.17}$$

$$= \frac{-\mathrm{i}e^2(p+p')(q+q')}{t}\,, \tag{A.18}$$

$$= \frac{-\frac{1}{4}\mathrm{i}e^2(\frac{s_W}{c_W} - \frac{c_W}{s_W})^2(p+p')(q+q')}{t - m_Z^2}\,, \tag{A.19}$$

$$= \frac{-4\mathrm{i}\lambda^2 v^2}{t - m_H^2}\,. \tag{A.20}$$

A.2. Gauge boson decays

In section 3.1, the tree-level angular decay distributions of longitudinal and transverse massive vector bosons were given. These distributions are the key ingredient to the measurement strategy discussed throughout chapter 3. Here we give the calculation of these results in detail.

Assume a vector boson V with momentum

$$\tilde{p}_V^\mu = (E, 0, 0, p_3)^\mu\,, \tag{A.21}$$

mass m_V and polarisation vector $\tilde{\varepsilon}$. As polarisation basis we use the two transverse modes

$$\tilde{\varepsilon}_\pm^\mu = \frac{1}{\sqrt{2}}(0, 1, \pm\mathrm{i}, 0)^\mu \tag{A.22}$$

and the longitudinal polarisation

$$\tilde{\varepsilon}_L^\mu = \frac{1}{\sqrt{E^2 - k_3^2}}(k_3, 0, 0, E)^\mu \,. \tag{A.23}$$

Boosting into the V reference frame, the transverse states remain unchanged,

$$\varepsilon_\pm^\mu = \tilde{\varepsilon}_\pm^\mu = \frac{1}{\sqrt{2}}(0, 1, \pm\mathrm{i}, 0)^\mu \,, \tag{A.24}$$

while the longitudinal polarisation becomes

$$\varepsilon_L^\mu = (0, 0, 0, 1)^\mu \,. \tag{A.25}$$

From now on, all quantities will be given in this V rest frame.

Now, let V decay into a fermion f_1 with momentum

$$p_1^\mu = (E_1, \mathbf{p})^\mu \tag{A.26}$$

and mass m_1 and an anti-fermion $\bar{f}_2$ with momentum

$$p_2^\mu = (E_2, -\mathbf{p})^\mu \tag{A.27}$$

and mass m_2. Let θ be the angle between $\mathbf{p}$ and the ε_L, or equivalently, the angle between $\mathbf{p}$ and the spatial momentum of the V boson in the original reference frame, $\tilde{\mathbf{p}}_W$. Crucially, this definition depends on the original reference frame. This subtlety will be discussed at the end of this section. Let g_V and g_A denote the vector and axial coupling structure of the decay. Later the result will be rephrased in terms of the coupling of V to left-handed and right-handed fermions,

$$c_L = g_V - g_A \,, \tag{A.28}$$

$$c_R = g_V + g_A \,. \tag{A.29}$$

Then the amplitude for this decay is given by

$$\mathcal{M} = \bar{u}(p_1) \not{\varepsilon} \left(g_V + g_A \gamma_5\right) v(p_2) \,. \tag{A.30}$$

Squaring and summing over the fermionic spins (but not the vector boson states) gives

$$|\mathcal{M}|^2 \propto \sum_{\text{spins}} \bar{v}(p_2) \not{\varepsilon}^* \left(g_V + g_A \gamma_5\right) u(p_1) \bar{u}(p_1) \not{\varepsilon} \left(g_V + g_A \gamma_5\right) v(p_2) \tag{A.31}$$

$$\propto \mathrm{Tr}\left[\not{\varepsilon}^* \left(g_V + g_A \gamma_5\right) u(p_1) \bar{u}(p_1) \not{\varepsilon} \left(g_V + g_A \gamma_5\right) v(p_2) \bar{v}(p_2)\right] \tag{A.32}$$

$$\propto \mathrm{Tr}\left[\not{\varepsilon}^* \left(g_V + g_A \gamma_5\right) \left(\not{p}_1 + m_1\right) \not{\varepsilon} \left(g_V + g_A \gamma_5\right) \left(\not{p}_2 - m_2\right)\right] . \tag{A.33}$$

Most of these terms vanish inside the trace, leaving only

$$|\mathcal{M}|^2 \propto g_V^2 \,\mathrm{Tr}\left[\not{\varepsilon}^* \not{p}_1 \not{\varepsilon} \not{p}_2\right] + g_V g_A \,\mathrm{Tr}\left[\not{\varepsilon}^* \not{p}_1 \not{\varepsilon} \gamma_5 \not{p}_2\right] + g_V g_A \,\mathrm{Tr}\left[\not{\varepsilon}^* \gamma_5 \not{p}_1 \not{\varepsilon} \not{p}_2\right] + g_A^2 \,\mathrm{Tr}\left[\not{\varepsilon}^* \gamma_5 \not{p}_1 \not{\varepsilon} \gamma_5 \not{p}_2\right] - m_1 m_2 g_V^2 \,\mathrm{Tr}\left[\not{\varepsilon}^* \not{\varepsilon}\right] - m_1 m_2 g_A^2 \,\mathrm{Tr}\left[\not{\varepsilon}^* \gamma_5 \not{\varepsilon} \gamma_5\right]. \quad \text{(A.34)}$$

This evaluates to

$$|\mathcal{M}|^2 \propto 4(g_V^2 + g_A^2)\Big(p_1 \cdot \varepsilon^* \, p_2 \cdot \varepsilon - p_1 \cdot p_2 \, \varepsilon^* \cdot \varepsilon + p_1 \cdot \varepsilon \, p_2 \cdot \varepsilon^*\Big) + 8 i g_V g_A \, \epsilon^{\mu\nu\rho\sigma} \varepsilon^*_\mu p_{1\,\nu} \varepsilon_\rho p_{2\,\sigma} - 4 m_1 m_2 (g_V^2 - g_A^2) \varepsilon^* \cdot \varepsilon \quad \text{(A.35)}$$

or equivalently

$$|\mathcal{M}|^2 \propto 2(c_L^2 + c_R^2)\Big(p_1 \cdot \varepsilon^* \, p_2 \cdot \varepsilon - p_1 \cdot p_2 \, \varepsilon^* \cdot \varepsilon + p_1 \cdot \varepsilon \, p_2 \cdot \varepsilon^*\Big) + 2i(c_R^2 - c_L^2) \, \epsilon^{\mu\nu\rho\sigma} \varepsilon^*_\mu p_{1\,\nu} \varepsilon_\rho p_{2\,\sigma} - 4 m_1 m_2 c_L c_R \varepsilon^* \cdot \varepsilon \,. \quad \text{(A.36)}$$

Plugging in the longitudinal polarisation vector (A.25) gives

$$p_1 \cdot \varepsilon_L^* \, p_2 \cdot \varepsilon_L + p_1 \cdot \varepsilon_L \, p_2 \cdot \varepsilon_L^* = -2\mathbf{p}^2 \cos^2\theta \quad \text{(A.37)}$$

and

$$\epsilon^{\mu\nu\rho\sigma} \varepsilon^*_{L\,\mu} p_{1\,\nu} \varepsilon_{L\,\rho} p_{2\,\sigma} = 0 \,. \quad \text{(A.38)}$$

For the transverse polarisation vectors (A.24), one finds

$$p_1 \cdot \varepsilon_\pm^* \, p_2 \cdot \varepsilon_\pm + p_1 \cdot \varepsilon_\pm \, p_2 \cdot \varepsilon_\pm^* = \frac{1}{2}\Big((p_x \mp \mathrm{i}p_y)(-p_x \mp \mathrm{i}p_y) + (p_x \pm \mathrm{i}p_y)(-p_x \pm \mathrm{i}p_y)\Big) \quad \text{(A.39)}$$

$$= -(p_x^2 + p_y^2) \quad \text{(A.40)}$$

$$= -\mathbf{p}^2(1 - \cos^2\theta) \quad \text{(A.41)}$$

and

$$\epsilon^{\mu\nu\rho\sigma} \varepsilon^*_{\pm\,\mu} p_{1\,\nu} \varepsilon_{\pm\,\rho} p_{2\,\sigma} = \epsilon^{1\nu 2\sigma} \frac{1}{\sqrt{2}} p_{1\,\nu} (\pm \frac{\mathrm{i}}{\sqrt{2}}) p_{2\,\sigma} + \epsilon^{2\nu 1\sigma} (\mp \frac{\mathrm{i}}{\sqrt{2}}) p_{1\,\nu} \frac{1}{\sqrt{2}} p_{2\,\sigma} \quad \text{(A.42)}$$

$$= \pm \mathrm{i}(E_1 + E_2)|\mathbf{p}| \cos\theta^* \,. \quad \text{(A.43)}$$

Putting everything together and shuffling the pieces around some more leads to

$$|\mathcal{M}|^2 \propto \begin{cases} E_1 E_2 + \mathbf{p}^2(1 - 2\cos^2\theta) + 2\frac{c_L c_R}{c_L^2 + c_R^2} m_1 m_2 & \text{for } V_L \\ E_1 E_2 + \mathbf{p}^2 \cos^2\theta^* & \\ \qquad \pm \frac{c_L^2 - c_R^2}{c_L^2 + c_R^2}(E_1 + E_2)|\mathbf{p}| \cos\theta^* + 2\frac{c_L c_R}{c_L^2 + c_R^2} m_1 m_2 & \text{for } V_T \,. \end{cases} \quad \text{(A.44)}$$

The differential decay width is proportional to $|\mathcal{M}|^2$, so this gives exactly the decay distribution of longitudinal gauge bosons,

$$\frac{\mathrm{d}\sigma(V_L \to f_1 f_2)}{\mathrm{d}\cos\theta^*} \propto E_1 E_2 + \mathbf{p}^2(1 - 2\cos^2\theta) + 2\frac{c_L c_R}{c_L^2 + c_R^2} m_1 m_2 \,, \tag{A.45}$$

and the distribution of transverse gauge bosons,

$$\frac{\mathrm{d}\sigma(V_T \to f_1 f_2)}{\mathrm{d}\cos\theta^*} \propto E_1 E_2 + \mathbf{p}^2\cos^2\theta^* \pm \frac{c_L^2 - c_R^2}{c_L^2 + c_R^2}(E_1 + E_2)|\mathbf{p}|\cos\theta^* + 2\frac{c_L c_R}{c_L^2 + c_R^2} m_1 m_2 \,. \tag{A.46}$$

E_1, E_2 and $|\mathbf{p}|$ are fixed by energy-momentum conservation to

$$E_1 = \frac{m_V^2 + m_1^2 - m_2^2}{2m_V} \,, \tag{A.47}$$

$$E_2 = \frac{m_V^2 + m_2^2 - m_1^2}{2m_V} \,, \tag{A.48}$$

$$|\mathbf{p}| = \frac{1}{2} m_V \lambda^{\frac{1}{2}}\left(1, \frac{m_1^2}{m_V^2}, \frac{m_2^2}{m_V^2}\right) \,, \tag{A.49}$$

where $\lambda(x, y, z)$ is the kinematic function given in (3.6).

In the limit of vanishing fermion masses, $E_1 = E_2 = |\mathbf{p}| = \frac{1}{2} m_V$, and the results simplify to

$$\frac{\mathrm{d}\sigma(V_L \to f_1 f_2)}{\mathrm{d}\cos\theta^*} \propto 1 - \cos^2\theta^* \,, \tag{A.50}$$

$$\frac{\mathrm{d}\sigma(V_T \to f_1 f_2)}{\mathrm{d}\cos\theta^*} \propto 1 + \cos^2\theta^* \pm 2\frac{c_L^2 - c_R^2}{c_L^2 + c_R^2}\cos\theta^* \tag{A.51}$$

in agreement with the literature. For W bosons, where $c_R = 0$, and including normalisation factors, this gives the well-known results

$$\frac{1}{\sigma}\frac{\mathrm{d}\sigma(W_L \to f_1 f_2)}{\mathrm{d}\cos\theta^*} = \frac{3}{4}(1 - \cos^2\theta^*) \tag{A.52}$$

and

$$\frac{1}{\sigma}\frac{\mathrm{d}\sigma(W_T \to f_1 f_2)}{\mathrm{d}\cos\theta^*} = \frac{3}{8}(1 \pm \cos\theta^*)^2 \,. \tag{A.53}$$

At first sight, this derivation seems to be independent of the choice of the original coordinate system, as everything was calculated in the rest frame of V. That is wrong. The definition of longitudinal polarisation, or in other words the definition of the reference axis for the definition of $\cos\theta^*$, depends on the V momentum in the original reference frame, $\tilde{\mathbf{p}}_V$. So the variable θ^* depends on the reference frame – as it must, because the polarisation of gauge bosons is also frame dependent, as discussed in section 2.2.2.

A.3. Higgs production in weak boson fusion

In order to calculate the full cross section for the process

$$pp \to Hqq'X \tag{A.54}$$

in the effective W approximation, the partonic cross sections $W^+W^- \to H$ for different W polarisation states are needed. The W^+W^-H vertex corresponds to a factor of $igm_W g_{\mu\nu}$, so the total matrix element squared is given by

$$|\mathcal{M}|^2 = g^2 m_W^2 \, |\varepsilon_+^* \cdot \varepsilon_-|^2 \,. \tag{A.55}$$

Here $\varepsilon_\pm$ are the polarisation vectors of the $W^\pm$ bosons, respectively. Assuming the Higgs-boson to be on-shell, the cross section in the centre-of-mass frame is

$$\mathrm{d}\hat{\sigma}(W^+W^- \to H) = \frac{\pi}{\lambda^{\frac{1}{2}}(\hat{s}, m_W^2, m_W^2)} \; |\mathcal{M}|^2 \; \delta(\hat{s} - m_H^2) \,, \tag{A.56}$$

where $\hat{s}$ is the centre-of-mass energy squared of the W^+W^- system and $\lambda(x,y,z)$ is the kinematic function given in (3.6). This gives

$$\mathrm{d}\hat{\sigma} = \frac{\pi g^2 m_W^2 |\varepsilon_+^* \cdot \varepsilon_-|^2}{m_H \sqrt{m_H^2 - 4m_W^2}} \, \delta(\hat{s} - m_H^2) \,. \tag{A.57}$$

Due to the form of the polarisation vectors (2.49) to (2.51), the product $|\varepsilon_+^* \cdot \varepsilon_-|^2$ yields

$$|\varepsilon_+^* \cdot \varepsilon_-|^2 = \begin{cases} \frac{(m_H^2 - 2m_W^2)^2}{4m_W^4} & \text{if both } W \text{ are longitudinally polarised} \\ 1 & \text{if both } W \text{ have the same transverse polarisation} \\ 0 & \text{for differing polarisations} \,. \end{cases} \tag{A.58}$$

Taking everything into account, the cross-sections for the process $W^+W^- \to H$ are given by

$$\mathrm{d}\hat{\sigma}(W_T^+W_T^- \to H) = \frac{\pi g^2 m_W^2}{2m_H \sqrt{m_H^2 - 4m_W^2}} \, \delta(\hat{s} - m_H^2) \,, \tag{A.59}$$

$$\mathrm{d}\hat{\sigma}(W_L^+W_L^- \to H) = \frac{\pi g^2 (m_H^2 - 2m_W^2)^2}{4m_W^2 m_H \sqrt{m_H^2 - 4m_W^2}} \, \delta(\hat{s} - m_H^2) \,, \tag{A.60}$$

$$\mathrm{d}\hat{\sigma}(W_T^+W_L^- \to H) = 0 \,, \tag{A.61}$$

$$\mathrm{d}\hat{\sigma}(W_L^+W_T^- \to H) = 0 \,, \tag{A.62}$$

where the additional factor of $\frac{1}{2}$ in the transverse result comes from averaging over initial polarisations.

Appendix B.

Numerical results

B.1. Decay distributions

In section 3.4.2, the distribution of decay angles in different gauge boson channels was discussed. We give these distributions both before and after reconstruction in the figures B.1 to B.9.

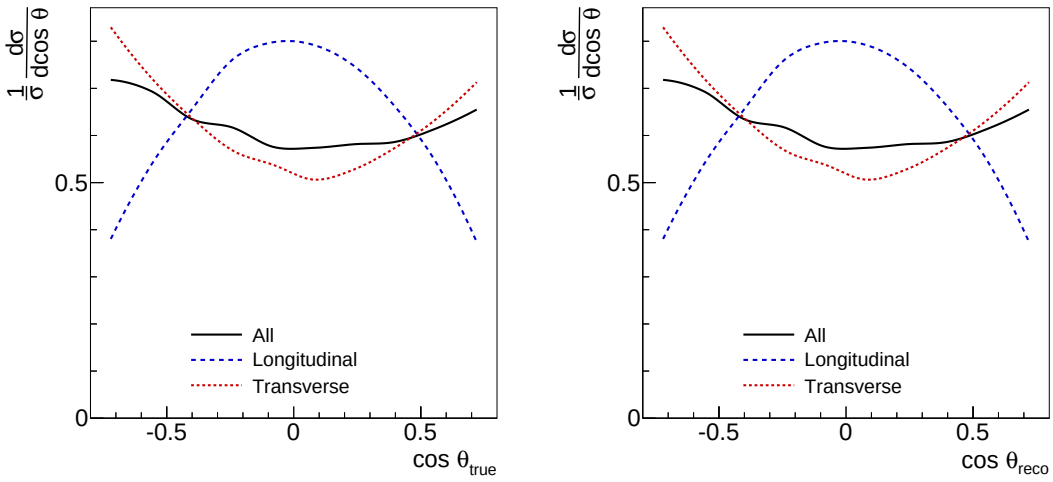

Figure B.1.: Distribution of decay angles in the $ZZ \to (\ell^+\ell^-)\ (\nu\bar{\nu})$ channel after the high-energy event selection. Only the decay angle for the $\ell^+\ell^-$ pair is reconstructed. Left: truth-level results. Right: after reconstruction.

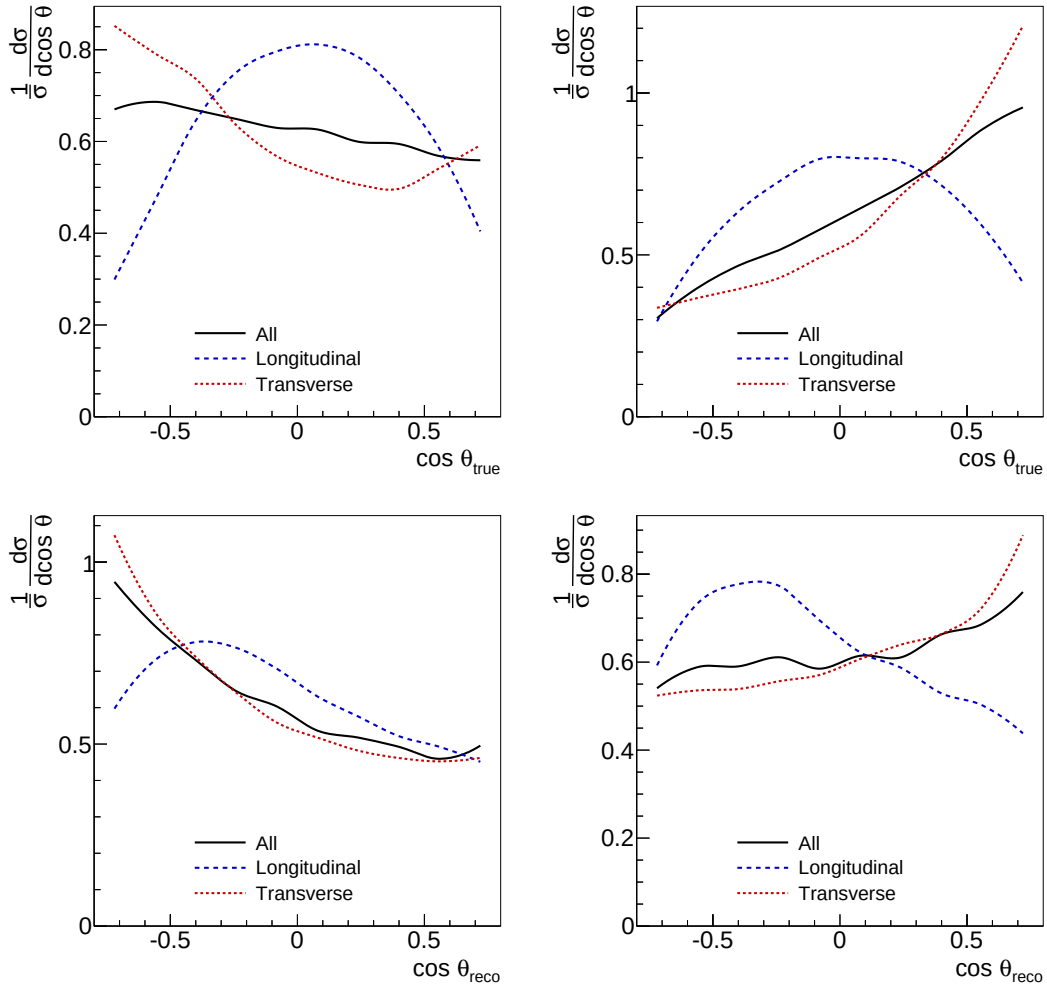

Figure B.2.: Distribution of decay angles in the $W^+W^- \to (\ell^+\nu)\ (\ell^-\bar{\nu})$ channel after the high-energy event selection. Top: truth-level results. Bottom: after reconstruction. Left: W^+ decay. Right: W^- decay.

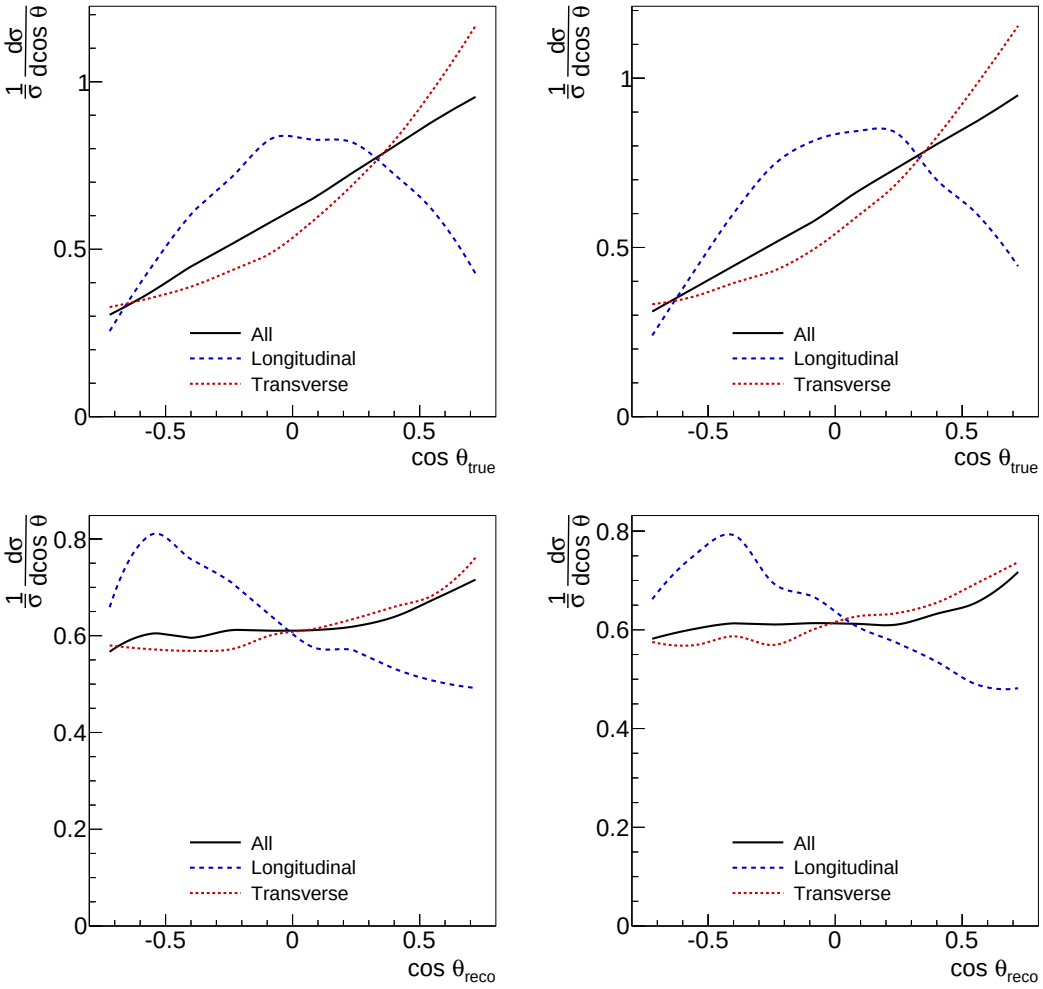

Figure B.3.: Distribution of decay angles in the $W^{\pm}W^{\pm} \to (\ell^{\pm}\nu)\ (\ell^{\pm}\nu)$ channel after the high-energy event selection. Top: truth-level results. Bottom: after reconstruction. Left: decay of W with lower rapidity. Right: decay of W with larger rapidity.

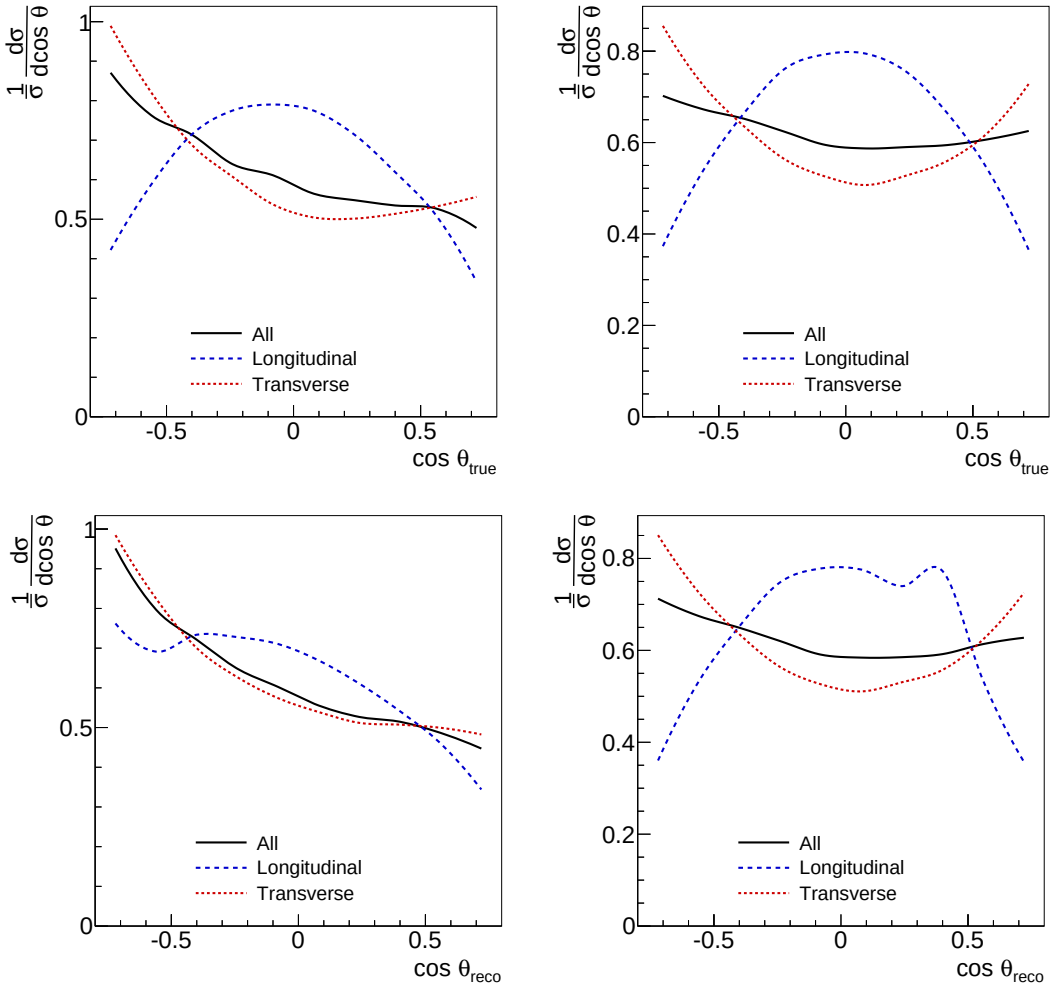

Figure B.4.: Distribution of decay angles in the $WZ \to (\ell^{\pm}\nu)\ (\ell^{+}\ell^{-})$ channel after the high-energy event selection. Top: truth-level results. Bottom: after reconstruction. Left: W decay. Right: Z decay.

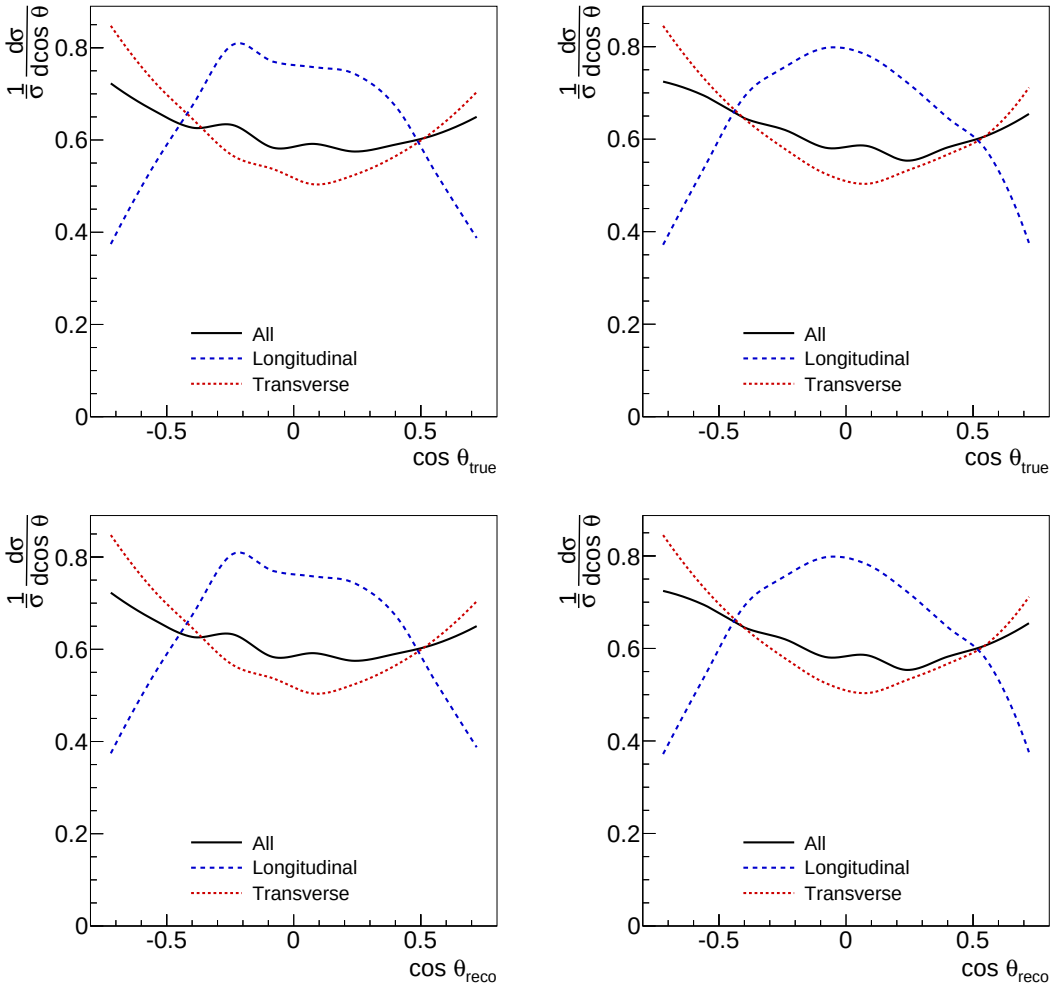

Figure B.5.: Distribution of decay angles in the $ZZ \to (\ell^+\ell^-)\ (\ell^+\ell^-)$ channel after the high-energy event selection. Top: truth-level results. Bottom: after reconstruction. Left: decay of Z with lower rapidity. Right: decay of Z with larger rapidity.

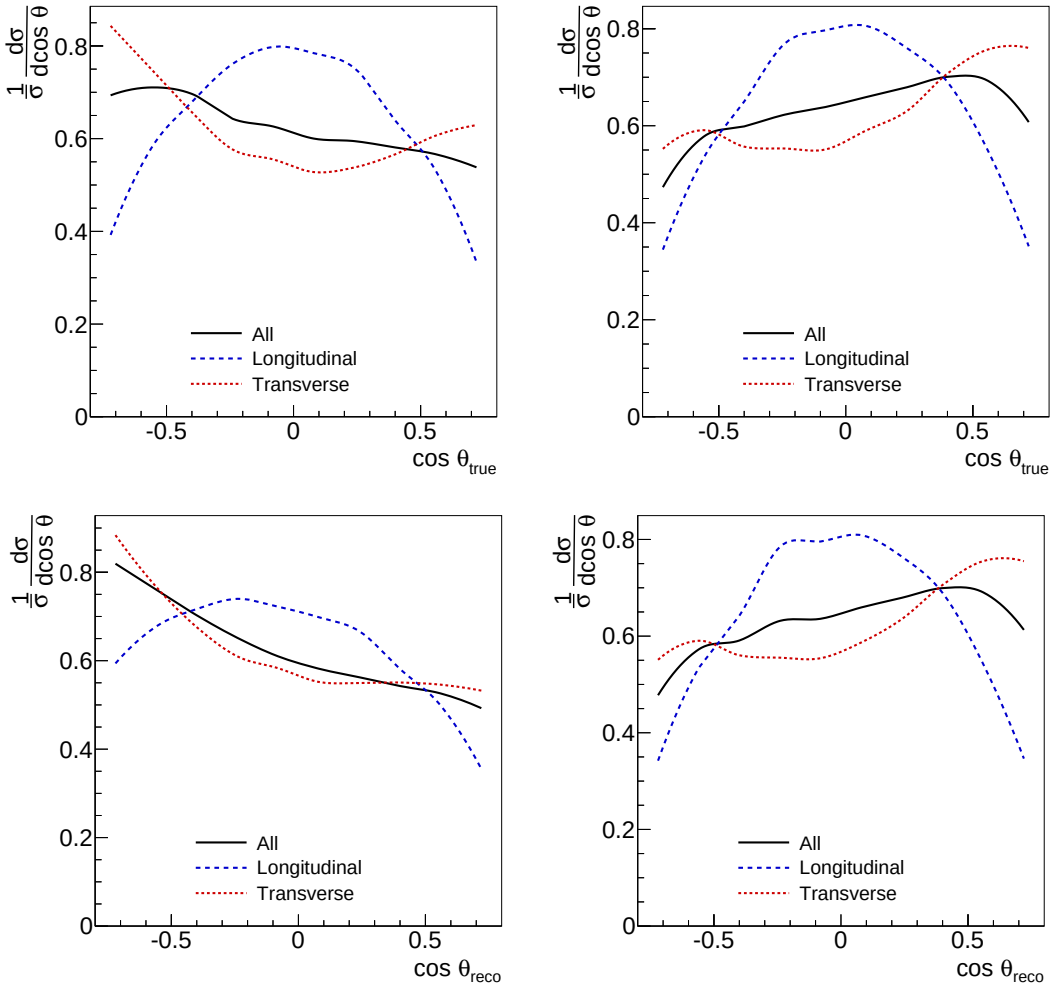

Figure B.6.: Distribution of decay angles in the $WW \to (\ell^{\pm}\nu)\ (jj)$ channel after the high-energy event selection. Top: truth-level results. Bottom: after reconstruction. Left: leptonic W decay. Right: hadronic W decay.

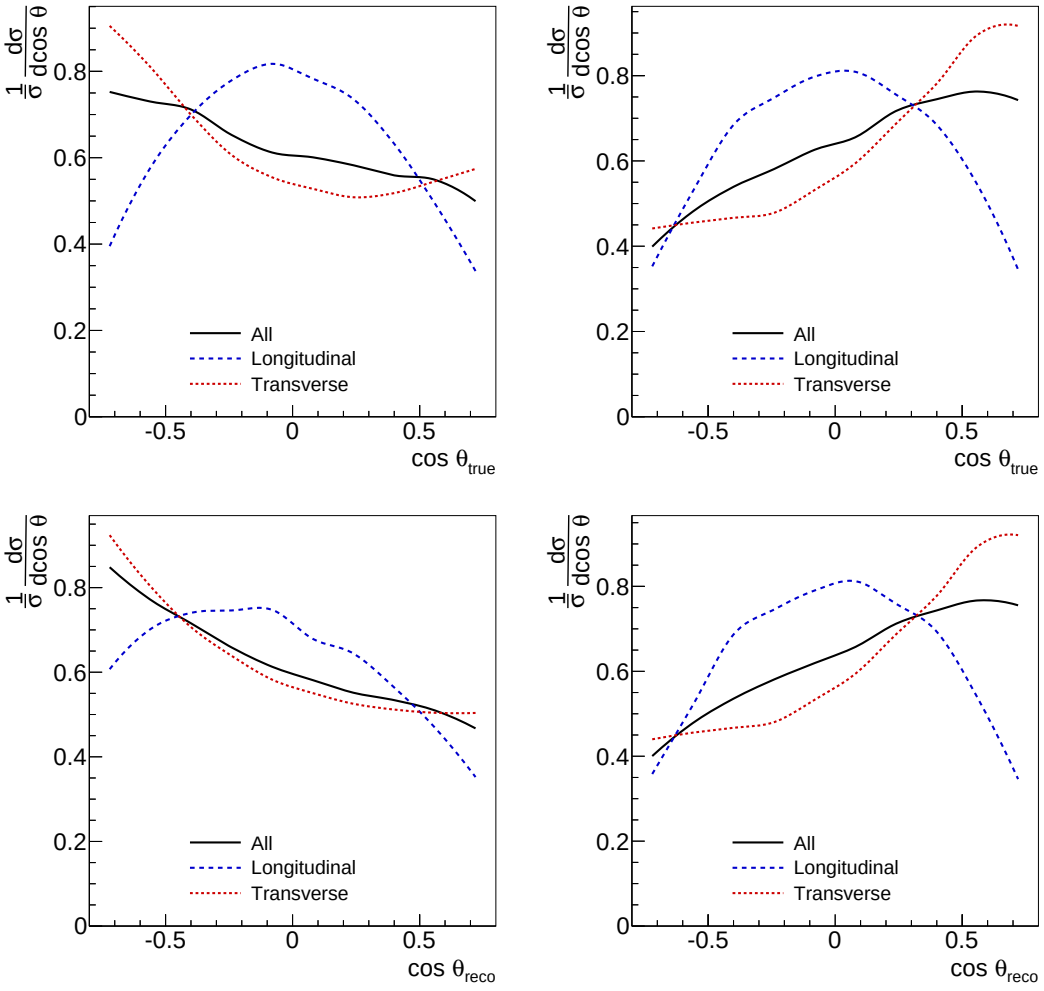

Figure B.7.: Distribution of decay angles in the $WZ \to (\ell^{\pm}\nu)\ (jj)$ channel after the high-energy event selection. Top: truth-level results. Bottom: after reconstruction. Left: W decay. Right: Z decay.

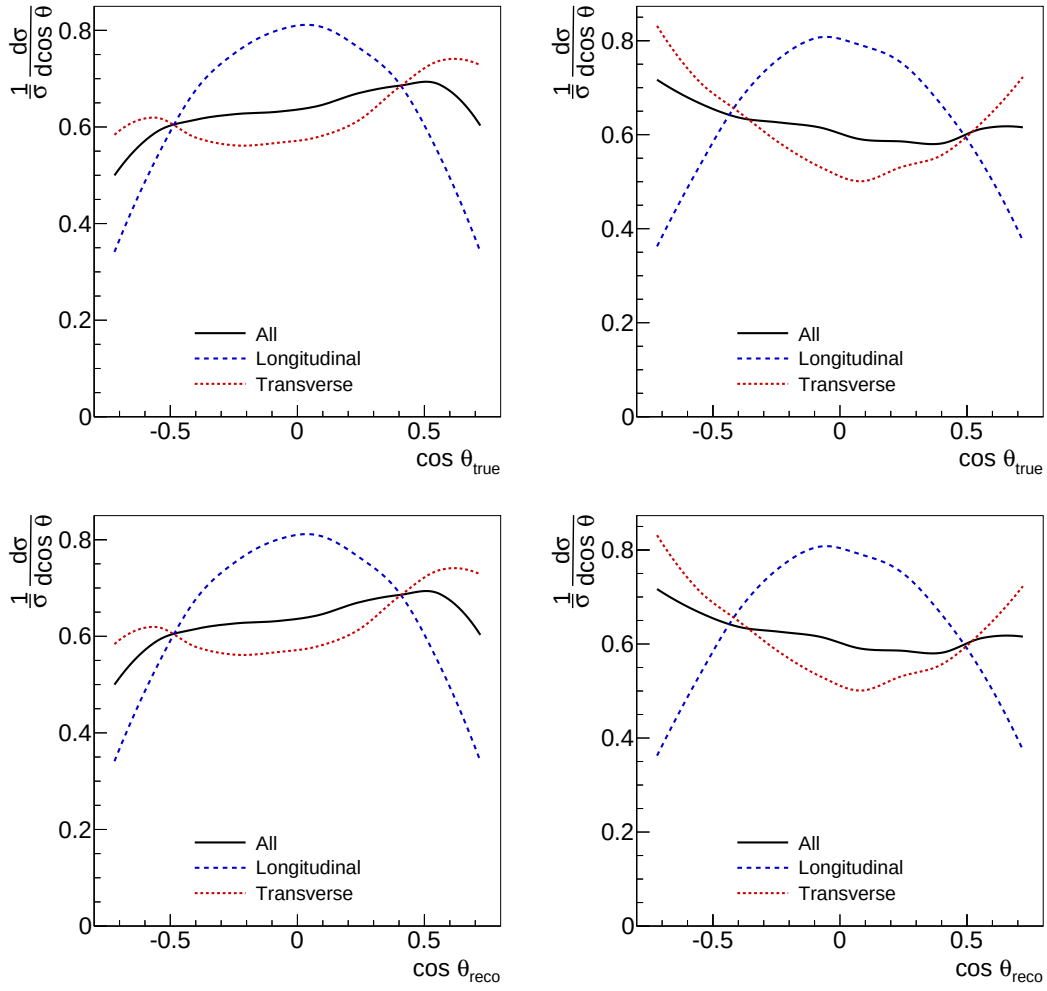

Figure B.8.: Distribution of decay angles in the $WZ \to (jj)\ (\ell^+\ell^-)$ channel after the high-energy event selection. Top: truth-level results. Bottom: after reconstruction. Left: W decay. Right: Z decay.

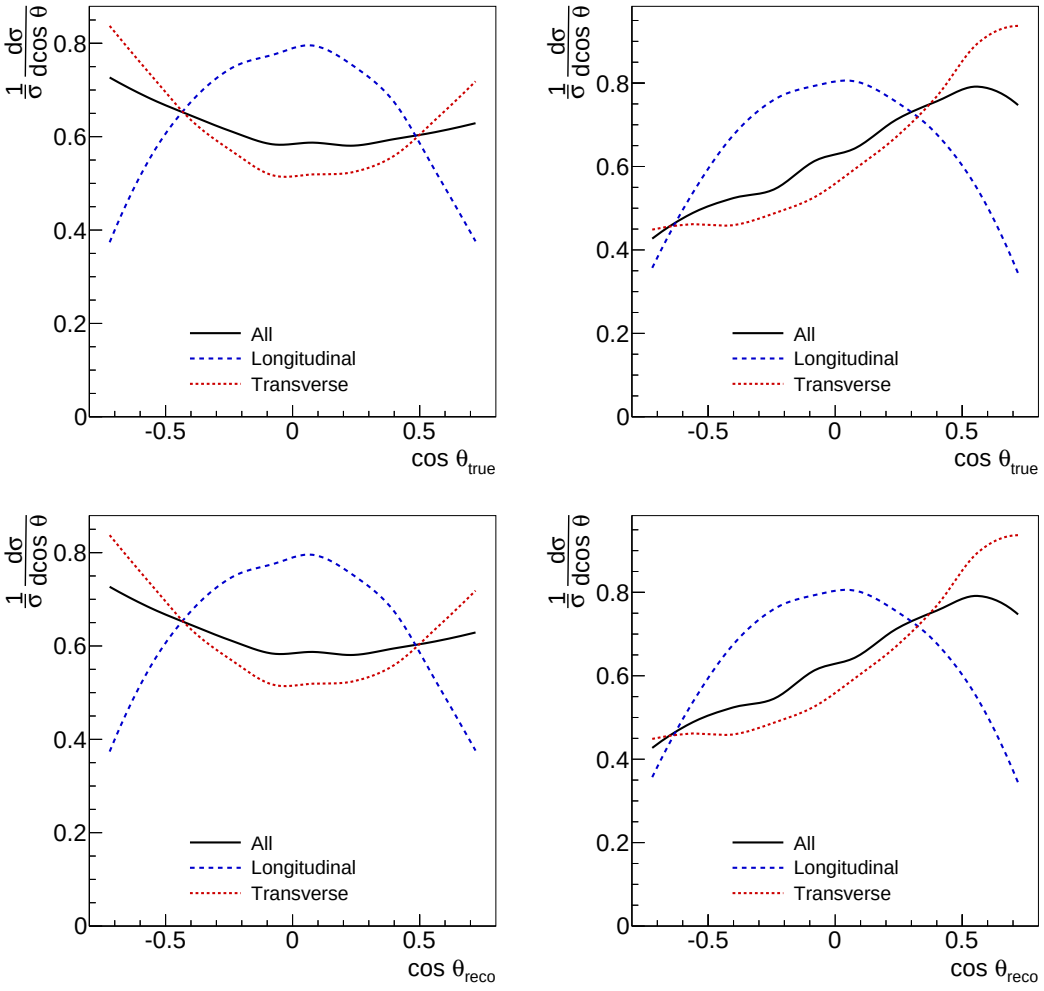

Figure B.9.: Distribution of decay angles in the $ZZ \to (\ell^+\ell^-)\ (jj)$ channel after the high-energy event selection. Top: truth-level results. Bottom: after reconstruction. Left: leptonic Z decay. Right: hadronic Z decay.

B.2. Results of decay fits

In section 3.4.3 the results of polarisation fits to decay angular distributions were given. In tables B.1 and B.2 we show the same results for polarised samples, which were limited at generation level to only longitudinal or transverse final VV pairs.

VV channel	Gauge boson	Longitudinal fraction	
		True	Reconstructed
$W^+W^- \to (\ell^+\nu)\,(\ell^-\bar{\nu})$	W^+	0.99 ± 0.01	–
	W^-	1.00 ± 0.01	–
$W^\pm W^\pm \to (\ell^\pm\nu)\,(\ell^\pm\nu)$	lower-η W	0.94 ± 0.01	–
	larger-η W	0.93 ± 0.01	–
$WZ \to (\ell^\pm\nu)\,(\ell^+\ell^-)$	W	0.94 ± 0.01	0.72 ± 0.01
	Z	0.98 ± 0.01	0.98 ± 0.01
$ZZ \to (\ell^+\ell^-)\,(\ell^+\ell^-)$	lower-η Z	1.00 ± 0.01	1.00 ± 0.01
	larger-η Z	1.00 ± 0.01	1.00 ± 0.01
$ZZ \to (\ell^+\ell^-)\,(\nu\bar{\nu})$	leptonic Z	1.00 ± 0.01	1.00 ± 0.01
$WW \to (\ell^\pm\nu)\,(jj)$	leptonic W	0.98 ± 0.01	0.60 ± 0.01
	hadronic W	1.00 ± 0.01	1.00 ± 0.01
$WZ \to (\ell^\pm\nu)\,(jj)$	W	0.94 ± 0.01	0.73 ± 0.01
	Z	1.00 ± 0.01	1.00 ± 0.01
$WZ \to (jj)\,(\ell^+\ell^-)$	W	1.00 ± 0.01	1.00 ± 0.01
	Z	1.00 ± 0.01	1.00 ± 0.01
$ZZ \to (\ell^+\ell^-)\,(jj)$	leptonic Z	1.00 ± 0.01	1.00 ± 0.01
	hadronic Z	1.00 ± 0.01	1.00 ± 0.01

Table B.1.: Polarisation fit results for a sample consisting of only longitudinal final gauge bosons. The errors are based on the statistical uncertainties of the generated samples, not a measure of statistics at the LHC. In the reconstructed leptonic WW states, the fitting procedure does not converge.

VV channel	Gauge boson	Longitudinal fraction	
		True	Reconstructed
$W^+W^- \to (\ell^+\nu)\,(\ell^-\bar{\nu})$	W^+	0.00 ± 0.01	–
	W^-	0.00 ± 0.01	–
$W^\pm W^\pm \to (\ell^\pm\nu)\,(\ell^\pm\nu)$	lower-η W	0.00 ± 0.01	–
	larger-η W	0.00 ± 0.01	–
$WZ \to (\ell^\pm\nu)\,(\ell^+\ell^-)$	W	0.04 ± 0.01	0.17 ± 0.01
	Z	0.01 ± 0.01	0.01 ± 0.01
$ZZ \to (\ell^+\ell^-)\,(\ell^+\ell^-)$	lower-η Z	0.08 ± 0.01	0.08 ± 0.01
	larger-η Z	0.06 ± 0.01	0.06 ± 0.01
$ZZ \to (\ell^+\ell^-)\,(\nu\bar{\nu})$	leptonic Z	0.03 ± 0.01	0.03 ± 0.01
$WW \to (\ell^\pm\nu)\,(jj)$	leptonic W	0.18 ± 0.01	0.20 ± 0.01
	hadronic W	0.33 ± 0.01	0.33 ± 0.01
$WZ \to (\ell^\pm\nu)\,(jj)$	W	0.10 ± 0.01	0.22 ± 0.01
	Z	0.19 ± 0.01	0.19 ± 0.01
$WZ \to (jj)\,(\ell^+\ell^-)$	W	0.26 ± 0.01	0.26 ± 0.01
	Z	0.02 ± 0.01	0.02 ± 0.01
$ZZ \to (\ell^+\ell^-)\,(jj)$	leptonic Z	0.03 ± 0.01	0.03 ± 0.01
	hadronic Z	0.21 ± 0.01	0.21 ± 0.01

Table B.2.: Polarisation fit results for a sample consisting of only transverse final gauge bosons. The errors are based on the statistical uncertainties of the generated samples, not a measure of statistics at the LHC. In the reconstructed leptonic WW states, the fitting procedure does not converge.

B.3. Parameter space for the simple model

In chapter 4 events were generated for a simple model with two parameters a_L and a_T, which describe the coupling of the Higgs boson to longitudinal and transverse massive vector bosons. In figure B.10 we give the parameter points for which event samples were generated. Between these points, results were interpolated based on Delauny triangulation [84].

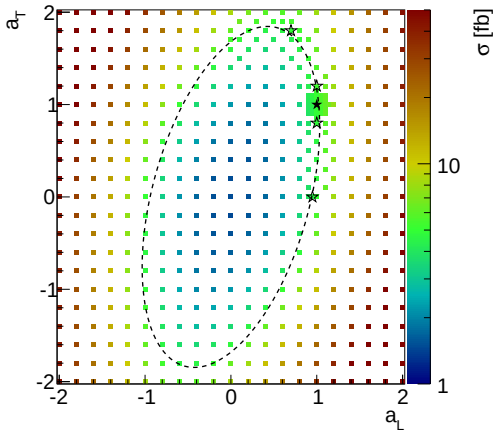

Figure B.10.: Parameter-space points in the simple model for which event samples were generated. Close to the Standard Model value $a_L = a_T = 1$, the resolution of the parameter-space sampling is larger than the binning of this plot. The colour of the dots denotes the cross section after our Higgs-resonance selection cuts. The stars show the benchmark samples used to plot many of the kinematic distributions in section 4.4, while the dotted ellipse again denotes the region of constant cross section.

References

[1] ATLAS Collaboration, 'Observation of a new particle in the search for the Standard Model Higgs boson with the ATLAS detector at the LHC.' *PhysLett*, *B716*: p. 1, 2012, 1207.7214.

[2] CMS Collaboration, 'Observation of a new boson at a mass of 125 GeV with the CMS experiment at the LHC.' *PhysLett*, *B716*: p. 30, 2012, 1207.7235.

[3] D. B. Kaplan, H. Georgi, and S. Dimopoulos, 'Composite Higgs Scalars.' *PhysLett*, *B136*: p. 187, 1984.

[4] G. F. Giudice, C. Grojean, A. Pomarol, and R. Rattazzi, 'The Strongly-Interacting Light Higgs.' *JHEP*, *0706*: p. 045, 2007, hep-ph/0703164.

[5] N. Arkani-Hamed, A. G. Cohen, and H. Georgi, 'Electroweak symmetry breaking from dimensional deconstruction.' *PhysLett*, *B513*: p. 232, 2001, hep-ph/0105239.

[6] R. Contino, Y. Nomura, and A. Pomarol, 'Higgs as a holographic pseudo-Goldstone boson.' *NuclPhys*, *B671*: p. 148, 2003, hep-ph/0306259.

[7] J. M. Cornwall, D. N. Levin, and G. Tiktopoulos, 'Derivation of Gauge Invariance from High-Energy Unitarity Bounds on the s Matrix.' *PhysRev*, *D10*: p. 1145, 1974.

[8] B. W. Lee, C. Quigg, and H. Thacker, 'Weak Interactions at Very High Energies: The Role of the Higgs Boson Mass.' *PhysRev*, *D16*: p. 1519, 1977.

[9] M. S. Chanowitz and M. K. Gaillard, 'The TeV Physics of Strongly Interacting W's and Z's.' *NuclPhys*, *B261*: p. 379, 1985.

[10] C. H. Llewellyn Smith, 'High-Energy Behavior and Gauge Symmetry.' *PhysLett*, *B46*: p. 233, 1973.

[11] D. A. Dicus and V. S. Mathur, 'Upper bounds on the values of masses in unified gauge theories.' *PhysRev*, *D7*: p. 3111, 1973.

[12] M. Veltman, 'Second Threshold in Weak Interactions.' *Acta PhysPolon*, *B8*: p. 475, 1977.

[13] J. Bagger, V. D. Barger, K. Cheung, J. F. Gunion, T. Han, et al., 'The Strongly interacting WW system: Gold plated modes.' *PhysRev*, *D49*: p. 1246, 1994, hep-ph/9306256.

[14] J. Bagger, V. D. Barger, K. Cheung, J. F. Gunion, T. Han, et al., 'CERN LHC analysis of the strongly interacting WW system: Gold plated modes.' *PhysRev*, *D52*: p. 3878, 1995, hep-ph/9504426.

[15] J. Bagger, S. Dawson, and G. Valencia, 'Effective field theory calculation of p p → V(L) V(L) X.' *NuclPhys*, *B399*: p. 364, 1993, hep-ph/9204211.

[16] J. M. Butterworth, B. E. Cox, and J. R. Forshaw, '*WW* scattering at the CERN LHC.' *PhysRev*, *D65*: p. 096014, 2002, hep-ph/0201098.

[17] A. Ballestrero, G. Bevilacqua, D. B. Franzosi, and E. Maina, 'How well can the LHC distinguish between the SM light Higgs scenario, a composite Higgs and the Higgsless case using VV scattering channels?' *JHEP*, *0911*: p. 126, 2009, 0909.3838.

[18] A. Ballestrero, D. B. Franzosi, and E. Maina, 'Vector-Vector scattering at the LHC with two charged leptons and two neutrinos in the final state.' *JHEP*, *1106*: p. 013, 2011, 1011.1514.

[19] A. Ballestrero, D. B. Franzosi, L. Oggero, and E. Maina, 'Vector Boson scattering at the LHC: counting experiments for unitarized models in a full six fermion approach.' *JHEP*, *1203*: p. 031, 2012, 1112.1171.

[20] A. Ballestrero, D. B. Franzosi, and E. Maina, 'Exploring alternative symmetry breaking mechanisms at the LHC with 7, 8 and 10 TeV total energy.' *JHEP*, *1205*: p. 083, 2012, 1203.2771.

[21] K. Cheung, C.-W. Chiang, and T.-C. Yuan, 'Partially Strong WW Scattering.' *PhysRev*, *D78*: p. 051701, 2008, 0803.2661.

[22] H.-J. He, Y.-P. Kuang, C. P. Yuan, and B. Zhang, 'Anomalous gauge interactions of the Higgs boson: Precision constraints and weak boson scatterings.' *PhysLett*, *B554*: p. 64, 2003, hep-ph/0211229.

[23] B. Zhang, Y.-P. Kuang, H.-J. He, and C. P. Yuan, 'Testing anomalous gauge couplings of the Higgs boson via weak boson scatterings at the CERN LHC.' *PhysRev*, *D67*: p. 114024, 2003, hep-ph/0303048.

[24] T. Han, D. Krohn, L.-T. Wang, and W. Zhu, 'New Physics Signals in Longitudinal Gauge Boson Scattering at the LHC.' *JHEP*, *1003*: p. 082, 2010, 0911.3656.

[25] S. Dawson, 'The Effective W Approximation.' *NuclPhys*, *B249*: p. 42, 1985.

[26] L. Kane, G. W. Repko, W. and B. Rolnick, W. 'The Effective $W^{\pm}$, Z^0 Approximation for High-Energy Collisions.' *PhysLett*, *B148*: p. 367, 1984.

[27] P. Borel, R. Franceschini, R. Rattazzi, and A. Wulzer, 'Probing the Scattering of Equivalent Electroweak Bosons.' *JHEP*, *1206*: p. 122, 2012, 1202.1904.

[28] J. Brehmer, J. Jaeckel, and T. Plehn, 'Polarized WW Scattering on the Higgs Pole.', 2014, submitted to JHEP, 1404.5951.

[29] T. Plehn, 'Lectures on LHC Physics.' *LectNotes Phys*, *844*, 2012, 0910.4182.

[30] S. Weinberg, 'Implications of Dynamical Symmetry Breaking.' *PhysRev*, *D13*: p. 974, 1976.

[31] L. Susskind, 'Dynamics of Spontaneous Symmetry Breaking in the Weinberg-Salam Theory.' *PhysRev*, *D20*: p. 2619, 1979.

[32] E. Farhi and L. Susskind, 'Technicolor.' *PhysRept*, *74*: p. 277, 1981.

[33] M. Suzuki, 'Dynamical Composite Models of Electroweak Bosons.' *PhysRev*, *D37*: p. 210, 1988.

[34] K. Hagiwara, S. Ishihara, R. Szalapski, and D. Zeppenfeld, 'Low-energy effects of new interactions in the electroweak boson sector.' *PhysRev*, *D48*: p. 2182, 1993.

[35] S. Willenbrock and C. Zhang, 'Effective Field Theory Beyond the Standard Model.' 2014, 1401.0470.

[36] C. Englert, A. Freitas, M. Muhlleitner, T. Plehn, M. Rauch, et al., 'Precision Measurements of Higgs Couplings: Implications for New Physics Scales.' 2014, 1403.7191.

[37] W. Buchmuller and D. Wyler, 'Effective Lagrangian Analysis of New Interactions and Flavor Conservation.' *NuclPhys*, *B268*: p. 621, 1986.

[38] B. Grzadkowski, M. Iskrzynski, M. Misiak, and J. Rosiek, 'Dimension-Six Terms in the Standard Model Lagrangian.' *JHEP*, *1010*: p. 085, 2010, 1008.4884.

[39] J. Elias-Miro, J. R. Espinosa, E. Masso, and A. Pomarol, 'Higgs windows to new physics through d=6 operators: constraints and one-loop anomalous dimensions.' *JHEP*, *1311*: p. 066, 2013, 1308.1879.

[40] C. Degrande, N. Greiner, W. Kilian, O. Mattelaer, H. Mebane, et al., 'Effective Field Theory: A Modern Approach to Anomalous Couplings.' *Annals Phys*, *335*: p. 21, 2013, 1205.4231.

[41] ATLAS Collaboration, 'Evidence for the spin-0 nature of the Higgs boson using ATLAS data.' *PhysLett*, *B726*: p. 120, 2013, 1307.1432.

[42] D. López-Val, T. Plehn, and M. Rauch, 'Measuring Extended Higgs Sectors as a Consistent Free Couplings Model.' *JHEP*, *1310*: p. 134, 2013, 1308.1979.

[43] T. Corbett, O. J. P. Eboli, J. Gonzalez-Fraile, and M. C. Gonzalez-Garcia, 'Robust Determination of the Higgs Couplings: Power to the Data.' *PhysRev*, *D87*: p. 015022, 2013, 1211.4580.

[44] A. De Rujula, M. B. Gavela, P. Hernandez, and E. Masso, 'The Selfcouplings of vector bosons: Does LEP-1 obviate LEP-2?' *NuclPhys*, *B384*: p. 3, 1992.

[45] K. Stelle, 'Unification lecture notes.', 2011.

[46] J. Alwall, M. Herquet, F. Maltoni, O. Mattelaer, and T. Stelzer, 'MadGraph 5: Going Beyond.' *JHEP*, *1106*: p. 128, 2011, 1106.0522.

[47] P. de Aquino, W. Link, F. Maltoni, O. Mattelaer, and T. Stelzer, 'ALOHA: Automatic Libraries Of Helicity Amplitudes for Feynman Diagram Computations.' *ComputPhysCommun*, *183*: p. 2254, 2012, 1108.2041.

[48] H. Murayama, I. Watanabe, and K. Hagiwara, 'HELAS: HELicity Amplitude Subroutines for Feynman diagram evaluations.' 1992.

[49] J. Pumplin, D. R. Stump, J. Huston, H. L. Lai, P. M. Nadolsky, et al., 'New generation of parton distributions with uncertainties from global QCD analysis.' *JHEP*, *0207*: p. 012, 2002, hep-ph/0201195.

[50] E. Accomando, A. Ballestrero, A. Belhouari, and E. Maina, 'Isolating Vector Boson Scattering at the LHC: Gauge cancellations and the Equivalent Vector Boson Approximation vs complete calculations.' *PhysRev*, *D74*: p. 073010, 2006, hep-ph/0608019.

[51] V. D. Barger, R. J. N. Phillips, and D. Zeppenfeld, 'Mini-jet veto: A Tool for the heavy Higgs search at the LHC.' *PhysLett*, *B346*: p. 106, 1995, hep-ph/9412276.

[52] D. L. Rainwater, R. Szalapski, and D. Zeppenfeld, 'Probing color singlet exchange in Z + two jet events at the CERN LHC.' *PhysRev*, *D54*: p. 6680, 1996, hep-ph/9605444.

[53] V. Del Duca, G. Klamke, D. Zeppenfeld, M. L. Mangano, M. Moretti, et al., 'Monte Carlo studies of the jet activity in Higgs + 2 jet events.' *JHEP*, *0610*: p. 016, 2006, hep-ph/0608158.

[54] C. Bernaciak, M. S. A. Buschmann, A. Butter, and T. Plehn, 'Fox–Wolfram Moments in Higgs Physics.' *PhysRev*, *D87*: p. 073014, 2013, 1212.4436.

[55] C. Bernaciak, B. Mellado, T. Plehn, P. Schichtel, and X. Ruan, 'Improving Higgs plus Jets analyses through Fox–Wolfram Moments.' *PhysRev*, *D89*: p. 053006, 2014, 1311.5891.

[56] V. D. Barger, G. Bhattacharya, T. Han, and B. A. Kniehl, 'Intermediate mass Higgs boson at hadron supercolliders.' *PhysRev*, *D43*: p. 779, 1991.

[57] M. Dittmar and H. K. Dreiner, 'How to find a Higgs boson with a mass between 155 GeV - 180 GeV at the LHC.' *PhysRev*, *D55*: p. 167, 1997, hep-ph/9608317.

[58] T. Plehn, D. L. Rainwater, and D. Zeppenfeld, 'Determining the structure of Higgs couplings at the LHC.' *PhysRevLett*, *88*: p. 051801, 2002, hep-ph/0105325.

[59] O. J. P. Eboli and D. Zeppenfeld, 'Observing an invisible Higgs boson.' *PhysLett*, *B495*: p. 147, 2000, hep-ph/0009158.

[60] V. Hankele, G. Klamke, D. Zeppenfeld, and T. Figy, 'Anomalous Higgs boson couplings in vector boson fusion at the CERN LHC.' *PhysRev*, *D74*: p. 095001, 2006, hep-ph/0609075.

[61] C. Ruwiedel, N. Wermes, and M. Schumacher, 'Prospects for the measurement of the structure of the coupling of a Higgs boson to weak gauge bosons in weak boson fusion with the ATLAS detector.' *EurPhysJ*, *C51*: p. 385, 2007.

[62] K. Hagiwara, Q. Li, and K. Mawatari, 'Jet angular correlation in vector-boson fusion processes at hadron colliders.' *JHEP*, *0907*: p. 101, 2009, 0905.4314.

[63] A. Djouadi, R. M. Godbole, B. Mellado, and K. Mohan, 'Probing the spin-parity of the Higgs boson via jet kinematics in vector boson fusion.' *PhysLett*, *B723*: p. 307, 2013, 1301.4965.

[64] C. Englert, D. Goncalves-Netto, K. Mawatari, and T. Plehn, 'Higgs Quantum Numbers in Weak Boson Fusion.' *JHEP*, *1301*: p. 148, 2013, 1212.0843.

[65] N. Cabibbo and A. Maksymowicz, 'Angular Correlations in Ke-4 Decays and Determination of Low-Energy pi-pi Phase Shifts.' *PhysRev*, *137*: p. B438, 1965.

[66] S. Groote, J. G. Korner, and P. Tuvike, 'O(α_s) Corrections to the Decays of Polarized $W^{\pm}$ and Z Bosons into Massive Quark Pairs.' *EurPhysJ*, *C72*: p. 2177, 2012, 1204.5295.

[67] ATLAS Collaboration, 'The ATLAS Experiment at the CERN Large Hadron Collider.' *JINST*, *3*: p. S08003, 2008.

[68] CMS Collaboration, 'CMS physics: Technical design report.' 2006.

[69] CMS Collaboration, 'CMS technical design report, volume II: Physics performance.' *JPhys*, *G34*: p. 995, 2007.

[70] ATLAS Collaboration, 'Search for the Higgs boson in the $H \to WW \to \ell\nu jj$ decay channel at $\sqrt{s} = 7$ TeV with the ATLAS detector.' *PhysLett*, *B718*: p. 391, 2012, 1206.6074.

[71] ATLAS Collaboration, 'Search for the Standard Model Higgs boson in the decay channel $H \to ZZ^{(*)} \to 4\ell$ with 4.8 fb^{-1} of pp collision data at $\sqrt{s} = 7$ TeV with ATLAS.' *PhysLett*, *B710*: p. 383, 2012, 1202.1415.

[72] ATLAS Collaboration, 'Search for a standard model Higgs boson in the mass range 200 – 600 GeV in the $H \to ZZ \to \ell^+\ell^- q\bar{q}$ decay channel with the ATLAS detector.' *PhysLett*, *B717*: p. 70, 2012, 1206.2443.

[73] C. G. Lester and D. J. Summers, 'Measuring masses of semiinvisibly decaying particles pair produced at hadron colliders.' *PhysLett*, *B463*: p. 99, 1999, hep-ph/9906349.

[74] A. Barr, C. Lester, and P. Stephens, 'm(T2): The Truth behind the glamour.' *JPhys*, *G29*: p. 2343, 2003, hep-ph/0304226.

[75] W. S. Cho, K. Choi, Y. G. Kim, and C. B. Park, 'M(T2)-assisted on-shell reconstruction of missing momenta and its application to spin measurement at the LHC.' *PhysRev*, *D79*: p. 031701, 2009, 0810.4853.

[76] D. Guadagnoli and C. B. Park, 'MT2-reconstructed invisible momenta as spin analizers, and an application to top polarization.' 2013, 1308.2226.

[77] D. L. Rainwater and D. Zeppenfeld, 'Observing $H \to W^*W^* \to e^\pm\mu^\mp \not{p}_T$ in weak boson fusion with dual forward jet tagging at the CERN LHC.' *PhysRev*, *D60*: p. 113004, 1999, hep-ph/9906218.

[78] N. Kauer, T. Plehn, D. L. Rainwater, and D. Zeppenfeld, '$H \to W^+W^-$ as the discovery mode for a light Higgs boson.' *PhysLett*, *B503*: p. 113, 2001, hep-ph/0012351.

[79] M. Lamont, 'Status of the LHC.' *JPhysConfSer*, *455*: p. 012001, 2013.

[80] ATLAS Collaboration, 'Physics at a High-Luminosity LHC with ATLAS.' 2013, 1307.7292.

[81] ATLAS Collaboration, 'ATLAS Upgrade for the HL-LHC: Meeting the challenges of a five-fold increase in collision rate.' *EPJ Web Conf*, *28*: p. 12069, 2012, 1201.5469.

[82] M. R. Whalley, D. Bourilkov, and R. C. Group, 'The Les Houches accord PDFs (LHAPDF) and LHAGLUE.' 2005, hep-ph/0508110.

[83] A. Djouadi, J. Kalinowski, and M. Spira, 'HDECAY: A Program for Higgs boson decays in the standard model and its supersymmetric extension.' *ComputPhysCommun*, *108*: p. 56, 1998, hep-ph/9704448.

[84] B. Delaunay, 'Sur la sphere vide.' *Izv Akad Nauk SSSR, Otdelenie Matematicheskii i Estestvennyka Nauk*, *7*(793-800): pp. 1, 1934.

[85] R. A. Fisher, 'Statistical methods for research workers.' *Oliver and Boyd, Edinburgh*, *14*, 1970.

Acknowledgements

First of all, I would like to thank Tilman Plehn, who had the idea for this thesis and provided a huge amount of physical insight and helpful advice. More important, he made physics fun. Thanks for all the honest rants and entertaining stories during lunch. I also want to thank Joerg Jaeckel, who joined this project at an early stage, always asked the right questions to keep us on track, and immediately responded to my problems in times of confusion. I was genuinely surprised by the level of collaboration and support during the research stage and especially while writing our paper.

I am very grateful to the whole group, including some visitors and former members: Cathy Bernaciak, Nishita Desai, Karin Firnkes, Jamil Hetzel, Sebastian Hoof, Thomas Hugle, Martin Jankowiak, Felix Kling, David Lopez-Val, Beatriz Tapia Oregui, Torben Schell, Peter Schichtel, and Jamie Tattersall. Thank you for the great time I had (and still have) here. To Felix, thank you for proofreading this thesis. Most of all, I want to thank Torben for his help with all kind of technical problems and for keeping the critical coffee system running.

It is a great pleasure to thank Antje Brehmer for reading this thesis and pointing out many missing commas and phrases too American. I also want to thank Dominik Neuenfeld for his comments and questions. As always, they were full of insight and a big help. I am very grateful to Astrid Blin for being an especially critical reader of this thesis. Astrid, thank you also for motivating me during many a coffee break.

I would like to express my sincere gratitude to my ever-supportive parents and to all the friends who accompanied me during this undertaking. Last but definitely not least, I want to thank Merle Reinhart. Thank you for your advice, help, and for always being there when I need you.

Erklärung

Ich versichere, dass ich diese Arbeit selbstständig verfasst habe und keine anderen als die angegebenen Quellen und Hilfsmittel benutzt habe.

Heidelberg, den 17. Juni 2014,

Johann Brehmer